A METHODOLOGY FOR STATE DETERMINATION WITHOUT PRIOR INFORMATION USING X-RAY PULSAR NAVIGATION SYSTEMS

BY

KEVIN LOHAN

DISSERTATION

Submitted in partial fulfillment of the requirements
for the degree of Doctor of Philosophy in Aerospace Engineering
in the Graduate College of the
University of Illinois at Urbana-Champaign, 2021

Urbana, Illinois

Doctoral Committee:

Assistant Professor Zachary R. Putnam, Chair
Associate Professor James T. Allison
Associate Professor Timothy Bretl
Dr. Chris D'Souza

ABSTRACT

Onboard measurements of periodic x-ray signals from highly stable, rapidly spinning stars called pulsars, enable determination of spacecraft position, velocity, and attitude states. Due to the short period of pulsar signals, X-ray pulsar based navigation (XNAV), may result in position ambiguity within the Solar System and typically requires an initial position estimate in order to determine spacecraft position. This dissertation presents a method to determine spacecraft position using XNAV in the absence of any prior state information, a scenario sometimes refered to as the cold-start problem or the lost in space scenario. In these scenarios, the spacecraft cannot communicate with Earth-based systems, nor is any prior state information available, excepting the current time. A position determination capability under these conditions may provide navigation redundancy for high-value missions (e.g. human missions to Mars), improved spacecraft autonomy, or improved deep-space navigation accuracy for low cost missions such as cubesats. In order to solve the cold-start problem, a model is developed to find candidate spacecraft positions for a given XNAV measurement. Combinations of pulsars are explored to find sets of pulsars which minimize the number of candidate solutions within a given domain. Through proper pulsar selection it is possible to find a single candidate position within a given domain solving the initial position determination problem without prior information.

This investigation includes a comprehensive survey of XNAV technology across a range of topics from advances in pulsar modeling, timing models, algorithms to estimate the pulsar phase, navigation filters, and hardware. By observing x-ray signals from pulsars, XNAV may be used to improve the navigation capabilities of spacecraft. XNAV is a particularly strong candidate for deep space applications because it is more accurate than ground based systems beyond 15 AU. XNAV may allow for more spacecraft autonomy, and improved robustness and accuracy when integrated with other navigation technology. Several flight experiments have been conducted to test the feasibility of XNAV technology on Earth orbiting spacecraft. As hardware and signal processing algorithms improve, XNAV will become a more desirable space technology option for future space missions.

The majority of current XNAV system concepts require an initial position estimate to

resolve ambiguity in the state determination process. Without prior information there are many candidate positions which may produce the same measurement as the true spacecraft position. If position ambiguity can be resolved, XNAV may enable full state estimation without prior information, a valuable capability for future space missions. Candidate spacecraft positions may be found by searching for intersections between pulsar wavefronts. An efficient numeric scheme for determining candidate spacecraft positions is developed for an arbitrary number of observed pulsars in two and three dimensions. Results indicate that, as the error in the measurement is reduced by an order of magnitude, the number of candidate solutions is also reduced by an order of magnitude. However, increasing the number of pulsars observed by one pulsar reduces the number of candidate solutions by two orders of magnitude.

Pulsar selection criteria to minimize the number of candidate solutions over a given domain are developed in terms of relative direction, period, and phase accuracy. Results indicate that smaller angular separation between the observed pulsars and increased period of the observed signals reduces the number of solutions in a given domain. Further, phase measurement accuracy should be improved simultaneously for all observed pulsars rather than focusing on improving observation of a single pulsar. These selection criteria are verified by evaluating the number of candidate solutions for all permutations of 34 candidate pulsars. Combinations of 3, 4 or 5 pulsars are evaluated to determine which set minimizes the number of candidate positions within a given domain.

By selecting an appropriate set of pulsars for a desired domain size, a single candidate position may be found within the domain. The trajectories of NASA's Insight, Juno and New Horizons missions are considered to represent Mars, Jupiter, or outer Solar System missions. In these cases results are presented for combinations of 5, 7 or 8 pulsar observations in the presence of measurement error. For all three cases a single candidate position is found to within the predefined measurement uncertainty. These results demonstrate feasibility of using XNAV for initial position determination without prior information for a variety of missions within the Solar System.

TABLE OF CONTENTS

LIST OF TABLES

LIST OF FIGURES

CHAPTER 1

INTRODUCTION

Since their discovery in 1967, pulsars have been an active topic of research across a variety of disciplines. Studies have looked into understanding how pulsars are formed [16, 17, 18], the mechanisms driving pulsars [19, 8], and how pulsars evolve over time [19, 20]. Pulsars have been proposed to be used for a variety of topics from atmospheric modeling [21], estimating the mass of planets [22], or gravity wave detection [23]. As knowledge of pulsar astronomy improved, using pulsars for time keeping [24] or for navigation [25] was proposed. Radio pulsars were found to require too large of an antenna to be applicable for many spacecraft [26] and research shifted towards using x-ray pulsars for space navigation applications since the required detector could be much smaller [27]. Using x-ray pulsars, Downs found that position accuracy could be between 150 and 1500 km depending on the antenna gain; Chester and Butman proposed that a 0.1 m^2 detector would generate a 150 km position estimate [27]. This work sparked research into the field of x-ray pulsar based space navigation.

X-ray pulsar based navigation (XNAV) uses observations of periodic signals from x-ray pulsars to determine spacecraft position, velocity, and/or attitude. XNAV has shown promise as an independent autonomous navigation system [28, 29, 30, 31], as part of a larger integrated navigation system [32, 12], or for relative navigation between satellites in a constellation [33]. For deep space navigation applications, XNAV has two main benefits relative to the current state of the art: (1) XNAV is nearly autonomous, i.e. navigation tasks may be performed onboard a spacecraft with limited need for communication with an Earth-based ground station and (2) the root means square XNAV position error is lower than that of the current state of the art, the Deep space Network (DSN), at distances from Earth greater than approximately 15 AU.

XNAV presents a strong candidate to move away from the DSN for spacecraft navigation. As more spacecraft are being placed into space, DSN time and resources are becoming more scarce. XNAV presents an opportunity to navigate spacecraft autonomously, or reduce communication with the DSN to once every 3 months [30]. DSN-based position accuracy degrades significantly with distance from Earth: The accuracy of the DSN in non-radial directions increases by 4 km per AU from Earth [34]. In contrast, the error in XNAV-based

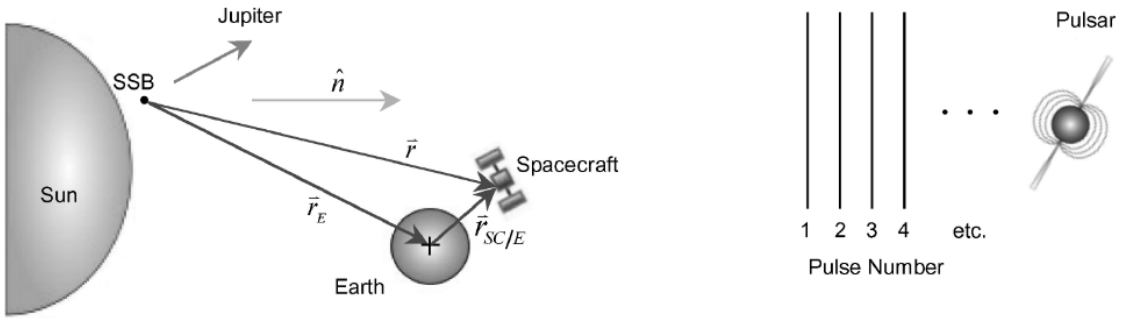

Figure 1.1: Pulsar pulse arrival at an observer in the Solar System [1].

position increases from approximately 0 to 5 km as the distance from the Solar System barrycenter increases from 0 to 100 AU [35].

XNAV technology still requires additional development. In a comparison for a lunar return trajectory of Global Positioning System (GPS), optical navigation, and XNAV it was found that current XNAV technology did not satisfy the trajectory requirements [36]. For missions which travel further than the moon, XNAV may be a promising candidate. Shemar et al. found that for a mission to Mars a sapcecraft may operate autonomously for up to 3 months while maintaining a position accuracy of 30 km [30].

Detailed overviews of XNAV are presented in [37, 38, 2, 39, 30]. A typical XNAV concept of operations is shown in Fig. 1.1. The majority of proposed XNAV applications operate under a relative position update framework. The state update process can be summarized as: [40, 41]

1. A pulsar is observed for a given length of time and all x-ray photons which reach the detector are recorded.

2. Using an initial position estimate, the photon arrival times are then translated from the spacecraft frame of reference to a reference epoch.

3. The photon time of arrivals are compared to the phase at the epoch, where the phase evolution of the pulsar is well-characterized, to determine a phase offset relative to the reference.

4. The phase offset is used to generate a position update in the direction of the observed pulsar.

A key limitation of the relative position update method is that it requires an initial position estimate. Without that estimate, the photon time of arrivals cannot be shifted back to the reference epoch. Sheikh et al. developed an alternate solution strategy termed “absolute

position determination" [42], where measurement differences are used to construct a set of candidate wavefronts for each pulsar measurement. The spacecraft location must be at a point where all wavefronts intersect. To date this XNAV method has not been considered for navigation due to the increased complexity required to measure multiple pulsars simultaneously. However, if multiple pulsars can be observed simultaneously, a full state update can be determined with each measurement. The main drawback to absolute position determination is it requires a bounded domain to search for candidate intersections. If the domain is too large, many candidate positions may be found (indistinguishable from the true position) resulting in position ambiguity.

The focus of this dissertation is on finding solutions to resolve the spacecraft's state in the absence of an initial position estimate, also called the cold-start problem or the "lost in space" scenario. For this problem, no initial position estimate is available, so there is no way to distinguish between peaks of the pulsar waveform and a single pulsar phase measurement only restricts spacecraft position to an infinite set of planes perpendicular to the direction of the pulsar. A second pulsar may be observed to determine the spacecraft position with respect to another direction, this places the spacecraft on a second set of infinite planes. Combining these two measurements results in an infinite set of lines, a third pulsar measurement reduces this space to an infinite set of points, and any subsequent measurement decreases the number of candidate intersections within a given volume of space.

A solution to the cold start problem using XNAV may allow spacecraft to operate with more autonomy and potentially reduce the overall ground based cost of the mission, and make communication to the DSN less frequent, allowing the DSN resources to be shifted to other missions. An independent absolute navigation capability also provides an accurate navigation source for low-cost missions such as cubesats, and is an excellent candidate for navigation in a swarm of spacecraft. Being able to use XNAV in a cold-start scenario provides a sense of redundancy to high-value missions, especially human class missions which cannot fail. Furthermore, it also increases the reliability of XNAV for deep space missions where the XNAV accuracy surpasses the DSN accuracy.

Both the requirement for simultaneous observations as well as a bounded domain (as assumed by Sheikh et al.) can be mitigated when operating in a cold-start scenario. With appropriate time corrections (i.e. the presence of an accurate onboard clock), absolute position determination can work for sequential pulsar measurements. In addition to the phase information from an observed pulsar, the frequency of the signal may also be recorded and compared to a reference frequency to determine the spacecraft's velocity in the direction of the pulsar. Combining the time between measurements with the partial velocity information allows for the translation of sequential measurements to a common reference. This process is

similar to how a digital phase-locked loop is used for XNAV applications when the frequency is time varying [43]. The required domain size to search for a candidate XNAV position has not been sufficiently characterized. While any sufficiently large domain may lead to an intractable problem using current computing technology, the issue can be mitigated through efficient intersection-finding algorithms and developing a better understanding of how to select pulsars to minimize candidate positions within a given domain.

The contributions of this dissertation address these issues and present solutions for determining candidate positions using XNAV measurements without prior state information. These contributions can be summarized as, a comprehensive survey of XNAV technology, development of an efficient method for determining candidate states in a bounded domain, the development and assessment of measurement strategies for XNAV systems, and a method for state determination in a cold-start scenario using XNAV.

Contribution 1: Comprehensive survey of XNAV technology

The use of pulsars for navigation has been an idea since 1974, however, interest in the subject was renewed in 2005 and since then many articles have been published on XNAV. In that time there has only been one, limited survey article written by Sheikh et al. [38], and since then many more publications have presented advances in the use of XNAV, and several spacecraft have been launched to test XNAV applications. Furthermore that survey predominately focused on articles within the United States as at that time majority of XNAV studies were being conducted there. The new survey article seeks to incorporate new advances in XNAV research as well as incorporate publications from around the world to better capture current XNAV research. Chapter 2 presents the findings of this article and gives a comprehensive background on pulsars, modeling pulsars, the XNAV state update process, and current XNAV missions which seek to validate XNAV as a viable strategy for future spacecraft.

Contribution 2: Development of an efficient method for determining candidate states in a bounded domain

Prior to determining a spacecraft's position using XNAV without prior information, all candidate spacecraft positions must be known. The lack of an initial position estimate implies that the spacecraft may be at one of an infinite set of points, therefore a method to quickly find these candidate points is required. Chapter 3 investigates this issue, formulates the problem for both two and three dimensions, and solves the problem both analytically and numerically. Two error modeling methods are proposed, one where the error is modeled as a ball about the intersection of two pulsar wavefronts and one that models error as an uncertainty band about each pulsar wavefront. Additionally, trends in the number of candidate spacecraft positions are shown when the number of pulsar measurements as well

as the accuracy of the pulsar measurements are varied.

Contribution 3: Development and assessment of measurement strategies for XNAV systems

Using the banded error model, an investigation of various pulsar parameters are presented in Chapter 4 to detertmine how to best select a pulsar to minimize the number of candidate solutions in a given domain. Fictitious pulsars are considered to find trends in pulsar selection in an ideal scenario where any combination is possible. Real pulsars are then considered and sets of 3, 4 or 5 pulsars are selected and the number of candidate positions for each combination is found.

Contribution 4: A method for state determination in a cold-start scenario using XNAV

Chapter 5 applies the candidate solution identification algorithm developed in Chapter 3 and the pulsar selection techniques outlined in Chapter 4 to select pulsars to use in a cold start scenario; candidate position identification algorithms are used to determine possible positions for the selected pulsars. Through proper pulsar selection it is possible to reduce the number of candidate solutions within a given domain such that only a single solution exists, thereby removing the position ambiguity entirely. Example applications are presented using the trajectory data from NASA's Insight lander's Earth-Mars transfer trajectory, as well as notional missions to Jupiter and beyond. Results indicate that XNAV may be used for position determination in a cold start scenario if sufficiently accurate pulsar observations can be made and an accurate clock is available. However, the required domain size, and therefore compute time, increases significantly as distance from the Solar System barycenter increases.

CHAPTER 2

SURVEY OF XNAV TECHNOLOGY

This chapter is a comprehensive overview of major developments in the field of XNAV. The Naval Research Laboratory (NRL) was a large contributor to early XNAV work and has compiled two surveys of their contributions to XNAV [37, 2]. An overview of the methods for XNAV was also compiled by Sheikh et al. [38]. The European Space Agency (ESA) has periodically performed feasibility analyses of XNAV [39, 30]. This survey covers XNAV technology from its inception through 2019. An overview of pulsar astronomy is presented along with key findings on the nature of pulsars. The photon emission process is described along with models to simulate the photon arrival process. Different techniques are presented for processing photon arrival data into a phase and frequency measurement of the x-ray pulsar signal. A review of methods for determining spacecraft position or attitude are shown. Lastly, rescent XNAV flight experiments from both the National Aeronautics and Space Administration (NASA) and the China Academy of Space Technology (CAST) are discussed.

2.1 Pulsars

When a massive star runs out of fuel it may undergo a supernova explosion, where part of the star's matter is released into space and the remaining matter collapses [16]. The angular momentum of the collapsing matter is conserved and causes an increase in rotation rate and in some cases the formation of a neutron star [16, 17, 18]. A typical neutron star has roughly 1.4 solar masses with a radius of 20 km and a rotation period of a few seconds or less [8]. The small size of the neutron star led researchers to believe such stars were cold and dark objects in space and could not be detected. In 1967 Hewish et al. observed a pulsating radio signal [44] in what is now known as pulsar PSR B1919+21, therefore discovering the first pulsar. Pulsars are identified by the prefix PSR, with an optional discovery mission abbreviation (XTE, ASCA, etc.), followed by the time epoch (B for B1950 or J for J2000). Immediately following the epoch is the right ascension (hours and minutes), and declination (degrees and minutes). The first measured pulsar, PSR B1919+21, is a pulsar in the B1950 epoch with a right ascension of 19 hours and 19 minutes, and a right ascension of +21

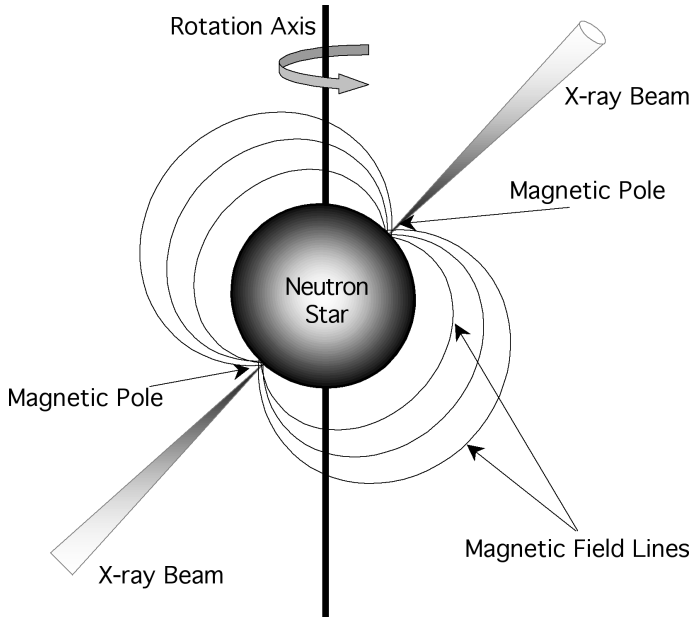

Figure 2.1: Neutron star with different rotation and magnetic field axes [1].

degrees. The discovery by Hewish and Bell spurred interest in the search for other pulsating celestial bodies and neutron stars.

Pulsars are subdivided into three main categories: accretion powered pulsars, rotation powered pulsars, and magnetars. The distinction between the pulsars is the manner in which they are pulsating. Accretion powered pulsars accrete matter from a companion star, which causes a hot spot on the surface of the pulsar where the accretion disk contacts the surface. As the binary system spins, the hot spot moves in and out of view of the observer causing pulsations in recorded x-rays [45]. Rotation powered pulsars are spinning down and rotational energy is being radiated away by the co-rotating magnetic field. Misalignment of the magnetic pole and the rotation axis causes a pulsation in the observed particles similar to a lighthouse [19]. A visual representation of a pulsar may be seen in Fig. 2.1. Magnetars are isolated neutron stars which have an immense magnetic field of approximately 10^{15}G and are emitting x-rays due to the decay of this field [8]. Magnetars are not typically considered viable candidates for XNAV since their long term timing stability has not been sufficiently analyzed.

Most pulsars are formed in binary star-systems. These may be high mass x-ray binary (HMXB) systems, where a companion star with a mass greater than 10 solar masses is present, or low mass x-ray binary (LMXB) systems, where a companion star has mass smaller than one solar mass. HMXB systems are defined by a neutron star that has a large

magnetic field pulling in particles from the solar wind. Some of these particles are drawn in and used to fuel to the pulsar. Others are accelerated along the magnetic field lines and emitted away from the magnetic poles. These types of systems are found throughout space. LMXB systems tend to have a weaker magnetic field due to their formation and are expected to have a longer life. A majority of LMXB systems can be found in galactic cores [19]. When searching for LMXB systems it is more beneficial to search through globular clusters, since globular clusters contain 20% of the known LMXB systems and account for 0.05% of the mass of the galaxy [46].

Rotation powered pulsars are neutron stars where particle emission is being driven by the rotational energy lost form a co-rotating magnetic field. Rotation powered pulsars are good candidates for navigation, however a subset called millisecond pulsars have the most favorable timing characteristics. In general, pulsars slow down as they age, and their magnetic field becomes weaker until they reach the"death line" and become radio silent. In the event that the evolution of a companion star fills the Roche lobe, i.e. the region where mass is bound to the star, mass, and therefore angular momentum, will be transferred to the pulsar. This will cause the neutron star to speed back up and cross the death line again to emit signals once more [20]. Once enough matter has been transferred from the companion, the particle emission powered by the rotation of the pulsar will become significant again. These types of pulsars may also be referred to as recycled millisecond pulsars. Since this evolutionary process makes the system a LMXB, an x-ray outburst from accretion may occur in some millisecond pulsars [47].The formation of isolated millisecond pulsars is not well understood and is still a topic of ongoing research. One hypothesis is that the companion was completely consumed by the pulsar or disrupted out of the system during formation [8].

2.1.1 Pulsar Catalogues

After the initial discovery of a pulsar in 1967 many more pulsars have been found emitting across the electromagnetic spectrum [48, 49, 50, 3, 51, 52, 53, 54, 55, 56, 57, 58, 59, 60, 61, 62, 63, 64, 65, 66, 67]. Since x-rays do not penetrate the Earth's ionosphere, the first x-ray pulsar was not measured until 1968 when the Naval Research Lab launched a rocket which found a pulsar in the Crab nebula [68]. The frequency of pulsations in the x-ray band matched the frequency of observed radio pulsations [68]. In 1977 the Higher Energy Astronomy Observatory (HEAO-1) was launched and found found the first non-pulsating LMXB which [49, 50]. HEAO-1 also conducted a survey to find x-ray sources [2], the results of which are shown in Fig. 2.2. In 1982, the first millisecond pulsar, PSR B1937+21, was found pulsating radio waves [48].

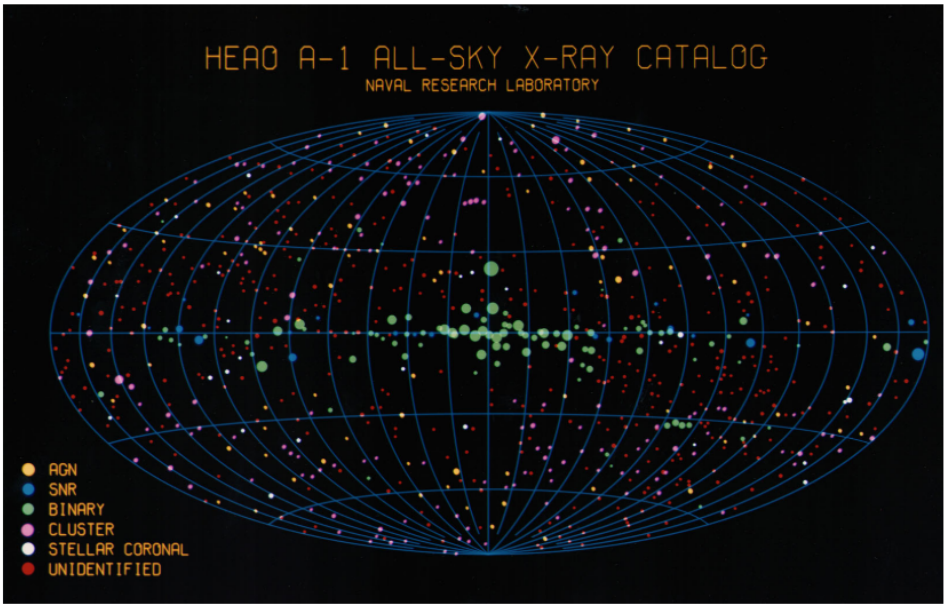

Figure 2.2: X-ray source catalog based on the HAEO sky survey found in [2].

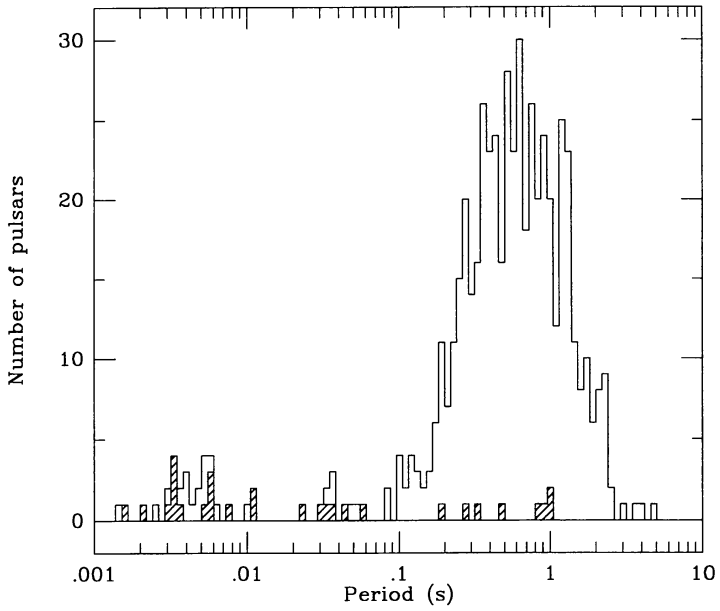

Figure 2.3: Histogram of the first 558 discovered pulsar periods produced by [3].

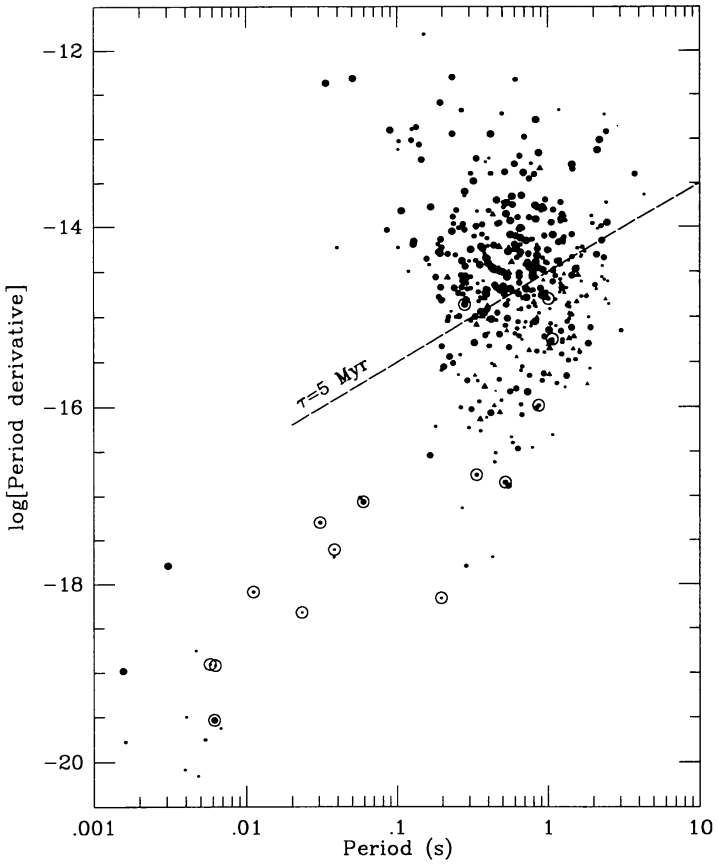

Figure 2.4: Derivative of the pulsar period as a function of the period for 466 identified pulsars [3].

The 1990s saw an increase in the number of in-space x-ray observatories with the launches of Röntgenstrahlen (ROSAT), Advanced Satellite for Cosmology and Astrophysics (ASCA), Rossie X-Ray Timing Explorer (RXTE), Chandra X-ray Explorer, and the Advanced Research and Global Observation Satellite (ARGOS). In 1993 the first millisecond x-ray pulsar was discovered by ROSAT as part of the All-Sky Survey [51]. ROSAT performed all-sky surveys which discovered pulsars of all types located throughout the galaxy [55, 58, 66]. ASCA is the first high-throughput imaging and x-ray spectroscopy observatory [52, 53]. RXTE expanded upon the results of ROSAT with additional sky surveys [54, 56, 69, 57, 62, 65, 66, 67]. Chandra is one of NASA's flagship observatories which can detect very faint x-ray signals [70]. The Unconventional Stellar Experiment, USA, was launched aboard ARGOS to observe bright x-ray sources and evaluate their potential for navigation [71, 72, 73, 2, 74, 37]. A catalogue of all pulsars has been compiled by the Australia Telescope National Facility [75], and updated versions are available online. Future spacecraft such as the Large Observatory for X-ray Timing (LOFT) may further expand these catalogues [76, 77]. An early consolidated catalogue of the first 558 pulsars was compiled by Taylor et al. [3], which was the first consolidation of pulsar catalogues, and showed that a majority of the observed pulsars have a period between 0.1 and 2 s (see Fig. 2.3). This distribution of pulsar periods has remained consistent as more pulsars have been discovered [59]. Furthermore, Fig. 2.4 shows that pulsars with shorter periods have smaller period derivatives implying that the faster a pulsar is spinning the smaller the spin-down rate.

2.1.2 Pulsar Stability

During the observation of pulsars, a pattern of peak pulsation was noted similar to the tick of a clock [24]. This enables the possibility of using a pulsar for timing. The discovery of millisecond pulsars, which emit more stable signals than longer-period pulsars, presented better candidates for timing applications [4]. Rawley et al. investigated the stability of PSR B1937+21 and found that, given a long enough observation interval, the timing stability of the pulsar was comparable to the timing stability of the reference atomic clock [4]. Figure 2.5 shows a comparison of the frequency stability as a function of measurement time for pulsar PSR B1937+21, filled circles, and the reference time, open circle. The dashed line represents a model for the stability of the UTC(NBS) reference time, and the solid line is the locus of frequency stability values that would be observed for a perfect clock measured every 16 days with 300 ns random error. The work of Rawley et al. was extended to more pulsars to generate timing and stability information for each pulsar [78, 65, 79]. As more pulsar stability characteristics were quantified it was found that there is some variance to their

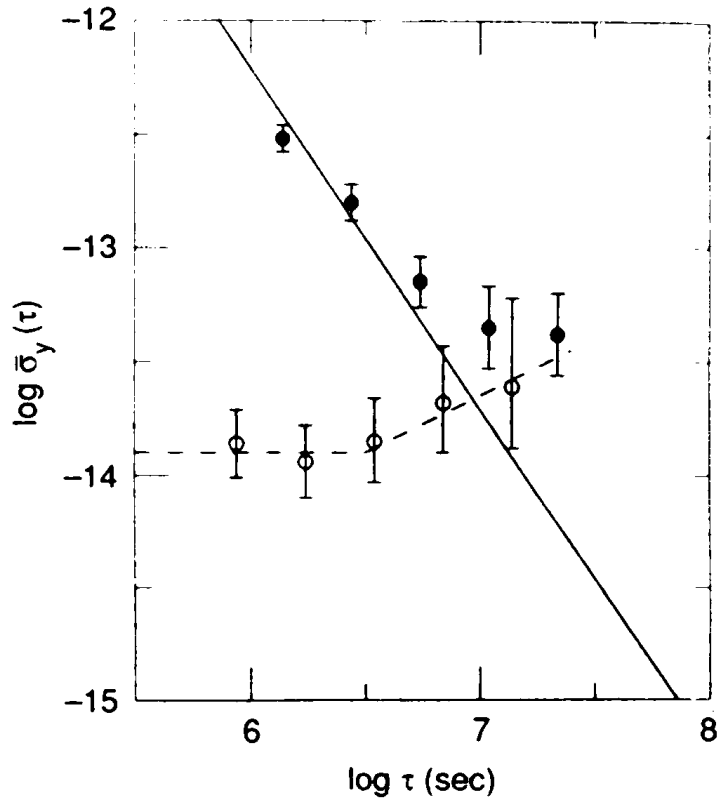

Figure 2.5: Stability of Pulsar PSR B1937+21 compared to the estimated stability of the time standard [4].

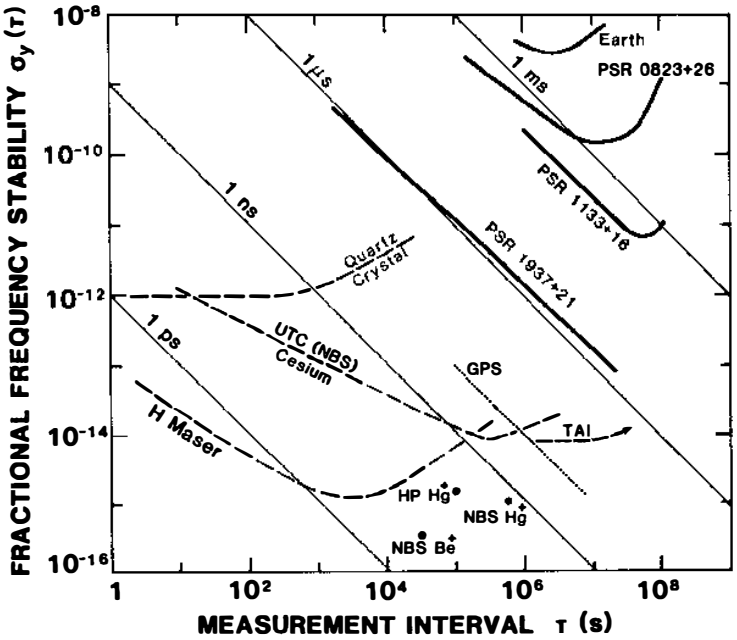

Figure 2.6: Frequency stability of pulsars compared to several different clock types [5].

stability [5]. The stability of pulsars PSR B1927+21, PSR B1133+16, and PSR B0823+26 are plotted along with GPS, a quartz crystal, UTC(NBS), and H Master laboratory clocks (see Fig. 2.6). Over the measurement intervals provided, only pulsar PSR B1937+21 does not begin to drift, all other pulsars and clocks begin to become less stable with increasing measurement time.

2.1.3 Glitches and Noise

Pulsars have been found to have stability comparable to that of an atomic clock, however, pulsars may also exhibit glitches were the period and period derivative changes. The first published glitch was of PSR B0833-45 which had four glitches between 1968 and 1980 [6], as shown in Fig. 2.7. The pulsar had a nominal period of 0.0892 s and was slowing down at a rate of 1.247×10^{-13} ss^{-1}. Each jump caused a relatively instantaneous change in the period and the period derivatives. The change in the period derivatives decayed back to their pre-glitch values over the course of the next 200 days. It was initially believed that these glitch events did not occur in millisecond pulsars until a glitch was observed in pulsar PSR B1821-24 [80]. This glitch was the smallest recorded glitch in a pulsar and remains the only detected glitch in a millisecond pulsar [81, 82]. One potential explanation for this glitch is PSR B1821-24 is young and the glitch is due to the pulsar's formation.

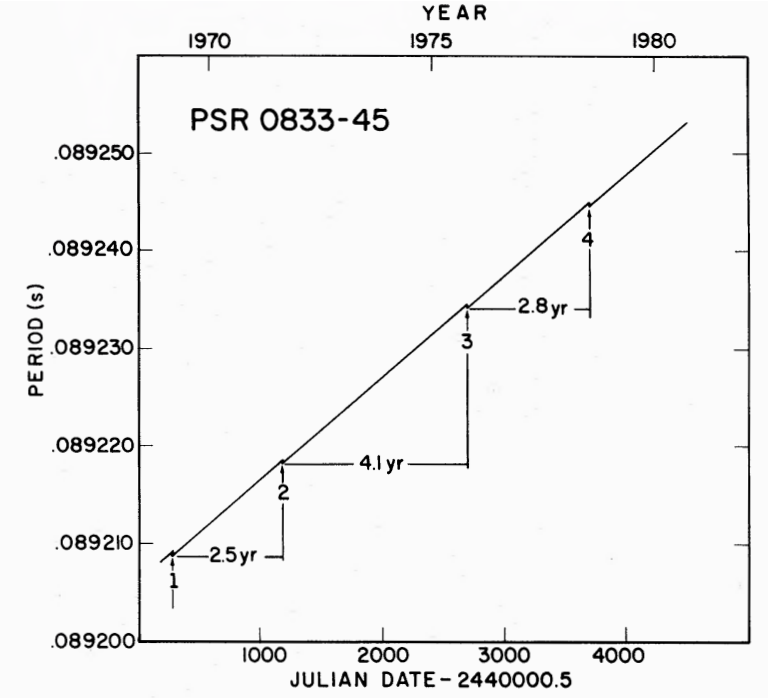

Figure 2.7: Period of pulsar PSR B0833-45 from 1968 to 1980 [6].

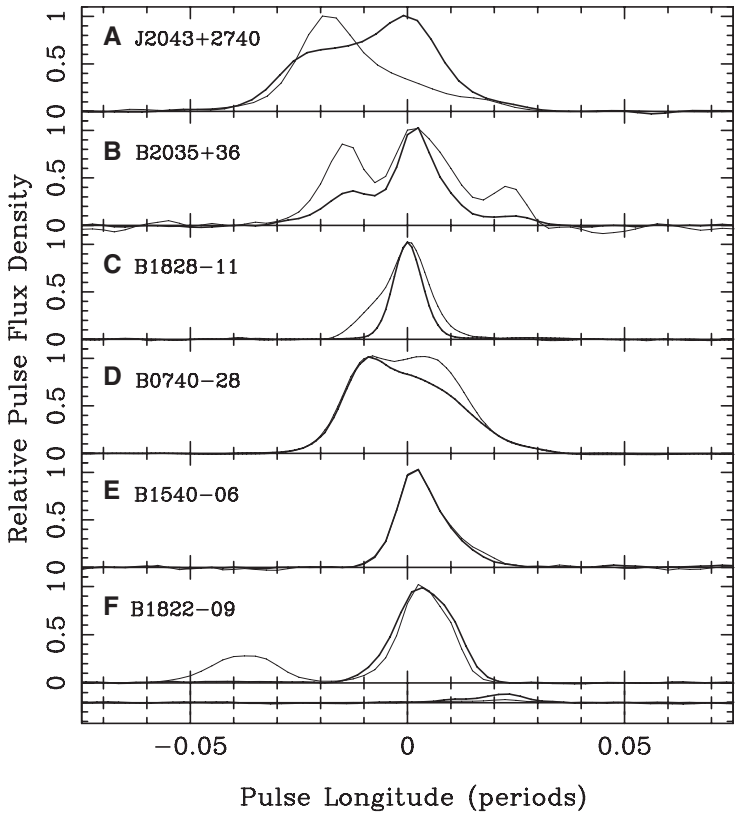

Figure 2.8: The profile for 6 pulsars which exhibited significant changes to their profile in the 1400MHz band [7].

In addition to glitches, pulsars may also exhibit other timing deviations which have are commonly referred to as red noise. It has been postulated that red noise events are quasi-random switches between two different spin down rates [7]. These switches change not only the frequency and its derivatives, but also the shape of the pulsar profile. Figure 2.8 shows two states for the pulse profile of several pulsars which, for some pulsars, can exhibit a significant change. Additionally pulsar PSR B1822-09 had its small pulse shifted by half a period shown at the bottom of Fig. 2.8 [7]. Unlike glitches, red noise is present in millisecond pulsars and radio pulsars, however they are rare occurrences [83, 84].

2.1.4 Pulsar Profile

As pulsars rotate, the intensity of the signal from the pulsar varies in time periodically; a single period of the signal is the pulsar profile. The time-varying intensity of the signal is determined by the alignment of the magnetic field axis and rotation axis as well as the orientation of the pulsar with respect to Earth. Since each pulsar has a different orientation, the profile from each pulsar is unique [8]. The mean pulsar signal profiles for 100 pulsars are presented in [59]. When using the profile of the pulsar it is important to note the frequency at which the measurement is taken.

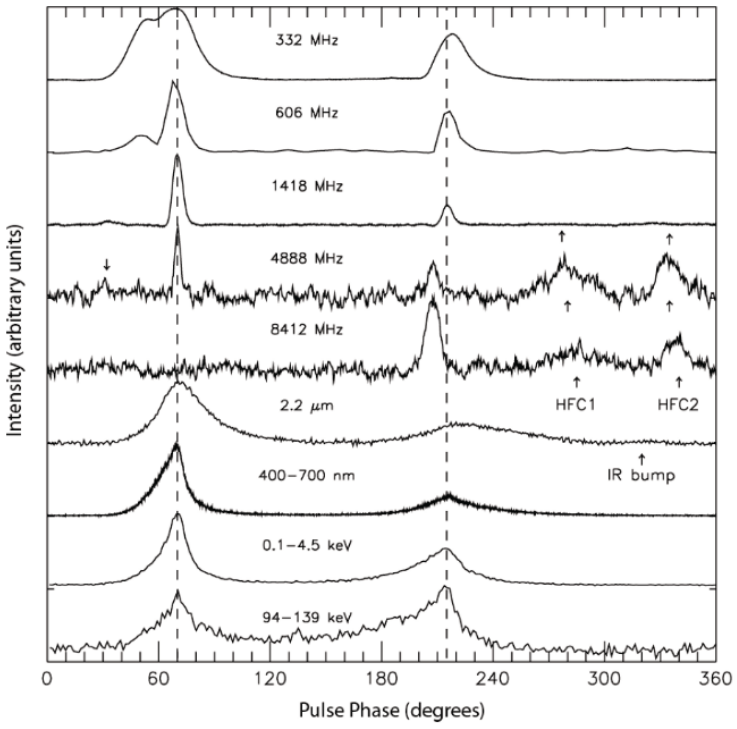

Figure 2.9: Profile for the Crab pulsar across different frequencies [8].

For the same pulsar different measurement frequency bands may produce different pulsar profiles, as shown in signals from the Crab pulsar in Fig. 2.9 [85, 8]. The dashed line indicates the mean peaks across all frequencies with respect to the phase of the Crab pulsar. This mean peak works well for the first peak of the Crab pulsar, however the second peak occurs at different places in the phase at different frequencies.

2.2 Pulsar Modeling

Since pulsars exhibit stability characteristics similar to that of an atomic clock, much work has gone into the creation of models to predict the observed phase at some time in the future. For XNAV applications, most pulsars may be observed for 6 months to a year without the need for model parameter updates. However, some pulsars are less reliable, such as the Crab pulsar, PSR B0531+21, which is far less consistent and whose model parameters must be updated every several days [30, 29] to maintain accuracy. The timing residuals for the Crab pulsar are plotted in Fig. 2.10 along with the residuals generated by an optimal extrapolation [9]. The Crab pulsar deviates from the model quickly; other millisecond pulsars take much longer for significant differences to appear.

Recall that if a pulsar glitches, both the frequency and its derivatives change, it may take up to a year to return to nominal observation. Models have been created to discuss the decay of the glitch terms back to their nominal values in [86], however, since millisecond

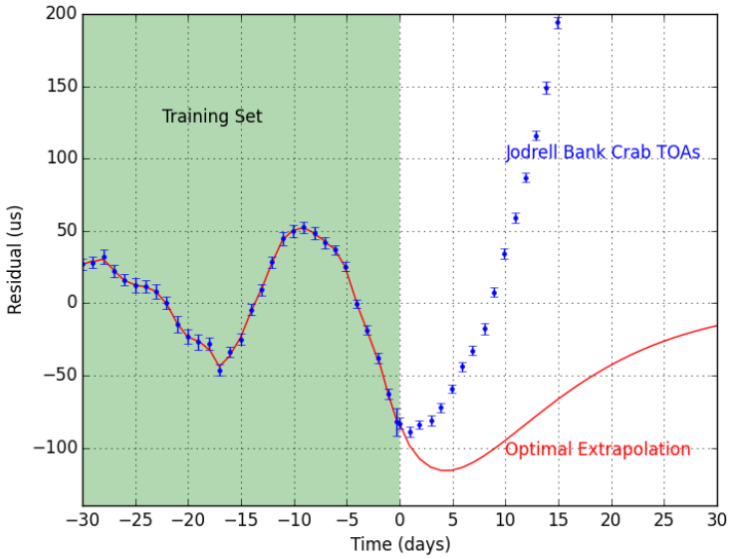

Figure 2.10: Comparison for the timing residuals for the Crab pulsar and an optimal extrapolation [9].

pulsars used for XNAV do not glitch often the glitches will not be discussed here. For XNAV applications red noise variations are small enough that they do not need to be accounted for to achieve the required accuracy for SEXTANT [9]. Red noise models are available in [7, 84].

2.2.1 Phase Evolution of Pulsar Signals

The phase of the pulsar in time may be approximated as a Taylor series expansion about a given point [4, 87],

$$\phi(t) = \sum_{n \geq 1} \frac{\nu^{n-1}}{n!}(t - t_0)^n + \phi_0 \tag{2.1}$$

where t is the proper time of signal which must be modified if the pulsar is in a binary system due to additional binary effects. Any number of frequency derivatives, ν^{n+1}, may be used; however, most studies have truncated the expansion after 3 terms. These derivatives are fitted parameters and may be found from ephemeris sources such as the Jordell Bank Observatory [88], or software packages such as Tempo2. An alternate timing model was developed by Deng et al. [89] which uses a maximum likelihood estimator to estimate the timing residuals given red and white noise covariance.

2.2.2 Time Transformation

Ephemeris databases for pulsar timing are typically referenced to an epoch at the Solar System barycenter (SSB). The Taylor expansion in Eq. 2.1 may be set to coordinate time by converting the time from proper time to coordinate time. This conversion is useful if there is an additional observer not located at the SSB, e.g. a spacecraft, which is measuring the phase of the pulsar. In order to use the frequency and its derivatives the time information from the observer must be converted to the same frame as the ephemeris database. Information on the pulsar time delays may be found in [90, 91, 92, 93, 94, 95, 5, 96, 97, 98] and are combined together in [85, 1, 87, 86, 40]. Deviations of the higher order time delays due to relativistic effects may be found in [99, 40, 100]. The arrival time correction at the barycenter combines the Roemer, Einstein, parallax, and Shapiro delays. Since XNAV applications are for spacecraft, the delays for atmospheric and Solar System dispersion effects will not be included andare neglected for XNAV; the reader is directed to [86] for coverage of those delays. If the observed pulsar is in a binary system additional terms must be included to account for those delays [91, 86]. The Tempo2 documentation has a detailed description of the timing delays [86].

Roemer Delay

The Roemer delay is the vacuum delay between arrival times at the observer and the SSB given by

$$\Delta_R = -\frac{\mathbf{r} \cdot \mathbf{n}}{c} \tag{2.2}$$

where $\mathbf{r}$ is the vector between the observer position and reference position, and $\mathbf{n}$ is the normal vector in the direction of the pulsar.

Einstein Delay

The Einstein delay accounts for the red-shift caused by the gravitational potential of planets in curved space time and is given by

$$\Delta_E = \frac{1}{c^2} \int_{t_0}^{t} \left(U + \frac{v^2}{2} + \Delta L_C^{(PN)} + \Delta L_C^{(A)} \right) \tag{2.3}$$

In Eq. 2.3 the final two terms $\Delta L_C^{(PN)} + \Delta L_C^{(A)}$ represent the time delays due to higher order terms and asteroids respectively. These terms are approximated as constants $\Delta L_C^{(PN)} \approx 1.097 \times 10^{-16}$, and $\Delta L_C^{(A)} \approx 5 \times 10^{-18}$ [97].

Parallax Delay

Since the pulsars are located outside of the Solar System, XNAV often assumess that the pulsars are an infinite distance from the observer. The infinite distance assumption is equivalent to approximating the incoming wavefronts as planes rather than spherical segments. The parallax delay corrects the infinite-distance assumption adding time delays due to the curvature of the signals [95, 5, 86]. Computing the parallax delay requires knowledge of the distance between observers and the distance to the pulsar, $\mathbf{R}_0$,

$$\Delta_P = \frac{\mathbf{r}^2 - (\mathbf{n} \cdot \mathbf{r})^2}{2c\mathbf{R}_0} \tag{2.4}$$

Shapiro Delay

The Shapiro delay is the time delay caused by the pulse moving through curved spacetime. The total delay for all bodies in the Solar System is given by [5],

$$\Delta_S = -2\sum_j \frac{Gm_j}{c^3} ln\left(\mathbf{n}\cdot\mathbf{r}_j + |r_j|\right) + \Delta_{S_2} \tag{2.5}$$

In this equation the term $\mathbf{r}_j$ represents the distance from the observer to each planetary body. The final term Δ_{S_2} is a higher order term which is only important if the observer is very close to one of the planets or the sun and is given by:

$$\Delta_{S_2} = \frac{4G^2m^2}{c^5|r|tan(\psi)sin(\psi)} \approx \frac{4G^2m^2}{c^5|r|\psi^2} \tag{2.6}$$

where ψ is the pulsar-telescope-object angle of the object. For example, using this equation light grazing the solar rim will only have a time delay of 9.1 ns [101].

Binary System Delays

The previous corrections apply to all pulsars. However, if the pulsar is in a binary star system, the binary dynamics affect the light travel time. Four more terms are then added to the timing delays, three of which are Einstein, Roemer and Shaprio delays, the fourth accounts for the aberration of a radio beam from binary motion. This fourth term does not need to be included in the case of XNAV. These terms for binary system delays are complex and do not apply to all pulsars. The reader is referred to [91] for the original work, or to [86] for the application within the Tempo2 timing software.

2.2.3 Non-homogeneous Poisson's Process

The arrival times of photons at the detector may be modeled as a non-homogeneous Poisson process which has a period arrival rate function $\lambda(t) \geq 0$. The arrival rate function is typically written as,

$$\lambda(t) = \beta + \alpha h(\phi(t)) \tag{2.7}$$

where α and β are the effective source and background arrival rates, respectively. The function h is the profile of the pulsar which is normalized to an area of one over one period such that:

$$1 = \int_0^1 h(\phi)d\phi \tag{2.8}$$

The phase ϕ in this equation is the accumulated phase which depends on the initial phase and the velocity of the observer with respect to the pulsar,

$$\phi(t) = \phi_0 + f_s(t - t_0) + \int_{t_0}^{t} f_s \frac{\mathbf{v}(\tau) \cdot \mathbf{n}}{c} d\tau. \tag{2.9}$$

The probability of k photons arriving in a time interval (t_a, t_b) is then a Poisson random variable and is given by Eq. 2.10 [102],

$$P(k; (t_a, t_b)) = \frac{e^{-\int_{t_a}^{t_b} \lambda(s)ds} - (\int_{t_a}^{t_b} \lambda(s)ds)^k}{k!} \tag{2.10}$$

Or as Eq. 2.12 [103] using a mean count rate given in Eq. 2.11,

$$\Lambda(t) = \int_0^t \lambda(s)ds \tag{2.11}$$

$$P(k; (t_a, t_b)) = \frac{e^{-(\Lambda(t_b) - \Lambda(t_a))} - (\Lambda(t_b) - \Lambda(t_a))^k}{k!} \tag{2.12}$$

Simulating this process may be done by either an inversion of the count rate or through thinning [104, 10, 105, 106, 103]. Pasupathy [104] presents an overview of methods for the generating the Poisson random numbers from a non-homogeneous Poisson process. Count-rate inversion methods simulate a standard Poisson process with uniform count rate of 1. The non-homogeneous arrival times are found by substituting these event times into the inverse of the mean arrival rate function. There are several different algorithms which fall under the inversion category and are discussed in detail in Refs. [103, 104, 10], Algorithm 1 is an example of an inversion algorithm from the SEXTANT documentation [103].

Algorithm 1 Inversion

1: Simulate N standard Poisson process event times S_K
2: Transform the time events to phase events $U_k = \Lambda^{-1}(S_k)$
3: Transform from phase back to time domain $T_k = \phi^{-1}(U_k)$

Thinning algorithms [103, 105, 106, 104] may be classified as accept-reject algorithms. Algorithm 2 is an example of a thinning algorithm [106]. The algorithm generates a uniformly distributed random point D (e.g. $D \in U(0, 1)$) and multiples it by the maximum arrival rate $\bar{\lambda}$. If this value is above the arrival rate for the current time no measurement is taken, if it is below the arrival rate for the current time an event has occurred and a measurement is taken. The time is then moved forward by a uniform exponential random variable, and the procedure is repeated.

Algorithm 2 Thinning

Input: $\lambda(t)$, T

Initialize $n = m = 0$, $t_0 = s_0 = 0$, $\bar{\lambda} = \sup_{0 \leq t \leq T} \lambda(t)$
while $s_m \leq$ T **do**
    Generate $u \sim U(0, 1)$
    Let $w = -ln(u)/\lambda$
    Set $s_{m+1} = s_m + w$
    Generate $D \sim U(0, 1)$
    if $D \leq \lambda(s_{m+1})/\bar{\lambda}$ **then**
        $t_n + 1 = s_{m+1}$
        n = n + 1
if $t_n \leq T$ **then**
    return $\{t_k\}_{k1,2,\ldots,n}$
else
    return $\{t_k\}_{k1,2,\ldots,n-1}$

Using these arrival times, an onboard waveform may be constructed to determine an observed phase and frequency. The values for the background radiation arrival rates are typically an order of magnitude larger than the pulsar source arrival rates of interest [107]. This results in not only low signal-to-noise ratio for the x-ray detector, but on average only one photon will be recorded every four to five seconds for a sensor comparable to SEXTANT [107]. Together, these challenges require relatively long observation times and appropriate filtering and estimation algorithms to estimate pulsar phase and frequency.

2.3 X-Ray Signal Measurement and Estimation

In order to determine spacecraft position and velocity on board, an XNAV system must determine pulsar phase and frequency at a given time. These are not directly measurable quantities; instead x-ray detectors measure individual photon arrivals. Photon arrival data are then used to build an onboard representation of the pulsar profile allowing estimation of the pulsar phase and frequency. Photon arrival times can be modeled by a Non-Homogeneous Poisson's Process (NHPP) with a time varying photon arrival rate [108, 109]. These photon arrival times may then be processed with epoch folding or maximum likelihood estimation schemes to generate a phase and frequency estimates whose accuracy depend on the observation time.

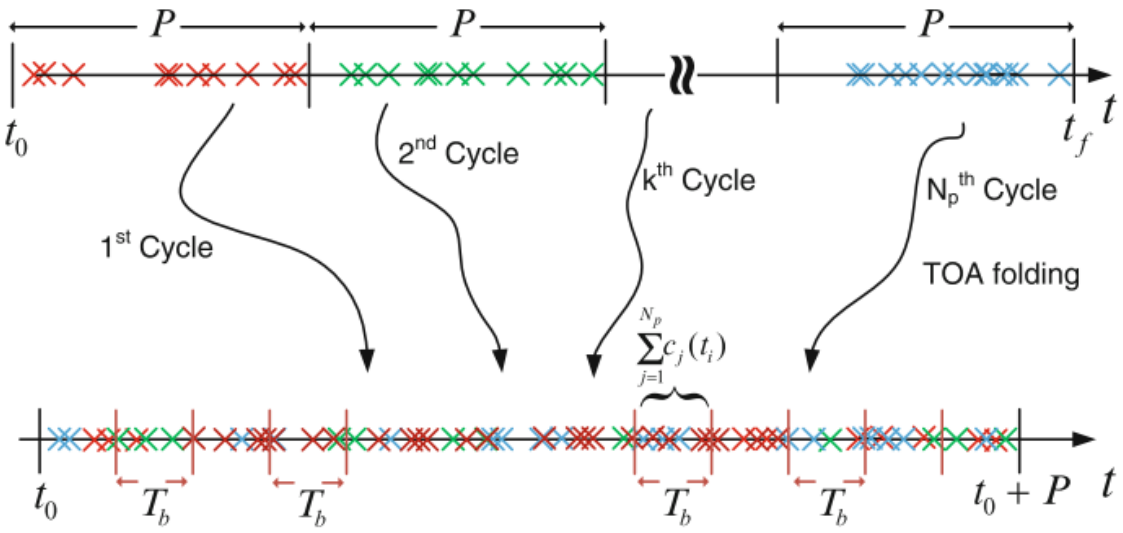

Figure 2.11: Visual representation of Epoch Folding as seen in [10].

2.3.1 Epoch Folding Methods

One method to generate an observed phase and frequency measurement is by using epoch folding, or phase averaging the photons. Since the period of the pulsar is known, the observation interval may be divided into segments where the length of each segment is one period. Each segment is then overlaid one on top of another so that all observation times are between 0 and P, one period. This interval is then subdivided into a number of bins and the number of photons in each bin is summed up and divided by the number of periods measured. A visual representation of this may be seen in Fig. 2.11. If the bin size is too small, statistical error will corrupt the produced waveform; if the bin is too large, information is lost due to averaging. Becker and Trümper [57] present a method for determining the bin size based on the optimal number of harmonics used in the H test. The H test was developed by De Jager et al. for determining the periodicity of a signal for either x or gamma ray astronomy without any light curve information [110]. Their method is built upon a statistical variable Z_m, Eq. 2.13, which quantifies the periodicity of the signal given by the first m harmonics for measurements N. Using Z_m, another statistic variable H, Eq. 2.14, may be computed to find the number of harmonics to include in order to minimize the error between the Fourier series estimator and the unknown light curve, this number is denoted as M. In their work Becker and Trümper present the number of bins as the second expression in Eq. 2.15 where R_i represents Fourier power of the i^{th}. Equation 2.16 is an equivalent form given by Bernhardt et al. [111] in terms of Z_m and m.

$$Z_m^2 = \frac{2}{N}\sum_{k=1}^{m}\left[\left(\sum_{i=1}^{N} cos(k\phi_i)\right)^2 + \left(\sum_{i=1}^{N} sin(k\phi_i)\right)^2\right] \tag{2.13}$$

$$H = \max_{1\leq m<\infty}(Z_m^2 - 4m + 4) = Z_M^4 - 4M + 4 \tag{2.14}$$

$$n = 2.36\left(\sum_{i=1}^{M} i^2 R_i^2\right)^{\frac{1}{3}} \tag{2.15}$$

$$n = 2.36\left[\sum_{m=1}^{M}\frac{1}{2}m^2\left(Z_m^2 - Z_{m-1}^2\right)\right]^{\frac{1}{3}} \tag{2.16}$$

The phase averaged photon arrivals create an onboard light curve given by Eq. 2.17 [109]. In this expression the onboard arrival rate $\breve{\lambda}$ is given in terms of the number of measured periods, N_p, bin size in seconds, T_b, and the number of detected photons in the i^{th} bin, $c(t_i)$. This rate function may may be compared to a known pulsar profile by using non-linear least squares methods as given in Equations 2.18 and 2.19 to generate a phase measurement.

$$\breve{\lambda}(t_i) = \frac{1}{N_p T_b}\sum_{j=1}^{n} c_j(t_i) \tag{2.17}$$

$$\hat{\phi} = \min_{\phi\in\Phi} J(\phi) \tag{2.18}$$

$$J(\phi) = \sum_{i=1}^{N}\left(\breve{\lambda}(t_i) - \lambda(t_i,\phi)\right)^2 \tag{2.19}$$

Information on the mean and variance of the estimator along with more detailed derivations may be found in [108, 109, 10]. Epoch folding has some drawbacks related to velocity estimation. The measured period of the pulsar depends on the frequency, which in turn depends on the observer's velocity through the Doppler shift. The first step of epoch folding is to divide the measurement interval into smaller intervals of one period length. If there is some error in the velocity estimate, as in a real system, then the intervals will not have the correct size leading to photons being placed in incorrect bins, distorting the measured waveform [10]. Emadzadeh and Speyer found that if the velocity error is small enough this contribution will not distort the waveform enough to prevent the reconstruction of the waveform [10, 112].

Epoch folding may also be extended further to incorporate the velocity into the construction of the estimator [113]. First, the spacecraft motion effects are removed by splitting the frequency into two terms, the source frequency and the expected frequency component due

to the spacecraft orbital velocity. The arrival times are then shifted based on the frequency from the orbit. The converted photons have a new period which is the inverse of the difference between the orbital frequency and source frequency. Epoch folding is then executed using this new period to better model the phase in dynamic environments.

The incorporation of compressed sensing into epoch folding methods has also been considered [114]. Compressed sensing is a relatively new signal processing paradigm which recovers a signal from a sparse data set. The basis of this idea is that a few key points may be able to sufficiently represent a larger data set. Compressed sensing theory was applied to x-ray pulsar based navigation in [114] where Li et al. found that their compressed sensing method required one order of magnitude less observation time to detect the signal.

2.3.2 Maximum Likelihood Estimation

An alternative method for phase determination using photon arival times is a maximum likelihood estimator (MLE). While MLE was first discussed for XNAV applicaitons in [39], a clear majority of studies follow the derivation in [11]. A MLE attempts to find model parameters which maximize the likelihood of the observation of a particular signal or pulsar. MLE for XNAV was derived in [11] where the log likelihood function is given by Eq. 2.20, where the summation is of the arrival rate function over measurements k.

$$(\hat{\theta}, \hat{f}) = \max_{\tilde{\theta}\in\theta, \tilde{f}\in\Omega} \sum_{k=1}^{K} \beta + \alpha h(\tilde{\theta}_0 + \tilde{f}(t_k - t_0)) \tag{2.20}$$

Many pulsar shape functions have two peaks, which means that the likelihood function will also have two peaks implying that an exhaustive search of phases should first be conducted. This is used to generate a solution near the global minimum. Gradient based methods may then be used after an initial estimate is generated with a smaller search domain to further refine the estimate [115].

2.3.3 Square Timing Estimation

Along with the derivation of a maximum likelihood estimator in [39], a reformulation of the MLE to a square timing estimator was also developed. The key difference is that the arrival rate function, and likelihood function, may be reformulated in terms of a Fourier series such that,

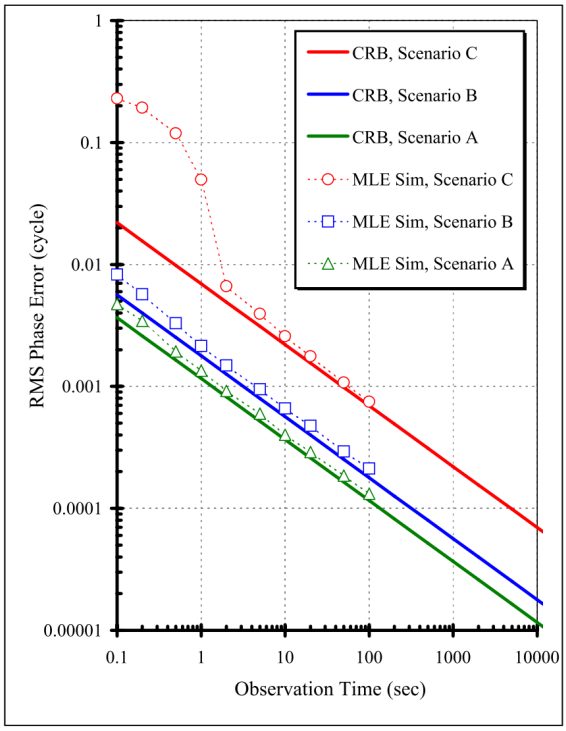

Figure 2.12: Cramer-Rao lower bound for three cases, (A) high source arrival rate, (B) equal source and background rates, (C) high background arrival rate [11].

$$\Lambda(\tau) = \sum_{k=-\infty}^{\infty} c_k \exp\left(j2\pi\frac{k}{T}\tau\right) \tag{2.21}$$

$$c_k = \int_0^T \Lambda(\tau)\exp\left(-j2\pi\frac{k}{T}\tau\right) = \sum_{n=0}^{N-1} \Lambda(n)\exp\left(-j2\pi\frac{k}{N_s}n\right) \tag{2.22}$$

where N_s is the sample number. Sala et al. showed that this method for computing the phase of the pulsar is far more computationally efficient since it only requires $N_s + 1$ evaluations of the likelihood function. The improvement in computational efficiency comes at the cost of a bias in the estimator accuracy. Huang et al. found that a bias of $10^{0.4}$ was added to the minimum variance of the estimator by performing the computation in this manner [116].

2.3.4 Phase Accuracy vs Observation Time

Pulsar signal phase and frequency estimation accuracy generally improves as observation time increases, i.e. as more photon arrivals are recorded. This relationship can be more accurately written using the Cramer-Rao Lower Bound (CRLB) which quantifies a lower bound on the variance of an unbiased estimator. Golshan and Sheikh derived the CRLB for XNAV,

Eq. 2.23 and 2.24, in terms of the pulsar shape function, the derivative of the shape function, source arrival rate, background arrival rate, and observation time [11]. Equation 2.23 shows the CRLB in terms of phase^2 and the Eq. 2.24 in terms of s^2.

$$\mathrm{Var}(\hat{\theta}_0) = \left[T_{obs} \int_0^1 \frac{[\alpha h'(\phi)]^2}{\alpha h(\phi) + \beta} d\phi \right]^{-1} \tag{2.23}$$

$$\mathrm{Var}(\hat{\tau}) = \left[f^2 T_{obs} \int_0^1 \frac{[\alpha h'(\phi)]^2}{\alpha h(\phi) + \beta} d\phi \right]^{-1} \tag{2.24}$$

Since the CRLB depends on the properties of the pulsar, each pulsar will result in a different variance for a given observation time. Lower variance results from pulsars with high source arrival rates compared to the background arrival rate, and pulsars with distinct peaks also help to reduce the variance of the observation. Furthermore, MLE methods for estimating waveforms approach the CRLB as observation time increases, as shown in Fig. 2.12 [11]. Epoch folding via either cross correlation or nonlinear least squares will not reach the CRLB in finite time, but will instead converge to a bias offset [112]. One note here is the MLE convergence to the CRLB is for cases where the velocity of the observer relative to the pulsar is constant. In the presence of acceleration, the MLE will no longer reach the CRLB. If the observer motion is transient enough then shorter observation intervals have been found to give better results than long observations [116].

2.3.5 Phase-Locked Loops

Individually, maximum likelihood estimators or epoch folding may provide a good estimate of the phase and frequency, but these estimates require that the frequency is constant over the observation interval. However, an observer with time varying velocity relative to the pulsar may experience shifts in frequency over the measurement interval. Potential frequency shifts may be accounted for by dividing the observation into smaller intervals where the frequency is nearly constant. These segments may then be recombined with a phase-locked loop. Phase-locked loops compare a measured signal with a reference signal to determine any offsets in phase, frequency, or frequency derivatives. The local model of the signal is then adjusted to synchronize with the observation at which point the signal is considered locked. An overview of phase-locked loops may be found in [117]. The first use of a phase locked loop for XNAV is discussed by Hanson in chapter 5 of his thesis where he uses an analog phase-locked loop to track the phase of the Crab pulsar [13]. The system was shown to lock onto the frequency of the Crab pulsar within 500 s with a steady state time error of 0.0015 s (the Crab pulsar

has a period of 0.033 s).

Digital phase-locked loops (DPLL) originally were more complex than their analog counterpart, until phase-locked loops were reformulated specifically for digital applications by Stephens in 1995 [118]. For definitions of the blocks and general structure of a DPLL the reader is referred to [119]. The first application of a DPLL to XNAV was done by Golshan and Sheikh who constructed a second order DPLL to refine the estimate of a MLE. Their application assumes that the spacecraft velocity with respect to the pulsar is not constant. In such cases their observation is subdivided into smaller blocks of near constant frequency. A MLE then generates a phase estimate over this block, which is passed into a DPLL to generate an updated phase and frequency estimate. This method was proven to work with phase errors tending towards zero using the Rossi X-ray Timing Explorer trajectory along with the actual photon measurements of the Crab pulsar [11]. Anderson and Pines then took this cascaded MLE-DPLL model and tested it on a lab testbed at the NASA Goddard Space Flight Center (GSFC) [107]. With the hardware experiments they were able to show that the MLE was able to obtain an initial phase estimate to within 0.15% for a moving spacecraft with velocity errors. Furthermore the MLE-DPLL cascaded system was able to track the doppler frequency of a spacecraft which was accelerating at 5 km/s^2 [43]. Anderson et al. used an x-ray test bed developed by GSFC to validate their algorithm with hardware generated photon events. For the Crab pulsar it was found that the phase error tended toward zero in 250 s while the frequency error tended toward zero in 100 s [31]. One of the issue with many of the phase tracking studies is that they use the Crab pulsar as a model. The Crab pulsar has photon arrival rates several orders of magnitude larger than other x-ray pulsars. To account for this Anderson and Pines extended the DPLL to a third order DPLL to better track low flux pulsars [120]; their model is able to keep the phase bounded however does not have the same convergence as the cases which used the Crab pulsar.

2.4 X-Ray Pulsar Based Navigation Methods

X-ray pulsar navigation has been developed for a variety of in-space applications. The most prominent aplication has been position estimation. Current XNAV position estimation technology can be subdivided into three categories: relative position, absolute position, or occulation. Aside from position, XNAV may be used to update estimates of spacecraft velocity, time, or attitude. Measurement of each quantity using XNAV presents its own set of challenges and error sources to overcome.

2.4.1 Position Estimation

Occultation

The Unconventional Stellar Aspect (USA) experiment was designed to demonstrate a position determination scheme using the occulation of x-ray sources along the Earth's limb [73, 72]. For bodies with an atmosphere, an atmosphere model is needed to account for photon disturbances through events such as refraction, winds, or weather. If these effects can be accounted for then the measured photon signal may be fit to the atmospheric model. Knowing the radius of the planet's disk, the time the source is occulted can be used to determine the spacecraft position relative to the planet [40]. The in-track satellite position may then be determined, with an expected accuracy of 350 m. A few hundred observations may then improve the resulting accuracy to 10s of meters [73]. Unfortunately the atmospheric models were not mature enough to yield any meaningful results on position determination via x-ray occulation [71]. X-ray occulations have also been proposed for navigation at other celestial bodies such as the moon [73].

Absolute Position

Sheikh et al. proposed a method for determining an absolute position estimate by measuring multiple pulsars simultaneously [40, 42]. Specifically, the methods assumes there is one unique observer position which satisfies the phase evolution for all measured pulsars. Four pulsars may be observed over a given observation interval. The intersection of three sets of planes from the first three pulsars may be found. The set of planes from the fourth pulsar may be evaluated at the intersection of the first three pulsars, and the point with the smallest distance to the fourth pulsar is considered the position. One drawback is that the phase measurements produce an underdetermined system. The spacecraft position is unknown, and each pulsar measurement adds an additional unknown in the pulsars phase. The system then becomes a system of N equations with N+3 unknowns. Within his dissertation Sheikh has proposed several methods to evaluate each cycle combination to determine which set is the most likely solution to the spacecraft position [40].

Relative Position

The first and most prominent position update method in the literature is a relative position update. By measuring photons from a known pulsar for a sufficient length of time a phase estimate for the pulsar may be generated. This phase estimate may be compared to the

same pulse measurement at a different location to produce a phase error. The error in phase may be converted to an error in position in the direction of the pulsar. To generate a full position state update at least 3 pulsars must be observed [25]. There are two distinct relative position measurement strategies. In the first case both observers are spacecraft and a relative position between the two spacecraft is computed. In the other case, one of the observers is set to the epoch of an ephemeris database. In the second case the computed relative position vector is between the epoch of the ephemeris database and the spacecraft. The epoch of the ephemeris database is typically located at the SSB or the center of the Earth.

In the first case a relative position between two spacecraft is computed by comparing the time taken for a pulsar signal to reach each satellite. The difference in observation may be converted to a relative range between the two spacecraft in the direction of the pulsar. For satellites in a constellation it was found that the computing phase offsets between satellites produces smaller position errors compared to using the SSB or Earth. The resulting position estimation has an error on the order of 100 m [33]. For this technology to work, the highly stable millisecond x-ray pulsars are not required. There are other variable x-ray sources which do not have any repeating waveform, but have a high source intensity. So long as the signal is time varying, peaks in the intensity of observed photons may be observed and their times recorded. If both spacecraft measure the same peak, then any difference in the time of observation is used to generate the position update [121].

The second option is to set one of the observers at an ephemeris database epoch such as the Solar System barrycenter or the Earth's center. At the ephemeris epoch, models must be constructed to predict what the phase should be as a function of time. The spacecraft observer then records photon arrivals and the arrival times are shifted to the frame of the ephemeris database. In order to do so, the navigation system requires the use of an initial position estimate, on-board clock, and pulsar models to calculate the required time shift and resolve any cycle ambiguities. The predicted phase is then compared with the observed phase to generate a position error. Overviews of the relative position solution framework where one observer is set to an ephemeris database epoch have been provided in [10, 122, 40, 41]. This method of relative position determination has been documented more extensively in the literature than all others.

Relative position determination XNAV is often compared to the Deep Space Network to determine at which point the expected accuracy of XNAV surpasses the DSN [35, 123]. When pulsar selection is based on noise characteristics alone it was found that a XNAV system would be more accurate than the DSN at 5.5AU from Earth [123]. However, when considering errors in the pulsar location it was determined that XNAV is more accurate than the DSN only beyond 15AU from Earth [35]. Although XNAV surpasses the expected

accuracy of the DSN at these points, an initial position estimate is still required. Like the absolute position determination scheme, the relative position will have an undetermined set of equations to solve. It is proposed that the initial position estimate only needs to be within half a phase to to allow relative position determination to work [124].

2.4.2 Velocity

The velocity of the spacecraft may be estimated by comparing the measured frequency of the pulsar with a known source frequency. The two are then related by a Doppler shift in the wavelength which may be solved for velocity.

$$f = \left(1 + \frac{\Delta v}{c}\right) f_o \tag{2.25}$$

$$\Delta f = \frac{\Delta v}{c} f_0 \tag{2.26}$$

This form of the Doppler shift is a linear approximation which is not entirely accurate for XNAV applications since higher order relativistic terms are not included. The time shifts to convert the pulsar time to the spacecraft time may be differentiated to determine higher order Doppler effects on the frequency, as presented in [116, 125]. Huang et al. found that the differentiation resulted in 28 terms for the pulsar frequency which was then reduced to six main terms with a contribution larger than 0.01 m/s to the velocity error. These terms are related to the second order Roemer delay, Shapiro delay, and three binary Roemer delay terms [116].

2.4.3 Attitude Determination

X-ray astronomy may also be used to determine observer attitude. In position estimation, a measured signal is compared to a reference to determine an offset in position. To estimate attitude, the detector must measure x-rays in a particular field of view and compare to a known catalogue of the area, similar to a star tracker. This is done by observing across a section of the sky and measuring the response. If the detector is well collimated there should be a time varying intensity of photons as the detector moves across a source. This process should be repeated to give full attitude information [73]. One key benefit here is that there are far fewer bright x-ray sources compared to the visible spectrum. This means that the required catalogue of x-ray sources is small, reducing the computing requirements. Since there are fewer sources and these sources are farther apart source confusion becomes less of

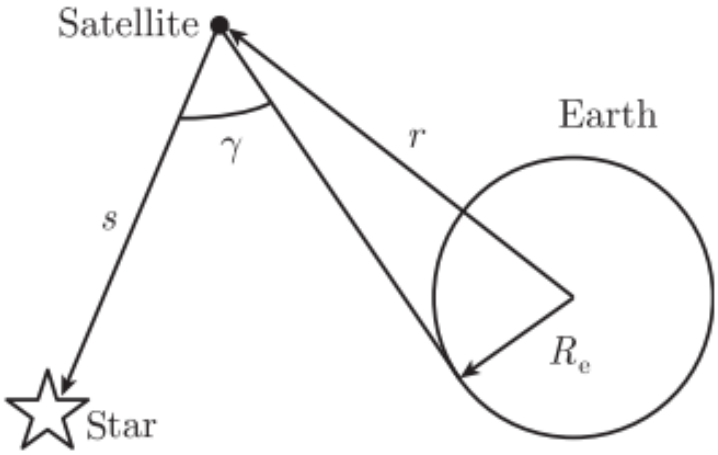

Figure 2.13: Geometric relationship between a CNS measurement and the observed bodies [12].

a problem. Furthermore, pulsation in some x-ray sources may also be used as a additional means to identify specific sources [13].

2.4.4 Integrated Systems

While XNAV has the potential to be a completely autonomous system for deep space navigation, XNAV may also be a means to reduce required communication with Earth-based systems through integration with existing on-board navigation technologies. Woodfork proposed the first integration solution by combining XNAV and GPS measurements [32], which resulted in marginal improvements in position estimation performance. Woodfork found that in order to generate more meaningful position updates the x-ray detector accuracy needs to be significantly improved. Integration work has moved away from using GPS and instead studied the potential benefits of integrating with the DSN, or with a celestial navigation system, CNS. Integration with the DSN has been studied by Sheikh et al. to determine missions which would benefit from XNAV support [126]. Measurement accuracies for the DSN can be broken down into radial and non-radial accuracies [127]. The radial measurements are a range measurement from an antenna on the Earth's surface whereas the non-radial measurement is derived from the angle at which the antenna is pointing. The expected error of the angular measurement provide a large component of the error in the non-radial direction and grows by approximately 4 km per AU from Earth [34]. Integration of XNAV with the DSN may present a better navigation solution that either method independently.

An active area of research is the integration of XNAV with a celestial navigation system

(CNS) [12, 128, 129]. A celestial navigation system measures the angle between a star and the horizon of a known body. The geometric relationship between the observed angle and the distance form the planet is shown in Fig. 2.13. Integrating XNAV and CNS again provides better position estimation than either system independently. The initial study by Liu et al. found that integration would result in a 33% improvement in position accuracy over CNS alone. For a high Earth orbit application, the RMS position error was found to be larger than 200 m for CNS alone, however system integration as able to reduce this to below 100 m [128].

2.4.5 Filter Development

Over the past 15 years the application of the Kalman filter for the XNAV estimation problem has improved the estimated position update accuracy while also allowing for new ways to integrate XNAV into other navigation systems. The first application of a Kalman filter for XNAV was presented by Sheikh in [130], with a more concise version in [40]. Both of these works used an extended Kalman filter to better capture the non-linearities in the state dynamics. This work was then extended to an Earth orbiting spacecraft to take the Earth's shadowing effect into account which limits the pulsar observation intervals [41]. Ju et al. found that using multiple sensors to measure pulsars simultaneously along with multirate processing may improve position estimation by up to 50% [131]. These efforts determined position relative to a given epoch; an implementation of an extended Kalman filter for the relative position between two satellites is shown by Kai et al. in [33].

Chen et al. integrated epoch folding into an extended Kalman filter in an attempt to remove some of the noise from the position and velocity estimation [132]. Four methods are compared in the study: an extended Kalman filter provides the baseline performance, two variations which incorporate epoch folding, and the last converts the measurement into a Fourier series. This Fourier series measurement is called quadrature formulation which is essentially the square timing estimation model presented in [39]. The analysis concluded that the quadrature formulation was not a good candidate for deep space applications. Huang et al. also studied the squared timing estimation formulation for a satellite in geostationary orbit, and found that the loss of accuracy may be justified by a reduction in the required computation time [116]. The study also examined the use of a second order Kalman filter to remove the use of a DPLL. The authors found that by properly selecting gains, the noise in the MLE-DPLL cascade may be removed without increasing the phase error.

Several different methods for integrating XNAV into other navigation systems have been proposed each with their own type of filter. The original proposal for integration of XNAV

with a CNS by Liu et al. also proposed the use of a federated unscented Kalman filter [12]. The federated filter is used to fuse the measurements of the two systems while the unscented estimation improves performance for non-linear dynamics. Further development of the XNAV CNAS integration lead to the proposal of an augmented state unscented Kalman filter [133]. This filtering process is the same as an unscented Kalman filter, however the state vector is augmented with a system bias and clock bias. Rather than using a single filter for the integrated measurement, Wang et al. proposed the use of a kinematic and static filter [128]. Here the CNS measurement is fused with the dynamics in a kinematic filter whose output is then combined with the XNAV measurement in a static filter. Both filters use an unscented transformations to estimate the non-linear dynamics, however the authors acknowledge that linearization may be done for computational considerations. Results showed that, using the non-linear dynamics, the position of a satellite in high Earth orbit may be estimated within 100 m. For a derivation of the error for a mixed XNAV/CNS system refer to [129].

If the x-ray detector is capable of measuring the photon angle of arrival, Runnels and Gebre-Egziabher proposed an integrated system which estimates both the spacecraft attitude and position simultaneously using a joint probabilistic data association filter [134]. The photon angle of arrival allows the filter to estimate the spacecraft attitude and if the attitude is recursively estimated the system them behaves as if it knows from which source the photons are originating. This allows the joint filter to more closely approximate an ideal estimator.

Implementing a Kalman filter requires the use of an error model which depends on the error sources being considered. The two largest sources or error are in the clock and the knowledge of the pulsar direction. Clock errors may incorrectly time tag photons leading to a bias in the phase estimate while errors in the pulsar direction apply the state update in an incorrect direction. An overview of the clock errors is presented by Sheikh [40]. Ashby and Howe recognized that higher order relativistic terms are not always negligible in the clock error models [135]. To simplify computations a linearized reformulation of the clock dynamics is presented by Chen et al. in terms of an intermediate variable which depends on the clock noise and pulsar timing noise [132].

The second large error source of error is the direction of the pulsar relative to the observer. XNAV is sometimes presented as a means to obtain the same position accuracy everywhere in the Solar System. This is not possible for a relative position estimate because the pulsar position error is a function of distance from the Solar System barrycenter [35, 30]. Graven et al. presents an error analysis where the XANV update error is related to the error in phase from the three pulsars and the error in the position of the pulsars [35]. This study found that the position error may grow by up to 5 km at 100 AU from the Solar System barrycenter.

Note that this study presents figures of the position error in terms of the detector size. Hanson et al. found that the error in the pulse estimate is inversely proportional to the product of the observation time and square root of the detector area [136].

Deng et al. presented a study of XNAV under various scenarios [124], including whether the spacecraft has its trajectory information, if the measurements are simultaneous, clock drift, potential glitches, and if the system is autonomous. The simulation measured 4 pulsars every 7 days and determined that for a trajectory from Earth to Mars the position may be determined to approximately 20 km depending on the included errors.

2.4.6 Pulsar Selection

The majority of studies choose a candidate set of pulsars based on which set gives the best estimate of phase as predicted by the CRLB. This may not always be the case. As discussed in the previous section the error in pulsar location increases with distance from the Solar System barrycetner [35]. The expected error for each pulsar changes at a difference rate which may change the set of observed pulsars. In a study by Shemar et al., the authors found that at 30 AU the best set of pulsars is PSR B1937+21, B1821-24, and J0437-4715. However at 1.5AU the set PSR B1937+21, B1821-24, and J1012+5307 provides the best accuracy and could be used with similar accuracy at 30AU without updating the timing model as frequently [30]. For missions which do not communicate with Earth, the pulsar-based time standard must be used which requires the observation of more pulsars [137].

One way to determine which pulsar should be observed is to look at the observability of the system. The observability of XNAV is presented in two different ways by Chen at al [132] for an autonomous spacecraft, and Ning et al. [129] for an integrated XNAV/CNS system. The method by Chen et al. preforms an analysis for a simplified system which is linear, has constant velocity, no timing noise, constant clock bias, and only the Roemer delay (geometric time shift). In this model the authors found that each pulsar observation increased the rank of the observability matrix by 1 which resulted in a full rank matrix after 3 different observations. An analysis of the resulting information matrix was conducted, where the size of the information was maximized by measuring pulsars in the opposite direction of the spacecraft motion [132]. The second method as derived by Ning et al. conducted the observably analysis under a piecewise constant model. Rather than looking at the rank of this matrix the authors instead looked at the condition number of the observability matrix. By integrating XNAV into a CNS the condition number was reduced by 66%. To minimize the condition number the authors found that pulsars either in the same, or opposite, direction as the CNS body should be observed; as the angle between the measurements increases the

error increases exponentially [129].

Alternatively, some studies pick pulsars based on the observation characteristics. Each pulsar has a different phase estimate for a given observation interval as defined by the CRLB. The CRLB depends on the pulsar profile, arrival rates, and observation time [11]. Chen et al. found that pulsars which had a high frequency, high peak intensity, low noise, large fourier coefficients for higher order minimized the error covariance [132]. The state update then strongly depends on the pulsars selected where the bounds on position update may vary from 5 km to over 200 km based only on pulsar selection [111]. The orientation of the pulsars also plays a role in the overall position update. As the measurements become more parallel the intersection of the error bands forms a larger area than if the measurements are orthogonal. This is a representation of the geometric dilution of precision (GDOP). Several studies evaluated the GDOP for pulsars [30, 1, 99, 40]. Shemar et al. found that the lowest GDOP for the considered pulsars is 1.7 and is achieved by pulsars PSR B1821-24, J1012+5307, J0437-4715, and J0030+0451 [30]. This candidate set had a position accuracy of 75 km whereas the best set, PSR B1937+21, B1821-24, and J0437-4715 had an accuracy of 35 km. It is therefore a combination of the orientation of pulsars with the expected phase accuracy. Shemar et al. also composed a table of candidate pulsars and ranked them based on the accuracy of the position estimate [30]. An analysis of the uncertainty, x-ray spectra, arrival rates, and orientation of candidate SEXTANT pulsars is presented in [9].

When considering pulsar selection for integrated systems there does not seem to be any consensus on how many pulsars to observe. Woodfork found that for an integrated GPS/XNAV system observing one pulsar accurately is better than observing pulsars less accurately [32]. Liu et al. came to the same conclusion for a XNAV/CNS integrated system [12]. Wang et al. found that observing 3 pulsars with three 0.3 m^2 detectors is better than observing one pulsar with a 1.0 m^2 detector [138]. There is no clear consensus for the number of pulsars to observe in an integrated system since the number seems to depend on the implementation and filter being used.

2.5 Hardware Implementation

Currently there have been three missions which sought to use x-ray pulsar navigation: the Unconventional Stellar Aspect (USA), X-ray Pulsar Navigation-1 (XPNAV-1), and Station Explorer for X-ray Timing and Navigation Technology (SEXTANT). The SEXTANT experiment is using the same x-ray optics as the Neutron Star Interior Composition Explorer, NICER. The USA and SEXTANT/NICER experiments are both payloads on a larger sys-

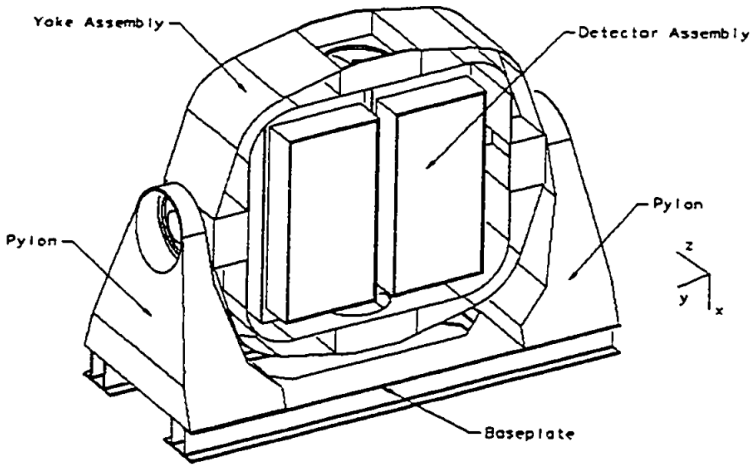

Figure 2.14: Drawing of the USA experiment as found in [13].

tem, whereas XPNAV-1 is an entire satellite.

2.5.1 Flight Systems

USA/ARGOS

The first mission which sought to use x-ray pulsars for navigation purposes was ARGOS. ARGOS carried the USA payload which was designed to use x-ray occulation to estimate the spacecraft position [72, 73]. A technical description of the USA payload is provided in [13] and an image of the payload is presented in Fig. 2.14. As previously mentioned position determination via x-ray occulation was unsuccessful since atmospheric models were not accurate enough to give a meaningful position update [71]. The mission instead proved that x-ray pulsars may be used for attitude determination. Hanson proposed a method for attitude determination by sweeping over x-ray sources [13] which was implemented on ARGOS. Shortly after ARGOS was operational, errors in the spacecraft attitude were discovered. To resolve the issue Hanson's attitude determination was implemented on ARGOS, which corrected the spacecraft attitude issue on August 18, 1999. The analyses suggested that the spacecraft roll angle was 1° out of alignment [74]. Although the spacecraft had the capability to preform the correction autonomously all data analysis was conducted on the ground [71].

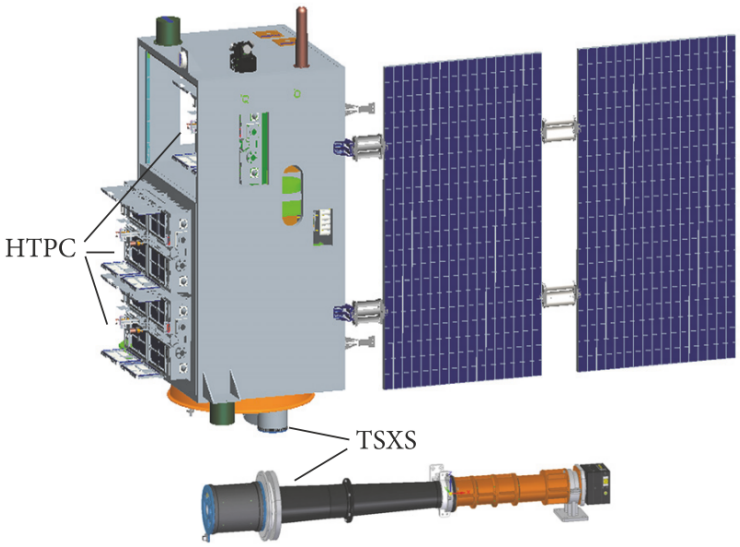

Figure 2.15: Schematic of XPNAV-1 [14].

XPNAV-1

The next XNAV mission launched was XPNAV-1 on November 10, 2016, Fig. 2.15. XPNAV-1 is the first of three phases of the China Academy of Space Technology (CAST), XNAV space demonstration. XPNAV-1 was launched to validate the capability of observing pulsars in space. The second phase is to launch another satellite which will generate more data and test navigation algorithms onboard. The third phase is a constellation of satellites [14]. XPNAV-1 was launched on a sun-synchronous orbit which allows it to observe one of 8 candidate pulsars. Four of the candidate pulsars are millisecond pulsars while the other four are x-ray binaries. The recorded data is analyzed to determine the energy of the photons, the number of source and background photons, time conversions to the Solar System barrycenter, and construction of an epoch folded profile. It is expected that the next mission, whose goal is to test XNAV algorithms, will launch within 3-5 years [14].

NICER/SEXTANT

The NICER/SEXTANT system is funded through the NASA Science Mission Directorate and Space Technology Mission Directorate. The NICER x-ray instruments were installed aboard the international space station in June 2017. The joint payload requirements are driven by NICER which seeks to further explore the composition of neutron stars. NICER is looking to use pulse timing to enable mass measurements, discover a maximum pulsar spin rate, determine long term clock stability, and determine the seismology of neutron stars.

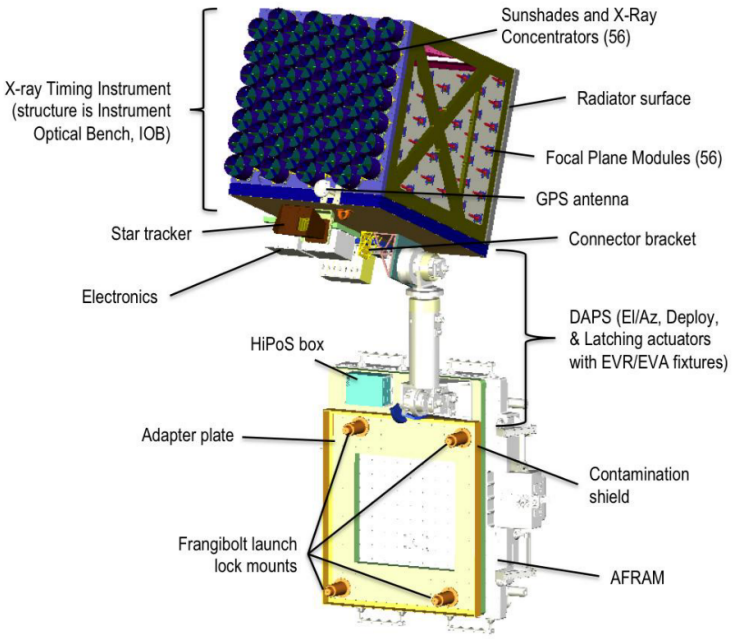

Figure 2.16: Schematic of NICER [15].

In order to achieve these goals, the NICER instrument was designed to measure the light curve state, Shapiro delays, search for periodic pulsation in the submillisecond scale, measure pulse arrival times monthly, and distinguish between thermal and non-thermal spectra [15]. Information on the hardware components may be seen in [139], and a rendering of the NICER payload may be seen in Fig. 2.16. SEXTANT's goal is to demonstrate real-time on-orbit XNAV-only orbit determination using the unmodified NICER flight hardware [137]. Successful orbit determination is achieved if the position error remains below 10 km in the worst direction, with a stretch goal of estimating the position error within 1 km. A secondary goal is to further explorer the pulsar clock stability and its potential for spacecraft clock synchronization.

SEXTANT was sent to determine the position of the International Space Station on orbit using the measured photons from NICER's x-ray timing instrument. Descriptions of SEXTANT XNAV algorithms are documented in [103, 107, 115]. The recorded photons will be processed through a MLE to generate a phase and frequency model. The MLE on SEXTANT will also allow estimates of the source and background arrival rates since these parameters may change with position and time. The phase estimation is conducted by finding the maximum of the likelihood function through an exhaustive search. The estimate is refined by taking the exhaustive search maximum then preforming Newton iterations on a restricted domain to better approximate the phase [115]. The estimated phase and frequency will be compared to a first order predictive model [107]. The Crab pulsar is another object of

interest since it has a high flux of photons requiring far less observation time. The photons signal processing was adjusted in the event of observations of the Crab pulsar [115]. In the event of a glitch SEXTANT will stop the measurement and update the pulsar model prior top measuring new photons [107].

The SEXTANT experiment started with an initial GPS measurement which is degraded prior to running a XNAV algorithm [107]. Initial models of SEXTANT predicted that the estimation should keep the root-sum-squared error to within 5 km [107, 115]. The SEXTANT flight experiment showed that the error remained within the 10 km goal for majority of the experiment. Near the start of the observation there is a point where the error rose above the 10 km threshold to over 15 km prior to dropping down. This error growth follows the propagation of the initial state before the system recovers and quickly reduces the error [28]. Future experiments will observe the Crab pulsar which will require model updates in order to accurately capture the noise characteristics. The model extensions are presented in [29] along with simulated results.

2.5.2 GXLT

Prior to implementation on SEXTANT, the algorithms were first tested on the GSFC X-ray Navigation Laboratory Testbed (GXLT). The GXLT has three modes of operation, one mode passes a phase and frequency measurement to the flight software, another simulates photons arrivals and passes those. The final mode is a hardware in the loop mode where x-ray events are generated by shinning a ultraviolet light emitting diode to remove electrons from a photocathode [107]. A reference signal is generated by Tempo2 and compared to the phase and frequency measurements to generate the position update. More details of the testbed may be found in [107, 115].

Aside from the SEXTANT algorithm verification the GXLT was used to test other models for XNAV. Anderson and Pines were able to test some of the advancements in XNAV [43], including the first experimental use of the DPLL for XNAV. As part of their experiments the GXLT was used with a time varying frequency and it was found that if the Crab pulsar may be used the estimation can give good results. These tests were done for the case where the source has a higher arrival rate than background, equal arrival rates, or a small source arrival rate. Based on the SEXTANT documentation the source arrival rate is much lower than the background arrival rate [107]. These tests provided a baseline for the SEXTANT experiments.

2.5.3 Sensor Technology

While most studies look at improving algorithms to process photons, some have considered possible improvements to the sensor technology [140, 141, 30]. Bernhardt et al. presents an overview of x-ray telescopes for navigation [141]. A key issue with the telescopes is the required mass per effective area, since as the angular resolution decreases the mass per effective area increases. Shemar et al. recognize that much of the literature on high time resolution sensing is centered around collimated detectors, however XNAV concepts use imaging detectors [30]. Imaging detectors tend to record less of the background noise while having a smaller, and simpler, detector. The main drawback is additional constraints on the pointing requirements. The study also presents some design considerations for future XNAV instruments. Revnivstev et al. studied how potential improvements in sensor technology would impact the XNAV accuracy of 1000 s of x-ray data from RXTE [140]. By increasing the detection band to 1 keV the position determination may improve to 450 m from 730 m, while an increase in detector size from 0.6 m^2 to 1.0 m^2 may further improve the accuracy to 350 m.

2.6 Summary

XNAV is a strong candidate for improving navigation capabilities on future autonomous spacecraft, especially for deep space applications which may have limited communication with Earth-based systems. XNAV technology is currently mature enough that several flight experiments have been conducted to test feasibility on spacecraft. As XNAV technology improves both in the available hardware and algorithms used for processing, XNAV will likely become a more desireable space navigation technology option for future space missions. In particular, XNAV may improve spacecraft autonomy, improve robustness and accuracy when integrated with other navigation technology, and provide improved navigation accuracy for missions to the outer Solar System and beyond.

CHAPTER 3

XNAV CANDIDATE STATE DETERMINATION

The majority of XNAV implementations to date are designed to operate under a relative position update framework. A key limitation of relative position update framework schemes is that they require an initial position estimate. Without that estimate, the photon time of arrivals can not be shifted back to the reference epoch. Sheikh et al. developed an alternate solution strategy called absolute position determination [42]. This method uses measurement difference to construct a set of wavefronts for each pulsar measurement. The spacecraft location must be at a point where all wavefronts intersect. Sheikh et al. postulated that this method would require simultaneous measurement of multiple pulsars; using current technology, simultaneous measurement requires multiple gimbaled detectors.

This chapter characterizes how candidate intersections, and therefore candidate spacecraft positions, evolve with measurement error, number of observed pulsars, and the selected set of pulsars observed with the application to the absolute position determination method. The problem formulation for the intersection of infinite sets of lines, or planes, is presented along with criteria to determine candidate set intersections. An analytic solution to the mixed-integer math problem is shown for a simplified test case. A numeric algorithm to rapidly determine candidate solutions is presented in both two and three dimensions. Using candidate XNAV pulsars, the number of candidate solutions for a given domain are found using various measurement accuracies and number of pulsars measured.

3.1 Identification of Candidate Positions in Two Dimensions

During the XNAV state update process, the onboard navigation system generates a phase offset with respect to an expected phase. A position update can be generated based on the phase offset, a first order approximation of which is given by,

$$\frac{\mathbf{n} \cdot \Delta\mathbf{r}}{v_c} = \Delta t \tag{3.1}$$

Here the position update, $\mathbf{n} \cdot \Delta\mathbf{r}$, is in the direction of the pulsar, see Fig. 1.1. Since the

distance between pulsars and our Solar System is large, pulsars are assumed to be infinitely far from the Solar System, making the pulsar waveform appear to propagate as a plane. The time delay caused by the curvature of the wavefront is given by,

$$dt = \frac{|\mathbf{r}_\perp|^2}{2v_c|\mathbf{R}|} \tag{3.2}$$

where $\mathbf{R}$ is the distance to the pulsar, and $\mathbf{r}_\perp$ is the perpendicular component of the spacecraft position with respect to the pulsar direction [86]. The nearest millisecond pulsar to Earth is at a distance of 157 parsecs [75] which corresponds to 4.84451×10^{15} km or 3.24×10^{7} AU. For spacecraft operating within the Solar System, approximately 80 AU diameter, we assume the time delay correction term is negligible.

The problem can be further simplified to two dimensions (2D) for the following reasons:

1. Most in-space trajectories are planar, and the plane of motion may be determined using velocity state information also available from XNAV [142].

2. The three-dimensional candidate solution identification problem quickly reduces to finding intersections of lines, a feature preserved in two dimensions.

3. Computational time required to determine candidate intersections is significantly reduced in two dimensions.

Figure 3.1 illustrates the candidate position identification problem in two dimensions: the lines are the projections of notional pulsar wavefronts in 2D. Each pulsar observation generates a candidate spacecraft position somewhere on an infinite set of lines. The intersection of two measurements reduces the spacecraft position to an infinite set of points, and each measurement afterwards reduces the number of points, but the set of candidate positions remains infinite for an unbounded domain. Figure 3.1(a) shows candidate spacecraft positions at the intersections of two observed pulsar wavefronts; Fig. 3.1(b) shows the reduced number of intersections resulting from three pulsar wavefronts. Error in the pulsar position estimate is assumed to be independent of position in the domain.

In this section, consider the following pulsars to determine position: J0218+4232, J0030+0451, B1937+21, B18218-24, and J0437-4715 (see Table 3.1). These are the pulsars used for NASA's Station Explorer for X-ray Timing and Navigation Technology (SEXTANT) experiments [28]. The search domain for the spacecraft position is restricted to a square with sides of length 2×10^{10}m (approximately 0.134 AU) unless otherwise noted. This domain size, when centered at Earth, encompasses all of cislunar space, as well as the Earth-Sun L_1 and L_2 points, for reference see Fig. 3.2.

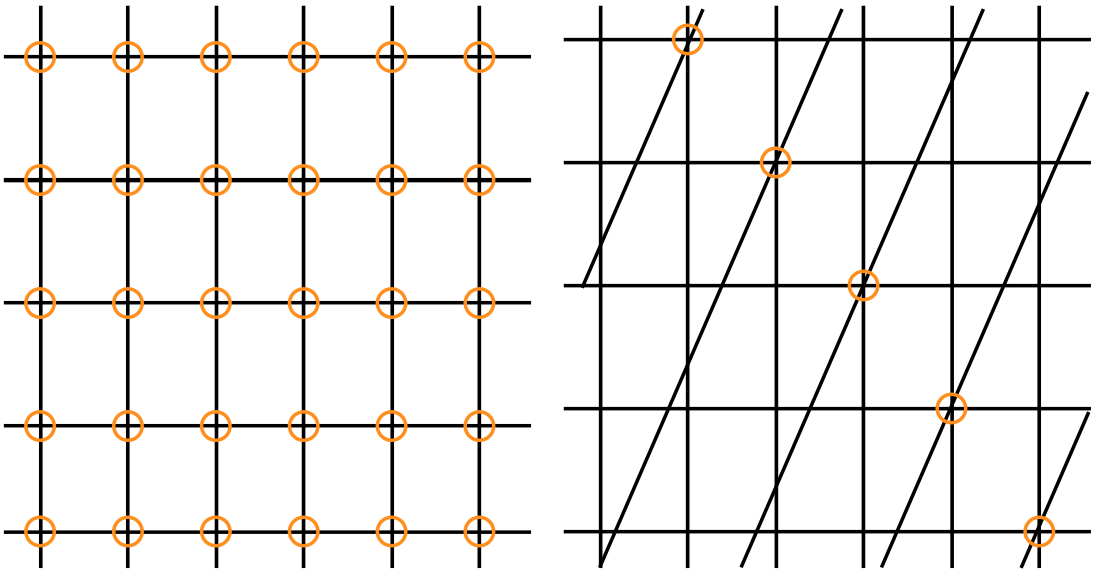

(a) (b)

Figure 3.1: The intersection of (a) two sets of lines and (b) three sets of lines.

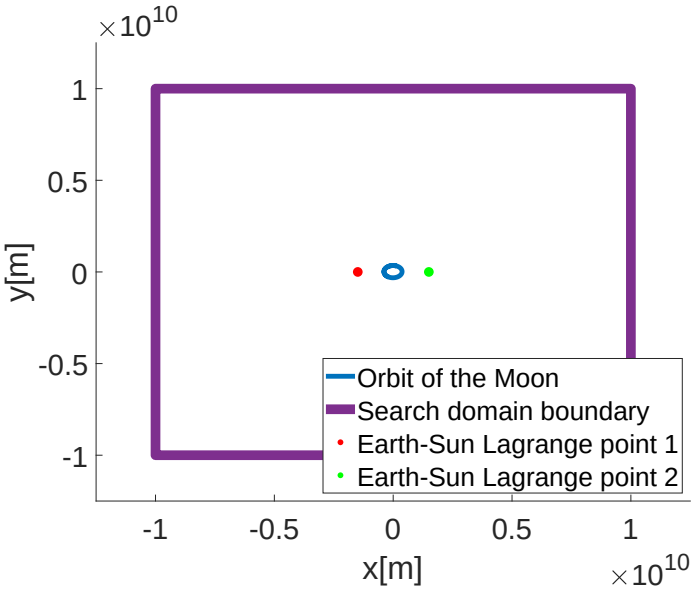

Figure 3.2: Visual representation of the search domain with the orbit of the moon.

Table 3.1: Candidate Pulsar Properties.

Pulsar	1	2	3	4	5
Name	J0437-4715	B18218-24	J0218+4232	B1937+21	J0030+0451
Period [s]	0.0058	0.0031	0.0023	0.0016	0.0049
Normal Vector	$\begin{bmatrix} -0.2594 \\ 0.9355 \\ 0.2397 \end{bmatrix}$	$\begin{bmatrix} -0.0449 \\ 0.9943 \\ 0.0969 \end{bmatrix}$	$\begin{bmatrix} 0.5570 \\ 0.5668 \\ 0.6070 \end{bmatrix}$	$\begin{bmatrix} 0.1549 \\ -0.9070 \\ 0.3917 \end{bmatrix}$	$\begin{bmatrix} 0.0840 \\ 0.1325 \\ 0.9876 \end{bmatrix}$

Candidate intersections may be found by modeling observed pulsar wavefronts as lines. The standard form of a 2D line is given by,

$$ax + by = c \tag{3.3}$$

where c characterizes the line, and is defined by a point on the line:

$$c = ax_0 + by_0 \tag{3.4}$$

A set of lines for each pulsar measurement corresponding to the signal wavefronts may be defined and used to generate a system of equations, all of the form,

$$a_p x + b_p y = c_i \tag{3.5}$$

where i is the index of a wavefront from a pulsar. The intersection of two pulsar wavefronts is given by,

$$\begin{bmatrix} a_1 & b_1 \\ a_2 & b_2 \end{bmatrix} \begin{bmatrix} x \\ y \end{bmatrix} = \begin{bmatrix} c_1 \\ c_2 \end{bmatrix} \tag{3.6}$$

where the normal vector components are given by,

$$\mathbf{n}_p = \begin{bmatrix} a_p \\ b_p \end{bmatrix} \quad p = 1:2 \tag{3.7}$$

Equation 3.4 is the dot product of the normal vector with a point on the plane. The point on the plane is the normal vector multiplied by the distance between wavefronts, or the wavelength. For a given wavefront, the constant, c, is given by,

$$c_i = cT_p i = \lambda_p i \tag{3.8}$$

The periods, T_i, are the corresponding 2D period of the pulsar wavefront. When projecting the wavefronts from 3D into a 2D plane, the corresponding wavefronts may have a smaller wavelength and therefore period. The period may be found by computing the angle between the normal vector and the z-axis using a dot product, then multiplying the sine of this angle by the period of the pulsar. Additionally, a phase offset may be added to the index to enable wavefront placement at any point in the domain.

$$c_i = \lambda_p(i + \phi_p) \tag{3.9}$$

For each additional observed pulsar, the (x, y) candidate point must satisfy Eq. 3.5 for the new pulsar. The set of Eq. 3.6 for a given set of pulsars results in an under-determined problem. The intersection of N pulsars has N equations, but $N+2$ unknowns. N unknowns are from the required index i to identify the line, and 2 unknowns for the (x, y) candidate intersection location.

3.2 Analytic Candidate Determination

The candidate position identification problem can be written as a mixed-integer programming problem, which provides a closed-form analytic solution for exact intersections of lines. The solution presented below follows the form of Bowman and Burdet [143] whose solution represents the mixed-integer problem as an equivalent linear Diophantine problem. The solution to this class of problem may be found using reflexive generalized inverses, as shown by Hurt and Waid [144]. First, the problem is express the problem in the required form. For XNAV, the system of equations given by Eq. 3.6 and 3.9 may be combined to form the set of equations,

$$\begin{bmatrix} a_1 & b_1 \\ a_2 & b_2 \end{bmatrix} \begin{bmatrix} x \\ y \end{bmatrix} = \begin{bmatrix} \lambda_1(i_1 + \phi_1) \\ \lambda_2(i_2 + \phi_2) \end{bmatrix} \tag{3.10}$$

If a fourth pulsar is added to the system, an additional row is added to the matrix equation,

$$\begin{bmatrix} a_1 & b_1 \\ a_2 & b_2 \\ a_3 & b_3 \end{bmatrix} \begin{bmatrix} x \\ y \end{bmatrix} = \begin{bmatrix} \lambda_1(i_1 + \phi_1) \\ \lambda_2(i_2 + \phi_2) \\ \lambda_3(i_3 + \phi_3) \end{bmatrix} \tag{3.11}$$

Each additional pulsar observed would add a row to the matrix equation. The standard form of a mixed integer problem is given by,

$$A\mathbf{m} + B\mathbf{s} = \mathbf{q} \tag{3.12}$$

where $\mathbf{m}$ is a vector of integers, $\mathbf{s}$ is a vector of scalars, and $\mathbf{q}$ is a vector of rational numbers. Equation 3.11 may be rearranged into this form and is given by Eq. 3.13, where $\mathbf{m}$ is a vector of integer indices, $[i_1, i_2, i_3]^T$, and $\mathbf{s}$ is the spacecraft position, $[x, y]^T$.

$$\begin{bmatrix} \lambda_1 & 0 & 0 \\ 0 & \lambda_2 & 0 \\ 0 & 0 & \lambda_3 \end{bmatrix} \mathbf{m} + \begin{bmatrix} a_1 & b_1 \\ a_2 & b_2 \\ a_3 & b_3 \end{bmatrix} \mathbf{s} = \begin{bmatrix} \lambda_1\phi_1 \\ \lambda_2\phi_2 \\ \lambda_3\phi_3 \end{bmatrix} \tag{3.13}$$

Closed-form solutions to equations of this form have been found for some cases [143]. The solutions are built around a reflexive generalized inverse of B, denoted as $B^{\#}$. A reflexive generalized inverse is not the same as a pseudo-inverse. The conditions for a pseudo-inverse are given by,

$$BB^{-1}B = B \tag{3.14}$$
$$B^{-1}BB^{-1} = B^{-1} \tag{3.15}$$
$$(BB^{-1})^T = BB^{-1} \tag{3.16}$$
$$(B^{-1}B)^T = B^{-1}B \tag{3.17}$$

To be a reflexive generalized inverse, only the first two conditions are required. One important note is that for a reflexive generalized inverse, $BB^{\#}$ or $B^{\#}B$ is not necessarily equal to the identity matrix. If a reflexive generalized inverse of B can be found, then a pair of intermediate quantities may be defined,

$$D = (I - BB^{\#})A \tag{3.18}$$
$$\mathbf{d} = (I - BB^{\#})\mathbf{q} \tag{3.19}$$

If the following set of conditions are satisfied:

$$D^{\#} \text{ is integral} \tag{3.20}$$
$$D^{\#}\mathbf{d} \text{ is integral} \tag{3.21}$$
$$DD^{\#}\mathbf{d} = \mathbf{d} \tag{3.22}$$

Hurt and Waid derived an analytic solution, given by Eq. 3.23 and 3.24 [144].

$$\mathbf{m} = D^{\#}\mathbf{d} + (I - D^{\#}D)\mathbf{w} \tag{3.23}$$
$$\mathbf{s} = B^{\#}\mathbf{c} - B^{\#}AD^{\#}\mathbf{d} - B^{\#}A(I - D^{\#}D)\mathbf{w} + (I - B^{\#}B)\mathbf{z} \tag{3.24}$$

where $\mathbf{w}$ is a vector of arbitrary integers and $\mathbf{z}$ is an arbitrary vector of real numbers. Any combination of integers in $\mathbf{w}$ or real numbers in $\mathbf{z}$ will result in a solution to the mixed-integer problem. The length of the vectors $\mathbf{w}$ and $\mathbf{z}$ is equal to the number of measurements considered.

To test the mixed-integer programming solution in 2D, consider pulsars with normal vec-

tors $[1,0]^T$, $[3/5,4/5]^T$, $[-4/5,3/5]^T$. For simplicity, the period and speed of light are normalized to 1, making the A matrix equal to the identity matrix and $\mathbf{c}$ a vector of ones. The problem being considered is given by:

$$\mathbf{m} + \begin{bmatrix} 1 & 0 \\ 3/5 & 4/5 \\ -4/5 & 3/5 \end{bmatrix} \mathbf{s} = \begin{bmatrix} 1 \\ 1 \\ 1 \end{bmatrix} \tag{3.25}$$

A reflexive generalized inverse of B which solves this problem is:

$$B^{\#} = \begin{bmatrix} 1 & 0 & 0 \\ -3/4 & 5/4 & 0 \end{bmatrix} \tag{3.26}$$

The resulting $\mathbf{d}, D$, and $D^{\#}$ are given by:

$$\mathbf{d} = \begin{bmatrix} 6 \\ 0 \\ 0 \end{bmatrix}, \quad D = \begin{bmatrix} -5 & 3 & -4 \\ 0 & 0 & 0 \\ 0 & 0 & 0 \end{bmatrix}, D^{\#} = \begin{bmatrix} 1 & 0 & 0 \\ 2 & 0 & 0 \\ 0 & 0 & 0 \end{bmatrix} \tag{3.27}$$

Using these parameters, the solution to Eq. 3.25 is:

$$\mathbf{m} = \begin{bmatrix} 6w_1 - 3w_2 + 4w_3 + 6 \\ 10w_1 - 5w_2 + 8w_3 + 12 \\ w_3 \end{bmatrix} \tag{3.28}$$

$$\mathbf{s} = \begin{bmatrix} 6w_1 - 3w_2 + 4w_3 + 7 \\ 8w_1 - 4w_2 + 7w_3 + 11 \end{bmatrix} \tag{3.29}$$

By substituting integer values into w_1, w_2, w_3, the candidate positions $\mathbf{s}$, may be determined along with the pulsar index $\mathbf{m}$. In this case, $BB^{\#} = I$ makes the problem independent of $\mathbf{z}$, the vector of arbitrary numbers. One drawback of the analytic solution is that the candidate position vector is a 2x1 vector (3x1 for 3 dimensional problems) and the w vector will be an Nx1 vector, where N is the number of pulsar measurements used. Therefore, there is not a one-to-one correspondence between combinations of w_i and $\mathbf{m}$; thus, a given candidate position may correspond to multiple $\mathbf{w}$ vectors.

Figure 3.3 shows the pulsar wavefronts; all analytic solutions are highlighted as orange dots. In this case, each w_i is varied independently from -10 to 10, resulting in 21^3 different values of $\mathbf{w}$ and 9261 candidate solutions. Within the desired domain, Eq. (3.28-3.29) identify only 77 candidate solutions (the orange dots) of the 84 total solutions. The remaining

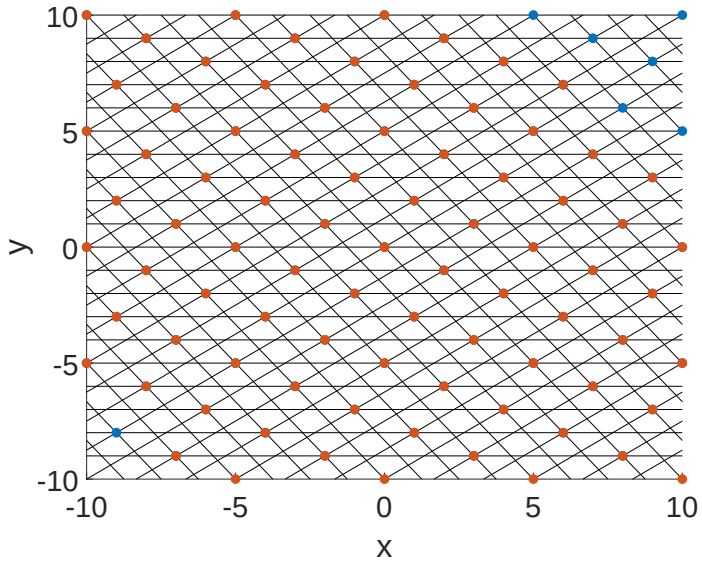

Figure 3.3: The intersection of three sets of lines are presented where the orange dots are analytically found intersections and the blue dots are additional intersections which were found numerically.

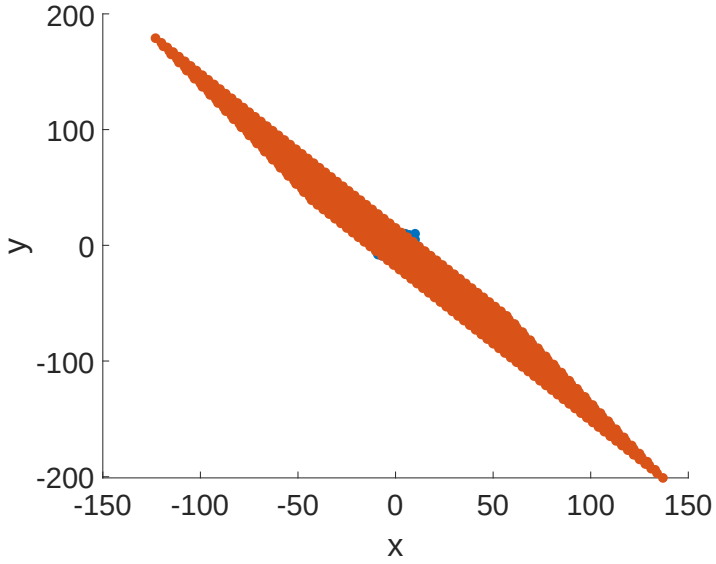

Figure 3.4: Analytic solutions to the mixed integer problem.

unidentified 7 solutions are shown as blue dots. Since there is no one-to-one correspondence between $\mathbf{w}$ and $\mathbf{m}$, there is no guarantee that all solutions in a given domain will be identified. Furthermore, there is no guarantee that each unique $\mathbf{w}$ will result in a new solution: of the 9261 analytic candidate solutions only 1281 are unique. Figure 3.4 shows additional solutions which are found by the analytic method that lie outside of the domain in question, resulting from the selection of $\mathbf{w}$. Therefore, while analytic solution yields a closed-form expression for the intersection of multiple sets of lines in terms of a single parameter $\mathbf{w}$, there is no way to know what combinations of $\mathbf{w}$ are required in order to capture all solutions within a desired domain. Also, this method can only determine exact solutions, meaning there is no way to incorporate the measurement error presented in a real XNAV system.

3.3 Numeric Candidate Determination

In a realistic scenario there will be some error in the measurement of the photons emitted from the pulsar. Error in this measurement will result in some phase error when comparing the measured signal to a reference. Phase measurement errors can be converted into a linear distance by,

$$\Delta\mathbf{r} = v_c \phi T \mathbf{n} \tag{3.30}$$

where c is the speed of light, ϕ is the phase error, and T is the period of the pulsar. Using the pulsars in Table 3.1, and phase errors of 10^{-3}, 10^{-4} and 10^{-5} the corresponding errors in position are on the order of 1 km, 100 m and 10 m respectively.

The error in phase may be defined by the Cramer-Rao lower bound, Eq. 2.24, which places a bound on the variance of an unbiased estimator. Golshan et al. derived this quantity for pulsar based navigation in terms of the observation time, T_{obs}, pulsar waveform, h, the derivative of the waveform, h', and the source, α, and background, β, photon arrival rates [11]. For a given pulsar this expression relates the observation time with the phase error.

$$\mathrm{Var}(\hat{\phi}_0) \geq \left[T_{obs} \int_0^1 \frac{[\alpha h'(\phi)]^2}{\alpha h(\phi) + \beta} d\phi \right]^{-1} \tag{3.31}$$

All of the terms within the integral are constant for a specific pulsar and may be computed for a given source and background photon arrival rate, which simplifies the expression in terms of an integration parameter, I_P.

$$\mathrm{Var}(\hat{\phi}_0) \geq [T_{obs} I_p]^{-1} \tag{3.32}$$

Table 3.2: Required Observation Time to Achieve the Desired Phase Tolerance for Each Pulsar.

	Pulsar				
	1	2	3	4	5
Phase Tolerance	J0218+4232	J0030+0451	B1937+21	B18218-24	J0437-4715
10^{-3}	1.79×10^{5}s	1.85×10^{5}s	4.29×10^{4}s	4.19×10^{3}s	3.45×10^{5}s
10^{-4}	1.98×10^{7}s	1.85×10^{7}s	4.29×10^{6}s	4.19×10^{5}s	3.45×10^{7}s
10^{-5}	1.79×10^{9}s	1.85×10^{9}s	4.29×10^{8}s	4.19×10^{7}s	3.45×10^{9}s

Ray et al. computed these integration parameters for the pulsars in Table 3.1 [9]. The required observation time in order to generate a measurement with the above accuracies has been computed for each pulsar and can be seen in Table 3.2.

Using these error characteristics, measurement error may be applied to the problem of finding intersections of pulsar wavefronts. The domain size is set to a square domain wide sides of length 2×10^{10} m to adequately capture the structure of candidate solutions while minimizing computational expense. Within this domain, sets of three, four and five pulsars will be considered from Table 3.1. In this chapter, if three pulsar measurements are used the first three pulsars will be considered, pulsars 1-3, if a fourth measurements is used pulsar 4 is added to the set, and if five measurements are used pulsar 5 is added. The phase accuracy will be set to be between 10^{-3} and 10^{-5}. The minimum phase accuracy is set to 10^{-3} so that the Cramer-Rao lower bound more closely matches the SEXTANT experimental data, Fig. 3.5 [9]. The solid lines represent the Cramer-Rao lower bound, and the data points are obtained from NASA's SEXTANT. Additionally, all measurements are assumed to be concurrent to allow for the calculation of intersections, without the need for time-based corrections. To enforce a solution within the domain, no phase offset is given for any of the pulsars, resulting in a solution at the origin, which for these cases is the only exact solution.

3.3.1 Intersection of Pulsar Wavefronts in a Bounded Domain

Prior to evaluating pulsar intersections, first the number of wavefronts within a given domain must be found. For a square domain this can be done by taking the dot product of the pulsar normal vector with each corner of the domain. Then this value can be divided by the pulsar wavelength to determine the number of wavefronts required to reach each corner. This process is then repeated for each pulsar observation used as their normal vectors and wavelengths will both impact the required number of wavefronts to search through.

In order to begin the numeric evaluation of pulsar intersections, first the intersection of two wavefronts must be computed by solving Eq. 3.6 for the candidate position. This

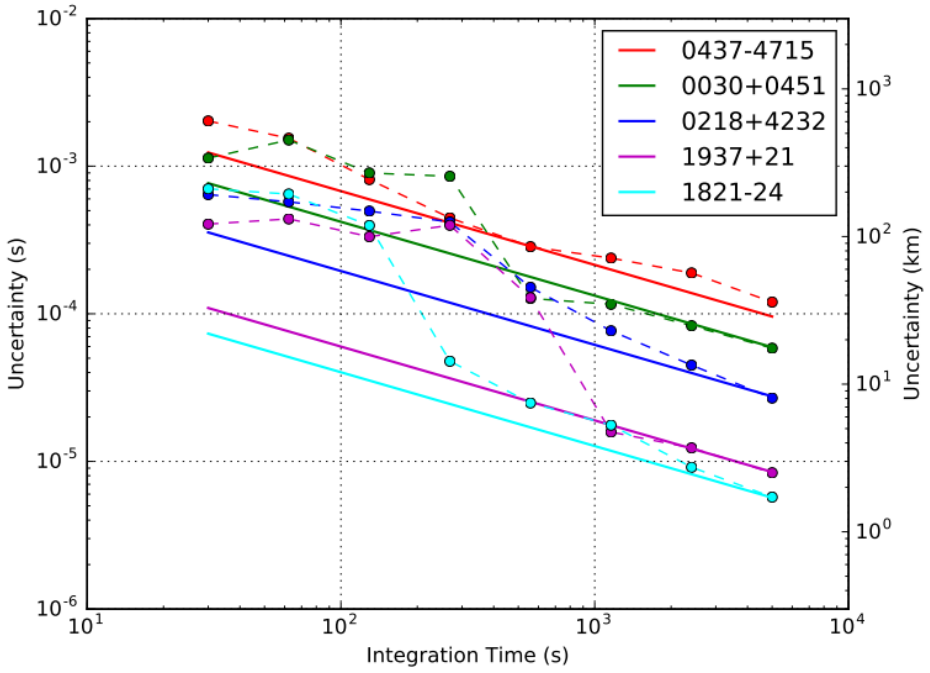

Figure 3.5: Measurement uncertainty vs observation time of pulsar measurements from SEXTANT [9]. The data points are observation accuracy from SEXTANT with dashed lines connecting them, and the solid lines show the estimated Cramer-Rao lower bound.

Table 3.3: Normal vector combinations for fictitious pulsars.

Case	(A)	(B)	(C)	(D)	(E)
Normal Vectors	$\begin{bmatrix}1\\0\end{bmatrix}, \begin{bmatrix}0\\1\end{bmatrix}$	$\begin{bmatrix}1\\0\end{bmatrix}, \begin{bmatrix}0.7\\0.7\end{bmatrix}$	$\begin{bmatrix}1\\0\end{bmatrix}, \begin{bmatrix}-0.89\\0.45\end{bmatrix}$	$\begin{bmatrix}0.7\\0.7\end{bmatrix}, \begin{bmatrix}0.45\\0.89\end{bmatrix}$	$\begin{bmatrix}1\\1\end{bmatrix}, \begin{bmatrix}0.9999\\0\end{bmatrix}$

can be done by calculating the c_i values for each wavefronts in the domain by Eq. 3.9 and substituting it into Eq. 3.6. A matrix inverse is then used to find the each candidate position for each combination of wavefronts. This process may be completed for each combination of wavefronts within the defined boundary, but may not always be necessary. The only case where each combination must be evaluated is the case where the the pulsar normal vectors are aligned with the edges of the domain. For other pulsar wavefront orientations, some combinations may result in candidate positions which lie outside the considered domain.

Consider a pair of fictitious pulsars whose wavelengths are 1, and a square domain with a side length of 200. Figure 3.6 shows the candidate position for each index combination for the normal vector combinations in Table 3.3. Here the blue dots are candidate positions within the domain and the red dots are candidate positions outside of the domain. Only in the case where the normal vectors are aligned with the Cartesian coordinates are all

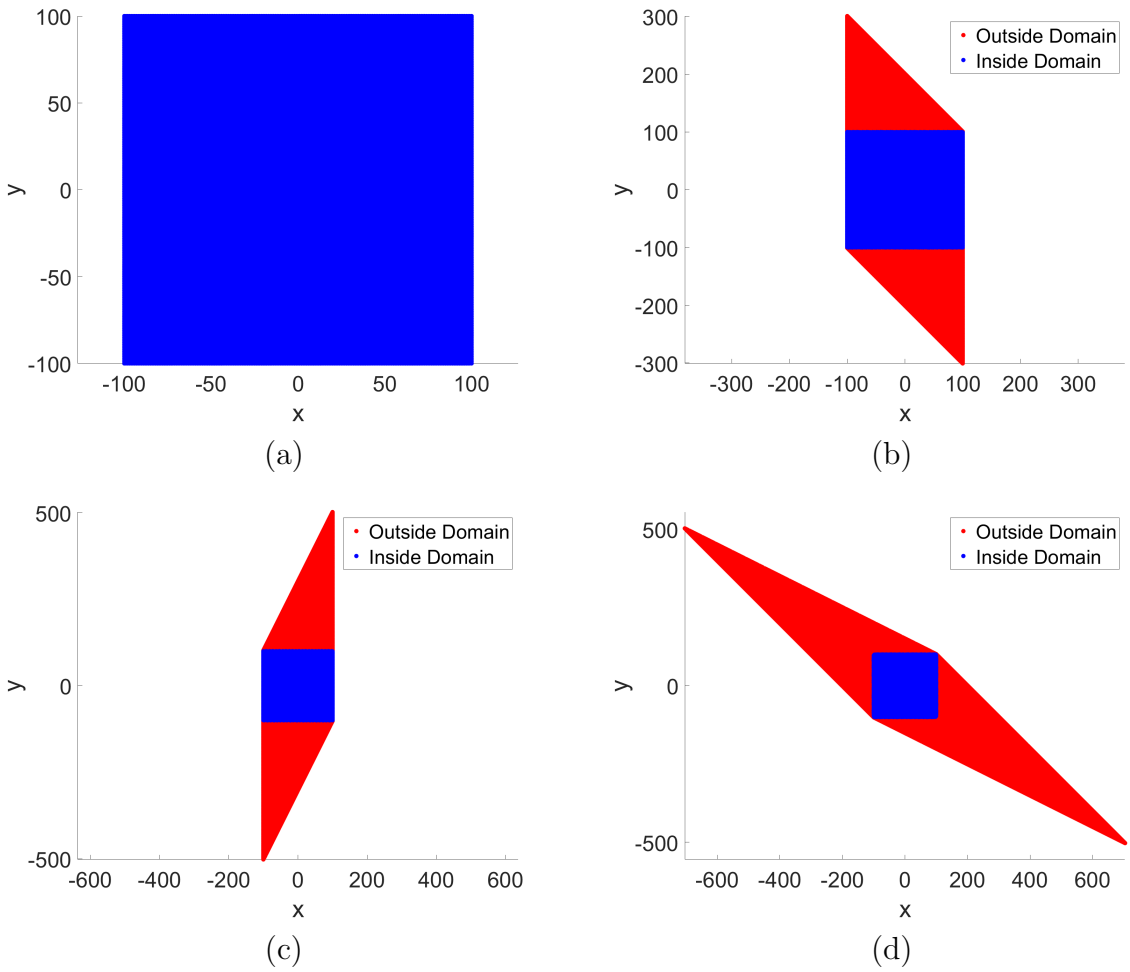

Figure 3.6: Candidate positions for all wavefront combinations using the normal vectors in Table 3.3 for case (a) A (b) B (c) C (d) D.

combinations within the domain, for all other cases there are some combinations which lie outside the domain in question. In all cases the solutions form a parallelogram whose edges are perpendicular to the wavefront normal vectors.

The indices which result in intersections within the domain can be recorded and for cases B, C and D are visualized in Fig. 3.7. Here the blue dots represent wavefront index combinations (i_1, i_2) which result in a candidate intersection within the specified domain, and the red dots are combinations which lie outside the domain. It can be seen that there is a structure along one of the diagonals, the direction of which corresponds to the sign of the normal vector dot products. If the dot products of the normal vectors are positive, the set of solutions which result in candidate positions within the domain will have an overall positive slope, and a negative dot product will result in an overall negative slope. Furthermore the width of

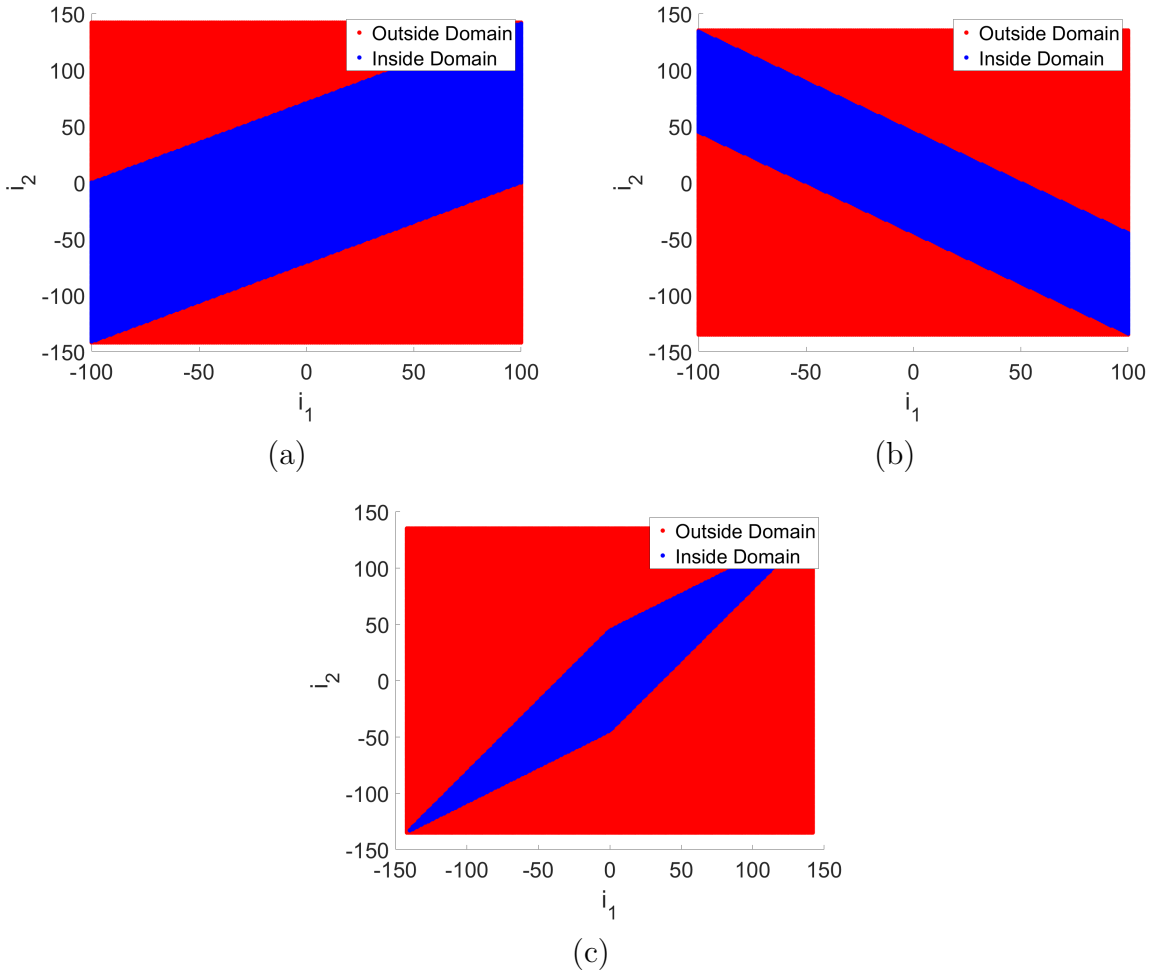

Figure 3.7: Pulsar wavefront index combinations, where the red dots result in candidate positions outside the domain, and the blue dots inside the domain, for pulsars with normal vectors as defined in Table 3.3 for case (a) B (b) C (c) D.

the band is correlated to the dot product of the normal vectors where a larger dot product results in a thinner band.

This can be tested with a more extreme case with pulsar normal vectors which are nearly parallel to one another, case E. The resulting candidate positions and index combinations which result in those positions are shown in Fig. 3.8, where again blue dots are within the domain and red dots are outside of the domain. Figure 3.8(a) shows the resulting set of candidate positions, which result in the most solutions along a thin band extending far outside of the domain, for a clearer image of the area within the domain refer to Fig. 3.8(b). Here it can be seen that there are a few combinations which result in feasible intersections within the domain. The upper and lower bands are only half within the domain as they cross over the domain boundary at 0. Figure 3.8(c) shows the index combinations and whether they result in a candidate inside or outside of the domain. This is a more extreme case than

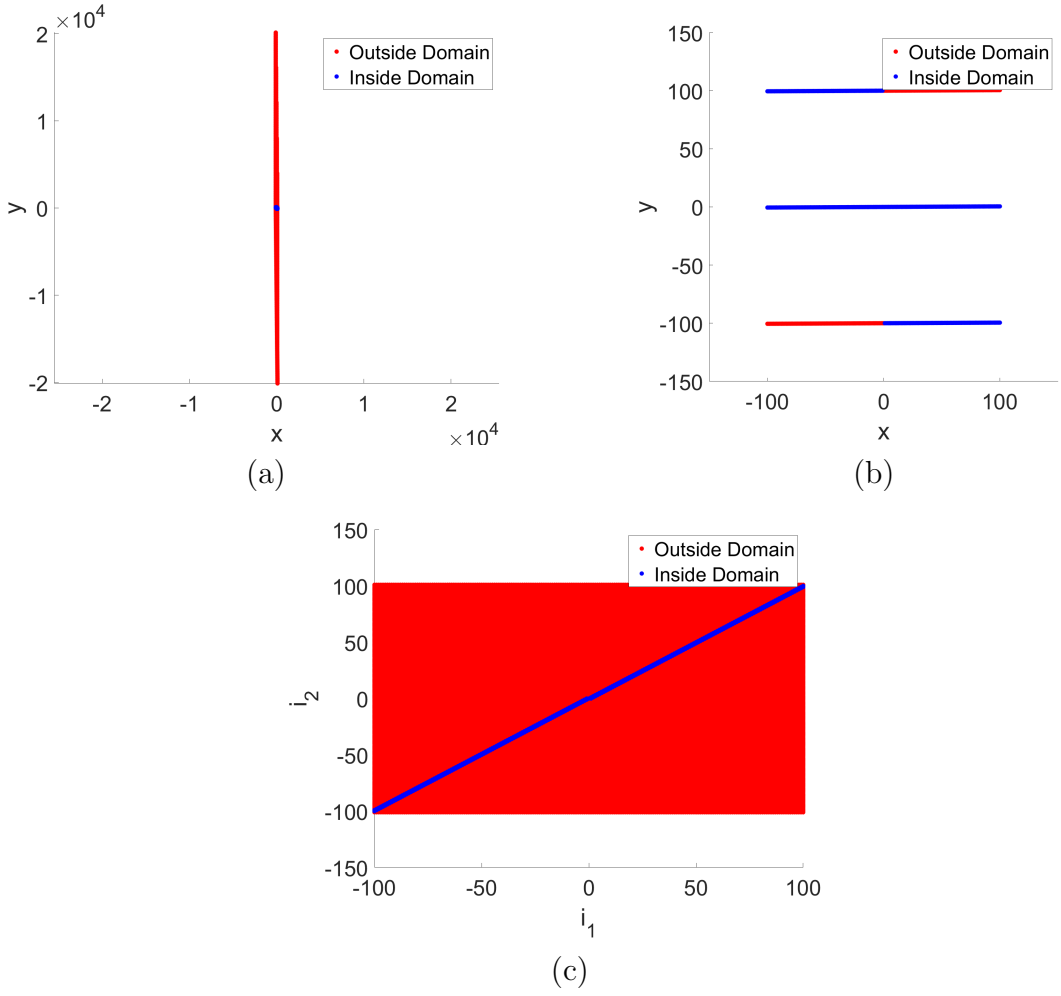

Figure 3.8: For pulsars with normal vectors defined by case E from Table 3.3 (a) the resulting candidate positions (b) candidate positions near the domain.

those in Fig. 3.7 where the parallelogram is very thin and concentrated along the diagonal.

Looking at Fig. 3.7 and Fig. 3.8(c) searching all possible combinations of wavefronts that are within the domain would result in a significant number unnecessary computations. This can be avoided by searching along the banded region using an adaptive algorithm to define which index combinations should be checked (see Algorithm 3). The presented algorithm is for a case where the normal vectors have a positive dot product and consists of three main steps. The first main step is setting $i_1 = 0$, and searching along i_2 both upwards and downwards to find the maximum and minimum i_2 which result in a candidate position within the domain, steps 3-15. Once those values are found the loop is broken as there is no need to continue searching since points outside this range will result in candidate positions outside the domain. Next i_1 is incremented and i_2 is searched from the previous lower boundary upwards. When the value of i_2 no longer results in a candidate position within the domain the loop is broken and a new lower bound on i_2 is defined and i_1 is increased. The process repeats until i_1 reaches it's upper boundary, steps 16-25. This results in finding all points from Fig. 3.8 with an $i_1 \geq 1$ that result in candidate positions within the domain. Steps 26-35 do a similar process but search by decreasing i_1 and searching i_2 from its upper boundary downwards, finding all points with $i_1 \leq -1$ from Fig. 3.8 which would result in candidate positions within the domain. For the case where the normal vectors result in a negative dot product, the inner loops which increment i_2 must be reversed, swapping steps 18-24 with steps 28-34.

Using algorithm 3 to iterate through candidate points results in far fewer computations for the intersection of two pulsars as well as reduces the number of candidate points which would need to be checked for additional pulsar measurements. In case B, there were a total of 57,285 index combinations within the upper and lower boundaries, however only 28,427 resulted in candidate positions within the domain, meaning approximately half needed to be evaluated. For case C, the proportion of combinations which needed to be evaluated was further reduced from 54,471 total combinations to 17,979, and for case D from 77,235 to 12,649. Case E provided the most significant reduction in the number of evaluated from 40,083 total combinations down to 401, less than 1% of the total number of index combinations. Each index combination evaluated requires one matrix inverse calculation, therefore removing half or more of the combinations results in significant reduction in computation time. The order the pulsars appear in Table 3.1 was set such than the maximum number of wavefronts within the domain are increasing from pulsars 1-5, to minimize the computation time for the following sections.

Algorithm 3 Index search for normal vectors with positive dot product

Compute index upper and lower bounds for each pulsar, LB_1, UB_1, LB_2, UB_2
Set $i_1 = 0$, $i_2 = 0$
while $i_2 \leq UB_2$ **do**
    Compute candidate position
    if Candidate position outside of domain **then**
        Define upper bound of i_2, i_U
        Break loop
    $i_2 = i_2 + 1$
$i_2 = -1$
while $i_2 \geq LB_2$ **do**
    Compute candidate position
    if Candidate position outside of domain **then**
        Define lower bound of i_2, i_L
        Break loop
    $i_2 = i_2 - 1$
$i_1 = 1$
while $i_1 \leq UB_1$ **do**
    $i_2 = i_L$
    while $i_2 \leq UB_2$ **do**
        Compute candidate intersection
        if Candidate position outside of domain **then**
            Define lower bound of i_2, i_L
            Break loop
        $i_2 = i_2 + 1$
    $i_1 = i_1 + 1$
$i_1 = -1$
while $i_1 \geq LB_1$ **do**
    $i_2 = i_U$
    while $i_2 \geq LB_2$ **do**
        Compute candidate intersection
        if Candidate position outside of domain **then**
            Define upper bound of i_2, i_U
            Break loop
        $i_2 = i_2 - 1$
    $i_1 = i_1 + 1$
Evaluate additional pulsar measurements

3.3.2 Error Ball Model

To check if the wavefronts from an additional pulsar coincide with a given intersection, Eq. 3.5 must be valid when evaluated at a candidate intersection point. From Eq. 3.5, the coefficient c may be moved to the left hand side and the right hand side may be interpreted as the distance from the new wavefront to the intersection point, as shown in Eq. 3.33. If the right hand side is less than some tolerance, ϵ, the intersection point is a candidate spacecraft position, see Fig. 3.9. The tolerance may be set to represent the phase accuracy of the pulsar waveform measurement.

$$a_p x + b_p y - c_i \leq \epsilon \quad i, p = 3, 4, ... \tag{3.33}$$

If this condition is checked for each candidate point then $\prod_{i=1}^{j} N_i$ computations are required where the N_i correspond to the number of pulsar wavefronts in the search space, and j is the number of pulsars observed. Solving the problem in this manner is inefficient and may be intractable given the limitations of flight computers, especially if the search domain is large. A more efficient method of determining the feasibility of a candidate intersection is to determine the required c_i value for an intersection to exist by solving Eq. 3.5 for a given candidate position. Looking back to Eq. 3.9, it can be seen that this value is related to the period of the pulsar, its phase offset, and an integer index. Equation 3.9 may be solved for the integer index as

$$j = \frac{c_i}{\lambda_p} - \phi_p \tag{3.34}$$

The required c_i and other pulsar properties are substituted into this equation, and if the value of j is integral, then the pulsar wavefront will intersect at this candidate location. Otherwise, there will be no intersection. By performing the computation this way, there are

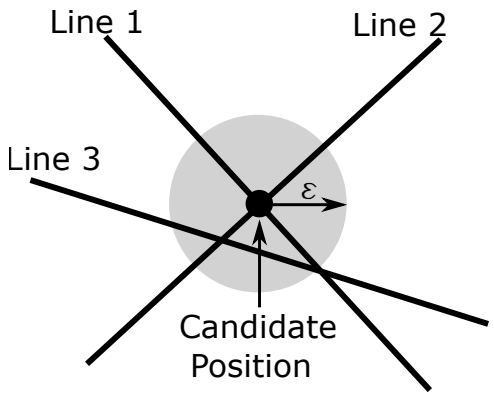

Figure 3.9: Feasible region for the intersection of an additional pulsar.

now only $\prod_{i=1}^{j-1} N_i$ computations which corresponds to the number of candidate locations. If additional pulsars are observed, only the points which pass the previous test are considered, further reducing the computational load.

A few additional assumptions were made to simplify the problem. All measurements are assumed to be measured concurrently to allow for the calculation of their intersections. Based on how the problem has been defined, the intersection of two wavefronts are found first then an error ball is constructed from this point, Fig. 3.9. The size of the error ball is related to the uncertainty in the measurement of an additional pulsar. The error of the first two measurements would correspond to shifting the center of the error ball not increasing the size of the ball. Therefore, the error in the first two pulsar observations is not included. To enforce a solution within the domain no phase offset is given for any of the pulsars resulting in a solution at the origin.

Effecting of Varying Phase Error

Using a phase tolerance of 10^{-3} the intersections of the first three, four, or five pulsars from Table 3.1 may be found as shown in Fig. 3.10. The phase error of 10^{-3} results in a position error on the order of 1 km. This position error results in 114,281 candidate solutions within the space when observing three pulsars, and the solution has a banded structure throughout the domain. Since each of these points is a feasible solution to within 1 km there is no way of accurately determining at which point the observer is located. There are two options to then resolve position: the pulsars may be observed for a larger period of time to reduce the position error and accept fewer candidate positions, or another pulsar may be observed. If an additional pulsar is observed the 114,281 solutions may be reduced to 233 solutions, and if the fifth pulsar is observed three solutions remain. However, it should be noted that, in general, there is no guarantee that a solution exists in a domain of this size. The addition of a small phase offset to a set of wavefrons to the problem may result in no solutions within the domain.

The same procedure may be repeated with other phase tolerances to determine how the candidate solutions change with phase accuracy. If the phase tolerance is adjusted to 10^{-4}, which corresponds to a position error on the order of 100 m, there are 11,439 solutions for three pulsars and a single solution for four or five pulsars, Fig. 3.11. Comparing the 10^{-4} case (Fig. 3.11) to the 10^{-3} case (Fig. 3.10) shows that increasing the phase tolerance by an order of magnitude decreased the number of candidate solutions by an order of magnitude for the intersection of 3 pulsars. For the 3 pulsar case the banded structure is present for both phase tolerances, but as the accuracy is increased the thickness of the band is decreased. Adding

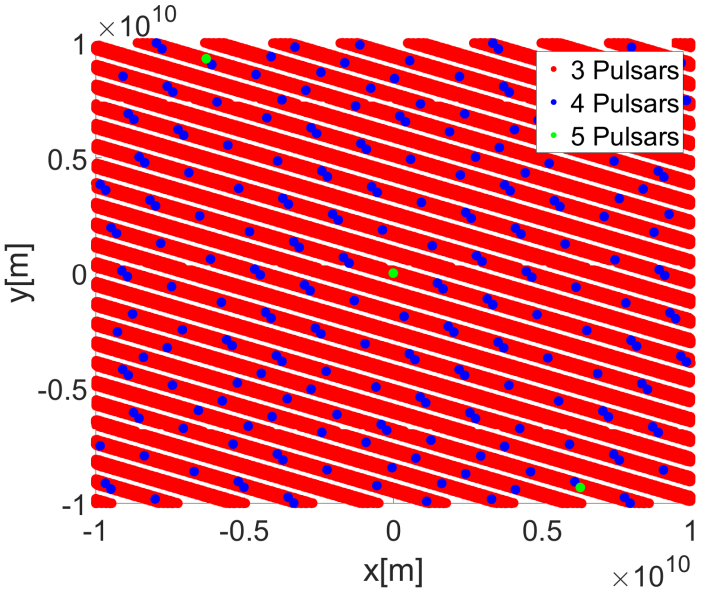

Figure 3.10: Candidate spacecraft positions for 3, 4 and 5 pulsars within a phase tolerance of 10^{-3}.

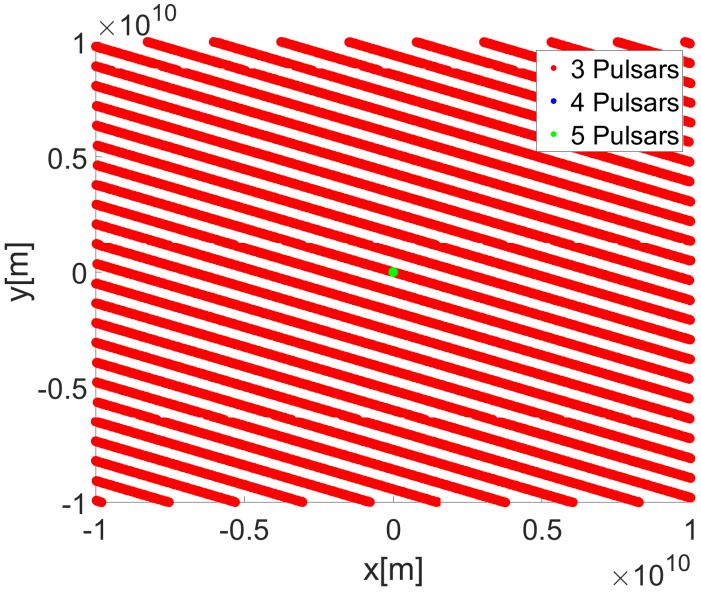

Figure 3.11: Candidate spacecraft positions for 3, 4 and 5 pulsars within a phase tolerance of 10^{-4}. A single candidate position for the 4 pulsar case is found and it lies underneath the candidate position for the 5 pulsar case.

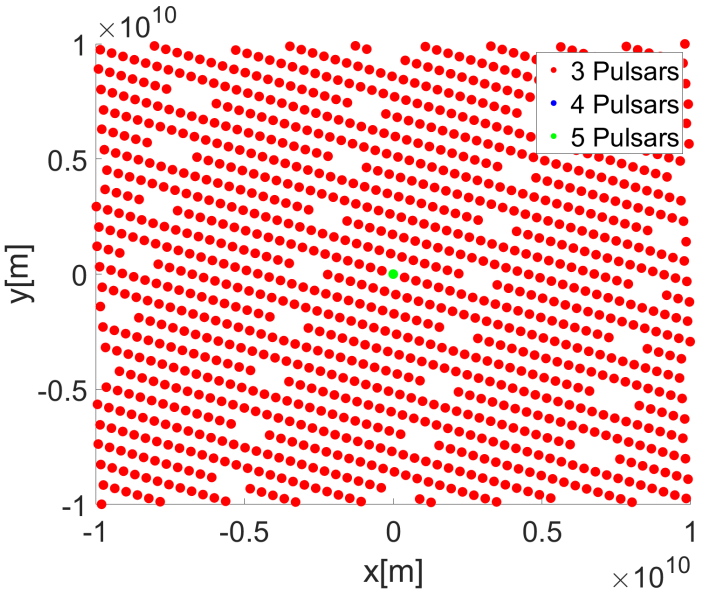

Figure 3.12: Candidate spacecraft positions for 3, 4 and 5 pulsars within a phase tolerance of 10^{-5}. A single candidate position for the 4 pulsar case is found and it lies underneath the candidate position for the 5 pulsar case.

a fourth pulsar with a phase accuracy of 10^{-4} now results in a single solution whereas with a larger phase tolerance it had 233 solutions, a reduction of two orders of magnitude. For the five pulsar cases there is now a single solution at the origin.

A final case may be considered where the pulsar is observed for a phase tolerance of 10^{-5} resulting in a position error on the order of 10 m. In this case there are 1,143 solutions for three pulsars and a single solution for four or five pulsars, Fig. 3.10(a). Again the increase of the phase tolerance by an order of magnitude decreased the number of candidate solutions by an order of magnitude for three pulsars. For four or five pulsars again there is a single solution at the origin. The banded structure of the three pulsar solution is still present but the solutions are more spread out and there are gaps in the structure that were not present before.

There are now two possible methods to obtain the solution at the origin. Either a phase tolerance of 10^{-4} may be used for four pulsars, or a phase tolerance of 10^{-3} may be used with five pulsars. When considering these cases, the time required to perform the computation is nearly identical. Computing the intersections for the first two pulsars directions is obtained by permuting Eq. 3.6 by all possible c_i values within the domain. Using the pulsar properties from Table 3.1 and a domain size of 2×10^{10} m the number of wavefronts within the domain may be found by a dot product of the pulsar direction and the corner of the domain, this results in 14,574 wavefronts in the first direction and 22560 in the second. Evaluating

Eq. 3.6 at each combination of these wavefronts yields 328,789,440 candidate intersections. Evaluating a third pulsar at these candidate locations reduces the number of candidates down to 11,439 for the 10^{-4} case, and 114,281 for the 10^{-3} case, which is negligible compared to the initial number of candidates. For a given domain size, adding additional pulsar measurements results in negligible changes in computation time.

Observation Time Versus Additional Measurements

Equation 2.23 shows the variance in measurement error is related to the observation time by $1/T_{obs}$, which makes the error proportional to $1/\sqrt{T_{obs}}$. Fig. 3.13 shows the number of candidate solutions as a function of observation time for 3, 4 or 5 pulsar measurements, with phase accuracies between 10^{-3} and 10^{-5} and their corresponding required observation time from Table 3.2. For the case of 3 pulsars, as the measurement accuracy is increased by an order of magnitude the number of solutions also drops by an order of magnitude. When considering 4 pulsars, as the measurement accuracy is increased by an order of magnitude the number of solutions drops by two orders of magnitude until there is a single solution. The five pulsar case has three solutions with a phase accuracy of 10^{-3} and otherwise it is a horizontal line with one solution. In order to determine the candidate set with a phase tolerance of 10^{-3}, a total observation time between 4.07×10^5 and 7.56×10^5 s (approximately 1 day) is required depending on the number of pulsars observed. A phase tolerance of 10^{-4}

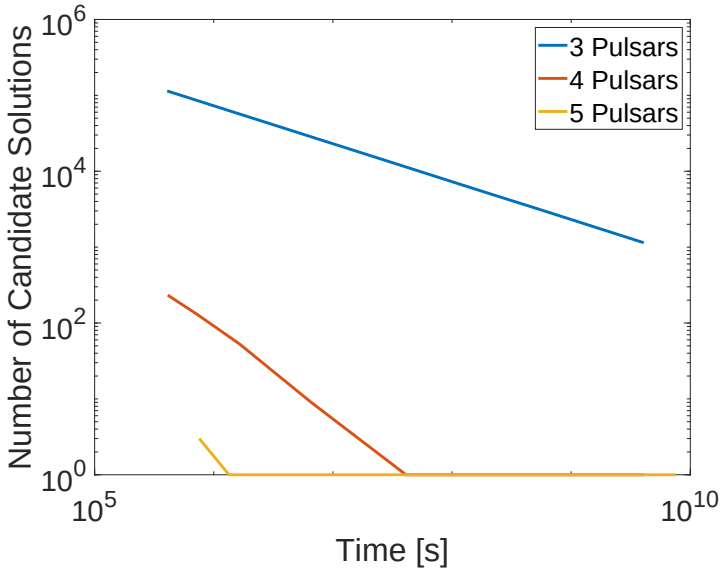

Figure 3.13: Number of candidate solutions as a function of observation time for 3, 4 or 5 pulsar measurements.

requires between 4.07×10^7 and 7.56×10^7 s (approximately 100 days), and a tolerance of 10^{-5} between 4.07×10^9 and 7.56×10^9 s (approximately 10000 days). Measuring five pulsars at a phase tolerance of 10^{-3} takes over 3 orders of magnitude less observation time than the required observation time for even one measurement at a phase tolerance of 10^{-5}. Therefore, when trying to minimize the number of candidate solutions in a given domain, it may be more beneficial to observe additional pulsars for shorter durations rather than increase the observation time for each pulsar.

Non-zero Phase Offset

In a real scenario, it is unlikely that the phase offset of each pulsar will all be zero; therefore, the phase of each pulsar will be allowed to vary as time is shifted forward by 10 s. This results in different phase offsets for each pulsar and the resulting intersections are computed and can be seen in in Fig. 3.14. For this case, if a small phase offset is added the same type of banded structure is retained; however, the bands are shifted. Looking back, the intersections are calculated by solving the equation of each line simultaneously and finding a position that satisfies all of them, Eq. 3.6. The c values are defined in Eq. 3.9, where ϕ is the phase offset. As time moves forward the phase offset changes linearly for each pulsar, and the combination of linear transformations will always be a linear transformation. As a result, changing the phase offset only linearly shifts the candidate solutions as a whole, it does not

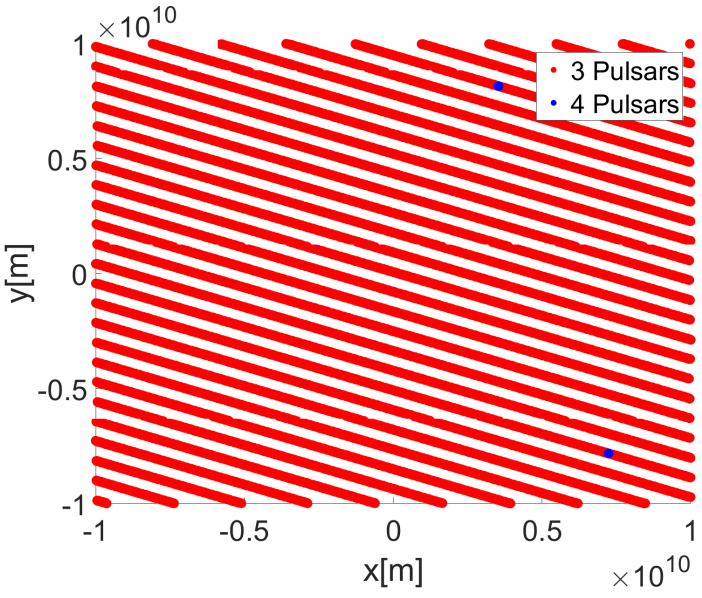

Figure 3.14: Candidate spacecraft positions for 3 and 4 pulsars within a phase tolerance of 10^{-4} with t=10 s.

change the orientation of the solutions. This implies that the number of solutions and how they are oriented within a domain only need to be calculated once for each combination of pulsars and phase accuracies. To asses the number of candidate solutions and their relative orientation, setting the phase offset to zero0 is sufficient and will be used for all following analysis.

Observation Order

As previously mentioned, the intersection of the first two pulsar wavefronts is computed and this intersection point serves as the center of the error ball, which implies that error in the first two measurements is not being accurately represented. Since the error ball is constructed

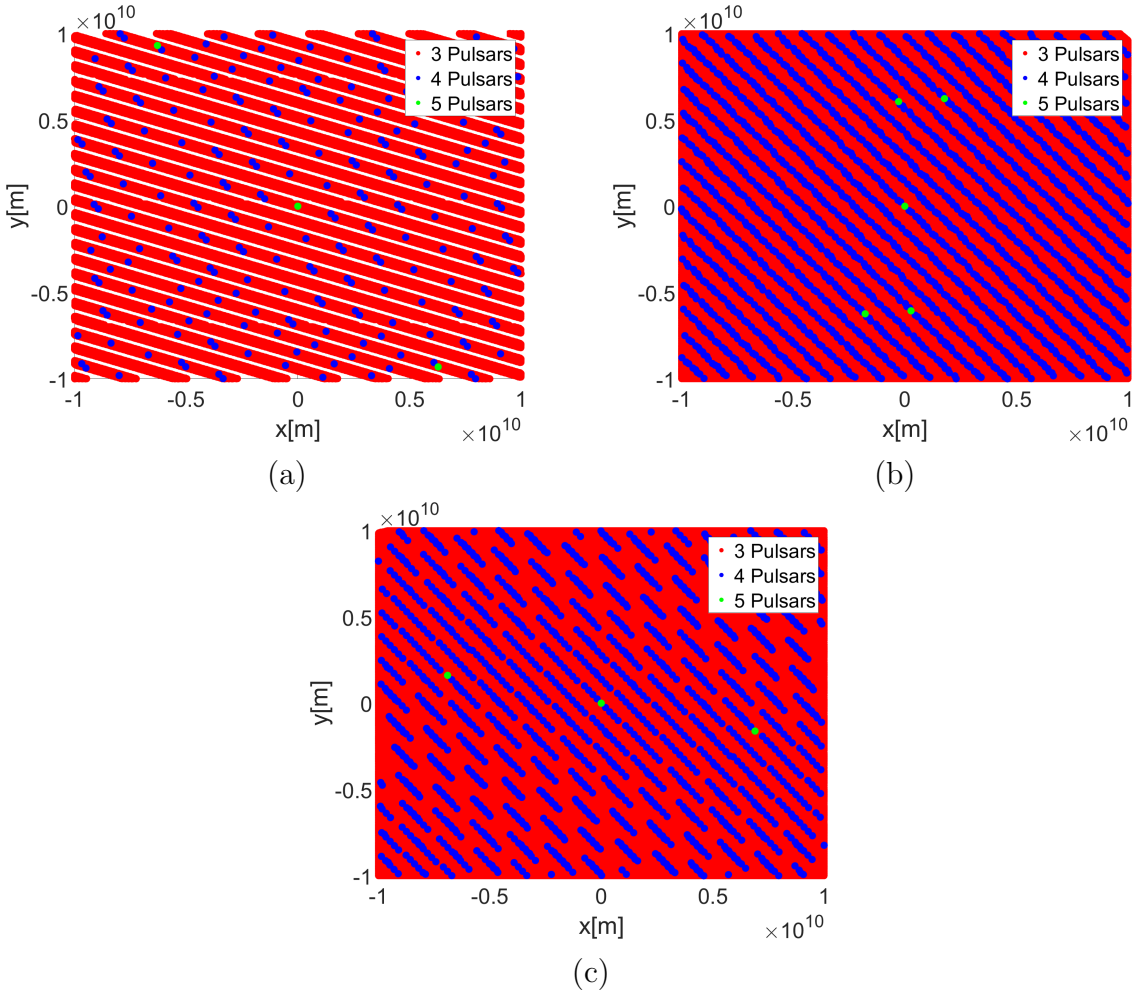

Figure 3.15: Candidate solutions for 3,4 and 5 pulsar observations with a phase tolerance of 10^{-3} where the order is defined by (a) the order in Table 3.1 (b) measurements 1 and 3 are switched (c) measurements 2 and 3 are switched.

in this way the order the measurements are considered matters since a different order would shift the location of the error ball center. The order of the first three pulsar observation is permuted to and the resulting intersections are computed and shown in Fig. 3.15. By varying the order that the pulsar observations are considered the structure of the 4 and 5 pulsar solutions are different. The original case, Fig. 3.15(a) presents the most sparse set of candidate solutions, the case where the first and third observations are flipped, Fig. 3.15(b) has the most solutions and the case where the second and third observations are flipped, Fig. 3.15(c), is an intermediate case. In cases (b) and (c) a clearer banded solution structure for the four pulsar case can now be seen whereas in case (a) it is more uniformly distributed. Aside from the solution at the origin, observing all five pulsars results in different candidate positions for all three cases. The order of observation impacts the number of candidate solutions as well as their relative position.

3.3.3 Banded Error Model

The error ball model may provide a quick estimate of candidate solutions, however it does not consistently identify all potential solutions. More realistically, measurement error typically results in some uncertainty in the position of wavefronts, which can be modeled as a band about each wavefront (see Fig. 3.16). By modeling the error as a banded region, the model is able to account for each pulsar's error characteristics independently by adjusting the width of the band. Intersecting two banded regions creates a parallelogram which will define the feasible intersection region. The error band for any additional pulsar measurement must overlap part of this feasible region. Only the portion of the region which intersects all of the banded errors will be considered a feasible solution. There are three scenarios which result in an overlap of banded regions as shown in Fig. 3.17. In cases (a) and (b) the pulsar wavefront passes within the feasible region, however in case (b) the feasible region is entirely within the banded region of the third pulsar resulting in no reduction of the feasible region. In case (c) the pulsar wavefront lies outside of the feasible region, but the error band overlaps the feasible region.

Calculating the feasible region for the banded error model starts by finding the intersection of two wavefronts and computing the vertices of the overlapping banded regions. The vertices are found by solving Eq. 3.6 four times where the c_i values are permuted by $\pm\epsilon_i\lambda_i$:

$$\begin{bmatrix} a_1 & b_1 \\ a_2 & b_2 \end{bmatrix} \begin{bmatrix} x \\ y \end{bmatrix} = \begin{bmatrix} c_1 \pm \epsilon_1\lambda_1 \\ c_2 \pm \epsilon_2\lambda_2 \end{bmatrix} \tag{3.35}$$

At each vertex, the required wavefront number for the additional measurement to coincide

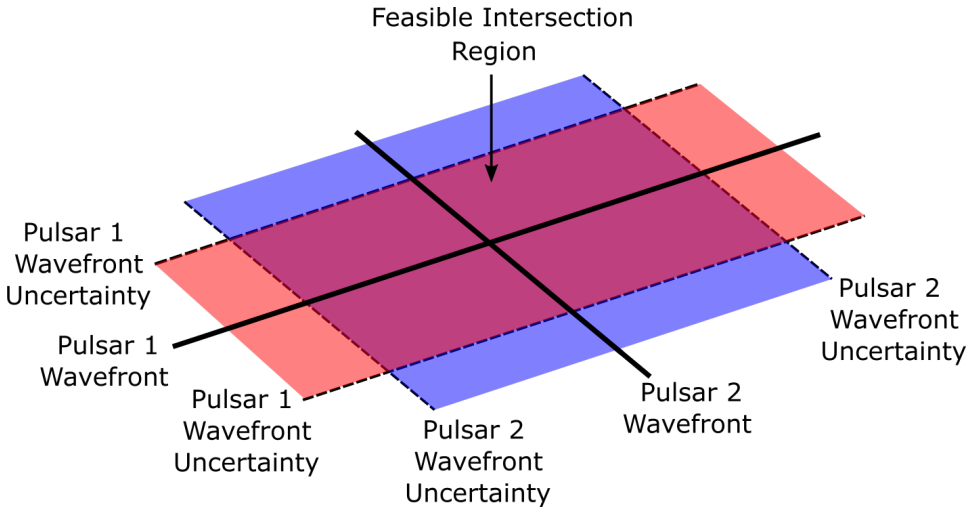

Figure 3.16: Feasible search region for the intersection of 2 pulsars.

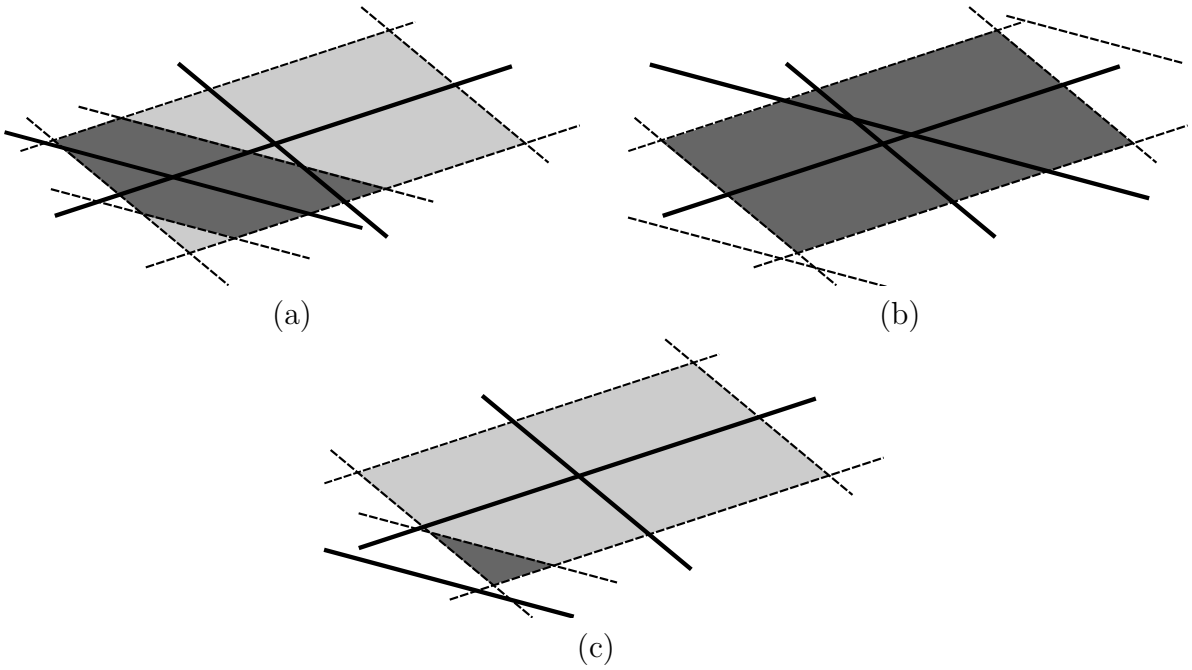

Figure 3.17: The intersection may be feasible if (a) the new wavefront and error bands lie within the feasible region (b) the error band covers the entire feasible region (c) the wavefront is outside of the feasible region, but the error band overlaps the feasible region.

with that vertex is computed. The constant c is defined for a general line by Eq. 3.4, where in this case the x_0 and y_0 are the vertex of the parallelogram. This calculated value of c may be substituted into Eq. 3.9, and rearranged to solve for the index, j, as in Eq. 3.34.

$$j = \frac{c_i}{\lambda_i} - \phi_i \tag{3.36}$$

In this case the value of i does not need to be integral, rather if the integer part of i changes between any of the vertices then the third wavefront passes through the polygon, as in cases (a) and (b). To check for case (c) a tolerance of ϵ is added to the maximum i and subtracted from the minimum i. If there is no solution for the additional pulsar measurement the computed i value will have the same integer part for all vertices and this candidate location will be discarded as an infeasible solution. The condition in Eq. 3.37 determines if the feasible solution region overlaps with the banded region of an additional pulsar measurement.

$$\text{if } \exists\, j \in \mathbb{Z} \text{ where } \min(i - \epsilon_p) \leq j \leq max(i + \epsilon_p) \tag{3.37}$$

The above condition only determines if the banded regions overlap, it does not determine the new shape of the feasible region. Each vertex of the original parallelogram must be evaluated to see if it lies within the banded region by evaluating if the i value of the vertex is within the tolerance ϵ of the j index.

$$j - \epsilon_p \leq i \leq j + \epsilon_p \tag{3.38}$$

The vertices which do not satisfy this condition lie outside the new feasible region and are removed. When comparing the $i \pm \epsilon$ and j, if all i values are above the $j - \epsilon$ or below the $j + \epsilon$ value, then the corresponding boundary of the banded region lies outside of the previous feasible region. This occurs in case (b) and on the lower boundary of the banded region in case (c). As seen in cases (a) and (c) there may be additional vertices of the new feasible region which must be calculated.

Consider case (a) where there are three vertices which would lie outside of the overlapping banded regions and additional vertices would need to be found. For simplicity, the vertices will be labeled as in Fig. 3.18. Vertices A, B, C, D are found previously from the intersection of the first two pulsar banded regions by using Eq. 3.35. When using these vertices, the condition in Eq. 3.34 would fail for vertices B, C and D, while vertex A is passed into the new parallelogram. Aside from the vertices A, B, C, D there are additional intersections labeled E, F, G, H, P, Q, R, S which are the intersections of the boundary of banded region of the new measurement with all other boundaries in the space. To determine which vertices

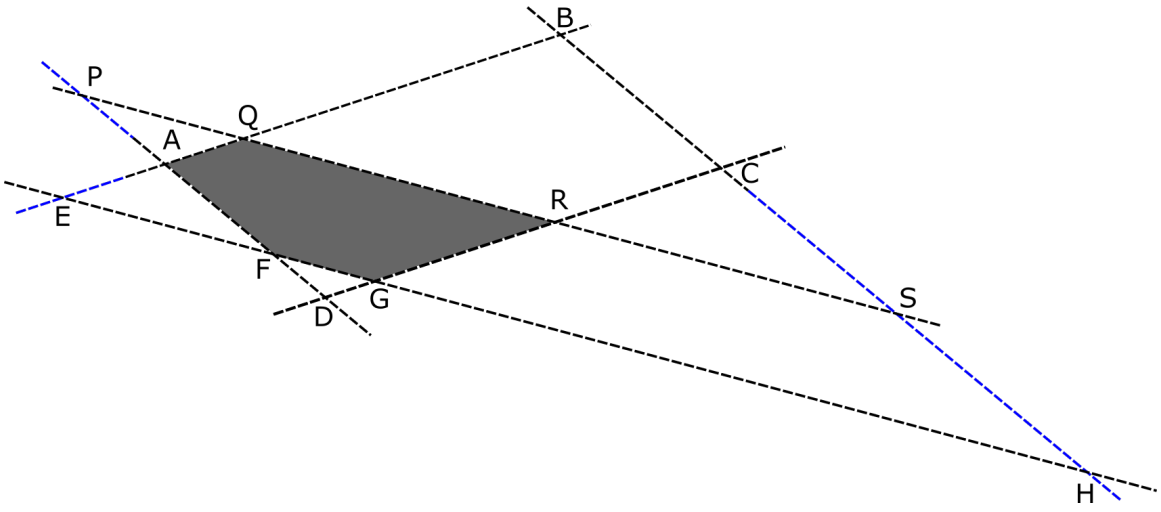

Figure 3.18: All intersections of the boundaries of banded wavefronts.

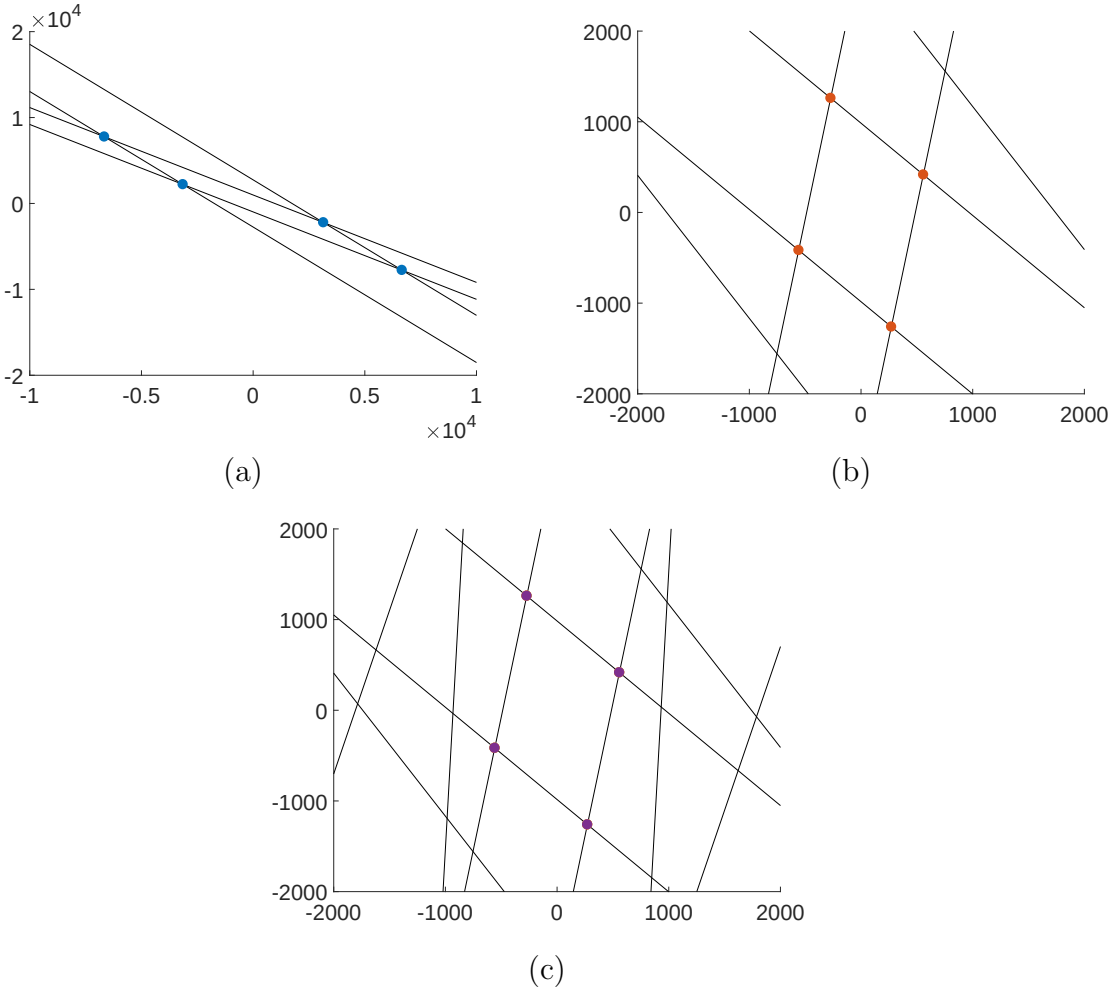

Figure 3.19: Selected vertices for intersection of (a) 2 wavefronts (b) 3 wavefronts or (c) 5 wavefronts.

construct the feasible region the indices are split into two sets, one for each boundary. Then the sets are sorted in ascending or descending order along the boundary, creating sets E, F, G, H and P, Q, R, S. The two innermost vertices are selected to construct the feasible region. For the set E, F, G, H vertices F and G are output and for the set P, Q, R, S vertices Q, and R are output. The set of vertices A, F, G, Q, R are used to construct the feasible region from Fig. 3.17(a). If additional pulsar observations are used, the same procedure is repeated for each subsequent measurement. If N is the number of pulsar observations, there will be $2(N-1)$ intersections, and again the middle two vertices are output.

An example set of data is shown in Fig. 3.19, for the 5 pulsars described in Table 3.1 with a phase tolerance of 10^{-3}. No phase offset was used, so an exact solution occurs at the origin. In this case, after the third pulsar observation, the other wavefront banded regions overlap the entire feasible region so no changes to the vertices are observed.

3.3.4 Effect of Varying Phase Error and the Number of Pulsars Observed

Using a phase tolerance of 10^{-3} the intersections of the first three, four, or five pulsars from Table 3.1 may be found as shown in Fig. 3.20. The phase error of 10^{-3} results in a position error on the order of 1 km. This position error results in 2,016,493 candidate solutions within the space when observing three pulsars. Since each of these points is a feasible solution to within 1 km there is no way of accurately determining at which point the observer is located. There are two options to then resolve position: the pulsars may be observed for a larger period

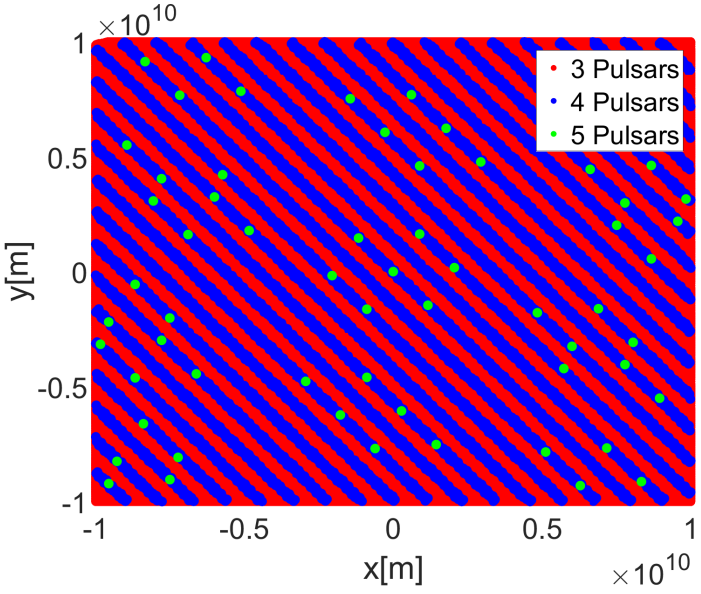

Figure 3.20: Feasible solutions with a phase tolerance of 10^{-3} for 3, 4 and 5 pulsars observed.

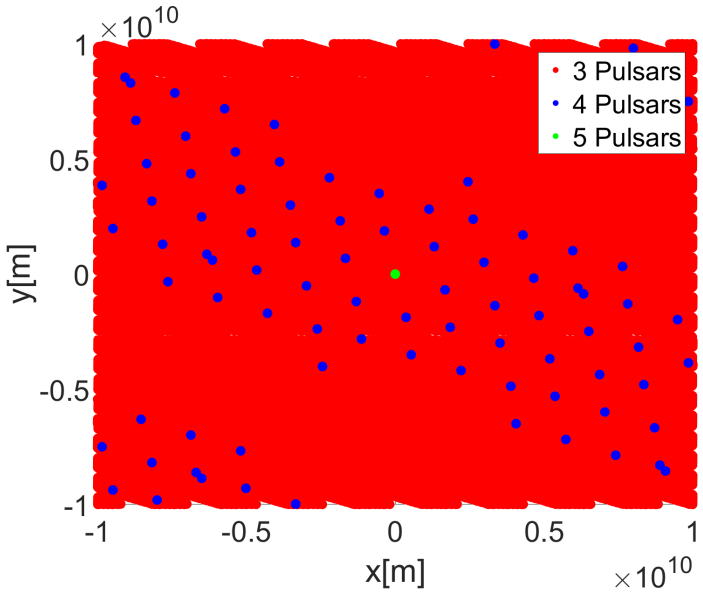

Figure 3.21: Feasible solutions with a phase tolerance of 10^{-4} for 3, 4 and 5 pulsars observed.

of time to reduce the position error and accept fewer candidate positions, or another pulsar may be observed. If an additional pulsar is observed the 2,016,493 solutions may be reduced to 10,103 solutions, and if the fifth pulsar is observed 65 solutions remain. As the number of measurements are increased the number of solutions in the domain is reduced by two orders of magnitude. For 4 pulsars there are bands of feasible solutions and for 5 pulsars there are clusters of solutions. However, it should be noted that, in general, there is no guarantee that a solution exists in a domain of this size. The addition of a small phase offset to a set of wavefronts to the problem may result in no solutions within the domain.

The same procedure may be repeated with other phase tolerances to determine how the candidate solutions change with phase accuracy. If the phase tolerance is adjusted to 10^{-4}, which corresponds to a position error on the order of 100 m, there are 201,615 solutions for three pulsars, and 95 for four pulsars and a single solution for five pulsars, Fig. 3.21. Comparing the 10^{-4} case (Fig. 3.21) to the 10^{-3} case (Fig. 3.20) shows that increasing the phase tolerance by an order of magnitude decreased the number of candidate solutions by an order of magnitude for the intersection of 3 pulsars and two orders of magnitude for the intersection of 4 pulsars. For the 3 pulsar case, majority of the domain is covered in solutions, however some gaps are now visible. Adding a fourth pulsar with a phase accuracy of 10^{-4} results in a banded structure again, however the bands are now in a different direction. Furthermore for 4 pulsars increasing the phase accuracy by an order of magnitude has decreased the number of candidate solutions by more that two orders of magnitude compared the the 10^{-3} case. For the five pulsar cases there is now a single solution at the

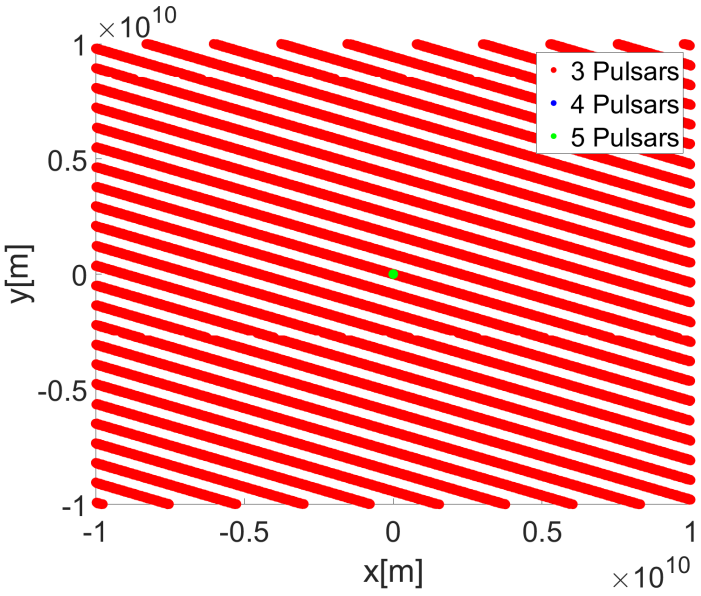

Figure 3.22: Feasible solutions with a phase tolerance of 10^{-5} for 3, 4 and 5 pulsars observed.

origin.

A final case is considered where the pulsar is observed for a phase tolerance of 10^{-5} resulting in a position error on the order of 10 m. In this case there are 20,161 solutions for three pulsars and a single solution for four or five pulsars, Fig. 3.22. Again the increase of the phase tolerance by an order of magnitude decreased the number of candidate solutions by an order of magnitude for three pulsars. For four or five pulsars there is a single solution at the origin. The banded structure is now present for the three pulsar solution and is in the same direction as the four pulsar case with a phase accuracy of 10^{-4}, however the gaps between the bands resemble that of the 4 pulsar case with a phase accuracy of 10^{-3}.

There are now two possible methods to obtain the solution at the origin. Either a phase tolerance of 10^{-4} may be used for five pulsars, or a phase tolerance of 10^{-5} may be used with four or five pulsars. When considering these cases, the time required to perform the computation is nearly identical. Computing the intersections for the first two pulsars directions is obtained by permuting Eq. 3.6 by all possible c_i values within the domain. Using the pulsar properties from Table 3.1 and a domain size of 2×10^{10} m the number of wavefronts within the domain may be found by a dot product of the pulsar direction and the corner of the domain, this results in 14,574 wavefronts in the first direction and 22,560 in the second. Evaluating Eq. 3.6 at each combination of these wavefronts yields 328,789,440 candidate intersections. Evaluating a third pulsar at these candidate locations reduces the number of candidates down to 201,615 for the 10^{-4} case, and 20,161 for the 10^{-5} case, which is negligible compared to the initial number of candidates. For a given domain size, adding

additional pulsar measurements results in negligible changes in computation time.

3.3.5 Observation Time Versus Additional Measurements

Just as in the error ball case the number of solutions may be found as a function of total observation time and the number of pulsar measurements. Figure 3.23 shows the number of candidate solutions as a function of observation time for 3, 4 or 5 pulsar measurements, with phase accuracies between 10^{-3} and 10^{-5}. For the case of 3 pulsars, as the measurement accuracy is increased by an order of magnitude the number of solutions also drops by an order of magnitude. For 4 pulsars the rate at which solutions is reduced is increased to two order of magnitude per order of magnitude increase in accuracy, and for 5 pulsars it is further increased to three orders of magnitude per order of magnitude increase in accuracy. In order to determine the number of feasible solutions with a phase tolerance of 10^{-3}, a total observation time between 4.07×10^5 and 7.56×10^5 s is required depending on the number of pulsars observed. A phase tolerance of 10^{-4} requires between 4.07×10^7 and 7.56×10^7 s, and a tolerance of 10^{-5} between 4.07×10^9 and 7.56×10^9 s. Again, measuring five pulsars at a phase tolerance of 10^{-3} takes over 3 orders of magnitude less observation time than the required observation time for even one measurement at a phase tolerance of 10^{-5}. As in the error ball case, it may be more beneficial to observe additional pulsars for shorter durations rather than increase the observation time for each pulsar.

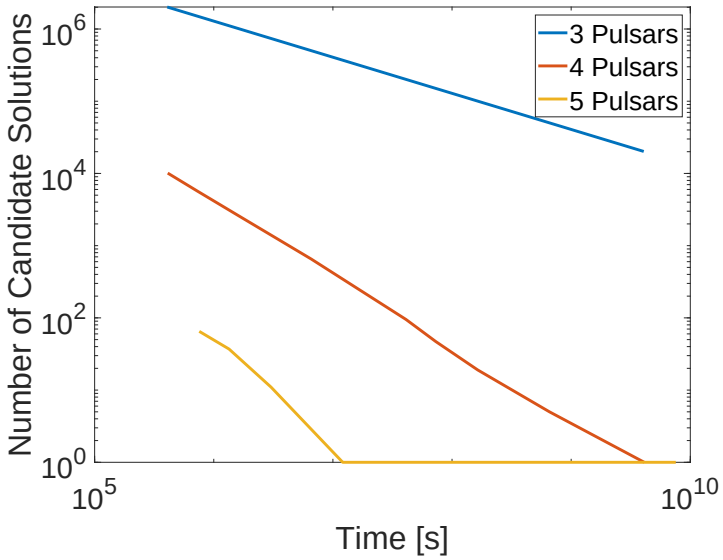

Figure 3.23: Number of candidate solutions as a function of observation time for 3, 4 or 5 pulsar measurements.

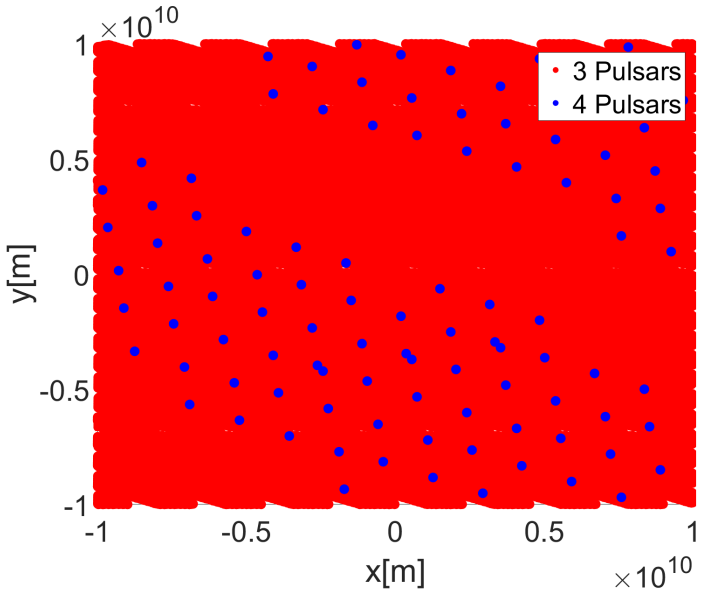

Figure 3.24: Candidate spacecraft positions for 3 and 4 pulsars within a phase tolerance of 10^{-4} with t=10 s.

3.3.6 Non-zero Phase Offset

In a real scenario, it is unlikely that the phase offset of each pulsar will all be zero; therefore, the phase of each pulsar will be allowed to vary as time is shifted forward by 10 s. This results in different phase offsets for each pulsar and the resulting intersections are computed and can be seen in in Fig. 3.24. For this case, if a small phase offset is added the same type of banded structure is retained; however, the bands are shifted. Looking back, the c values are defined in Eq. 3.9, where ϕ is the phase offset. As time moves forward the phase offset changes linearly for each pulsar, and the combination of linear transformations will always be a linear transformation. As a result, changing the phase offset only linearly shifts the candidate solutions as a whole, it does not change the orientation of the solutions. This implies that the number of solutions and how they are oriented within a domain only need to be calculated once for each combination of pulsars and phase accuracies. To assess the number of candidate solutions and their relative orientation, setting the phase offset to zero is sufficient and will be used for all following analysis.

Area of Intersection

One metric which was considered as a means to reduce the number of candidate solutions without the need for additional measurements was to only consider points with large feasible regions. It was thought that candidates with a large feasible region would be more likely to

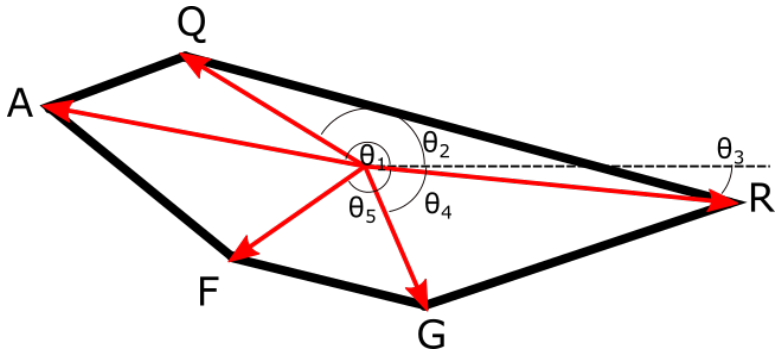

Figure 3.25: Definition of the angle between each measurement.

contain the true solution. The area of each feasible region may be calculated by Gauss's area formula, Eq. 3.39, where the x_i and y_i are the coordinates of each vertex. This formula works for the banded error model since the polygon will always be a convex closed polygon. In order to apply Gauss's area formula the vertices must be written in order along the edge of the polygon. The procedure described above calculates the location of each vertex, however they are not sorted in the correct order. To sort the vertices an interior point to the region must be found, and since the polygon is convex, averaging each vertex will result in an interior point. A vector can then be constructed from this point to each vertex of the polygon. The angle that vector makes with respect to the x axis is found by an inverse tangent, and all vertices are then sorted by their corresponding angle, Fig. 3.25.

$$A = \frac{1}{2}\sum_{i=0}^{n-1} x_i y_{i+1} - x_{i+1} y_i \tag{3.39}$$

Under this condition, the area of the feasible regions was computed for the case with a phase tolerance of 10^{-4} using 4 pulsars, and the results are presented in Fig. 3.26. It can be seen that there is a significant difference in the area among all of the solutions; however, there are still many candidates with similar area to the true solution at the origin. Many of these candidates have similar areas as that of the solution at the origin. It may be possible to reduce the number of solutions in the domain using the area of the intersection region, however this does not present a unique solution and additional pulsar observations would still be required. Thus, using the area to reduce the set of candidate solutions is not recommended.

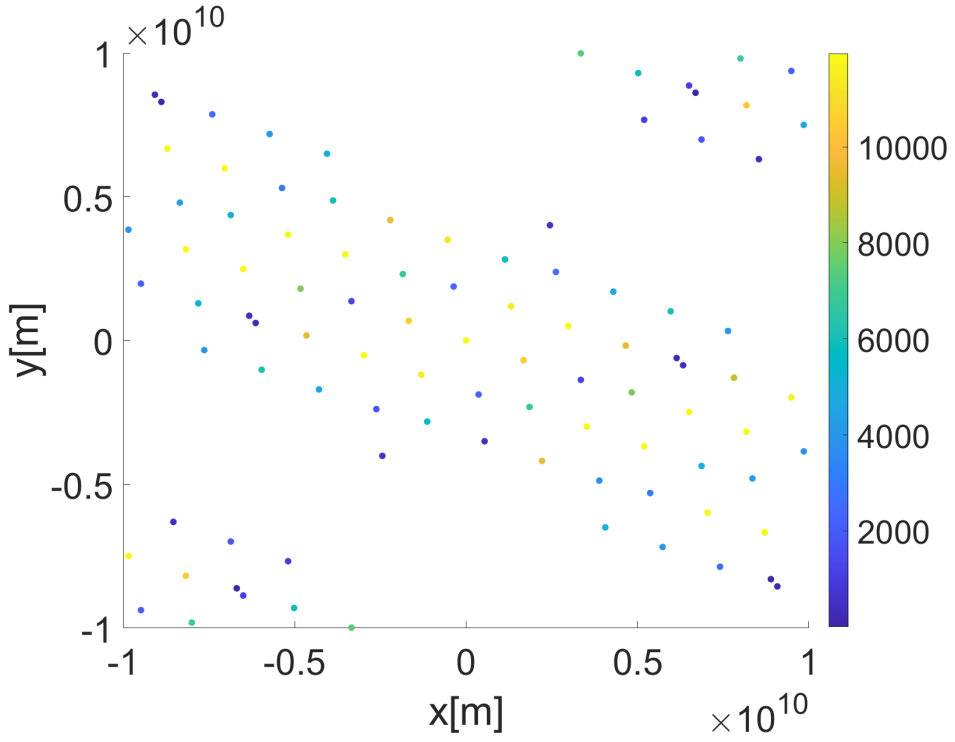

Figure 3.26: Area of the feasible region for the intersection of 4 pulsars.

Geometric Centroid Calculation

If a single solution can be found there is still some uncertainty in the spacecraft position, since anywhere within the polygon is feasible. One candidate for the spacecraft location is the centroid of the feasible region. Since the polygon is convex and closed the coordinates of the centroid, (C_x, C_y), may be computed similarly to the area of the feasible region. Using the area of the polygon, A, and the vertices ordered along the polygons edge from the area calculation, the following equations define the centroid.

$$C_x = \frac{1}{6A}\sum_{i=0}^{n-1}(x_i + x_{i+1})(x_i y_{i+1} - x_{i+1} y_i) \tag{3.40}$$

$$C_Y = \frac{1}{6A}\sum_{i=0}^{n-1}(y_i + y_{i+1})(x_i y_{i+1} - x_{i+1} y_i) \tag{3.41}$$

3.4 Extension to Three Dimensions

Determining the candidate states for XNAV may still solved in 3D using much of the same framework as 2D. Instead of solving the equation of a line as in Eq. 3.3, each pulsar is

represented by a plane given by,

$$ax + by + cz = d \tag{3.42}$$

The constant d characterizes the plane and is given by a point on the plane,

$$d = ax_0 + by_0 + cz_0 \tag{3.43}$$

In the same fashion as 2D the constant defining the plane, d, is defined by the pulsar wavelength and phase offset, and the coefficients a, b and c are defined by the normal vector. The plane defining a pulsar wavefront may then be written as

$$a_p x + b_p y + c_p z = d_i = \lambda_p (i + \phi_p) \tag{3.44}$$

$$\mathbf{n} = \begin{bmatrix} a_p \\ b_p \\ c_p \end{bmatrix} \tag{3.45}$$

The intersection of three planes is a simple linear system given by Eq. 3.46 which may be solved through a matrix inverse. Again, each additional pulsar measurement adds an additional equation, but also adds an unknown in the wavefront index number, i. Solving for the candidate positions in 3D is again an under-constrained problem however now there are $N + 3$ unknowns with N equations.

$$\begin{bmatrix} a_1 & b_1 & c_1 \\ a_2 & b_2 & c_2 \\ a_3 & b_3 & c_3 \end{bmatrix} \begin{bmatrix} x \\ y \\ z \end{bmatrix} = \begin{bmatrix} d_1 \\ d_2 \\ d_3 \end{bmatrix} \tag{3.46}$$

3.4.1 Error Ball Model

Solving the intersection of planes using the error ball method works similarly in 3D as in 2D. The intersection of three planes is calculated using Eq. 3.46. As was the case in 2D, instead of evaluating each plane to see if one of them is near the intersection point to within some tolerance, the required wavefront number, j, is found. Again if j is integral to within some tolerance, ϵ then a solution exists.

$$j = \frac{d_i}{\lambda_p} - \phi_p \tag{3.47}$$

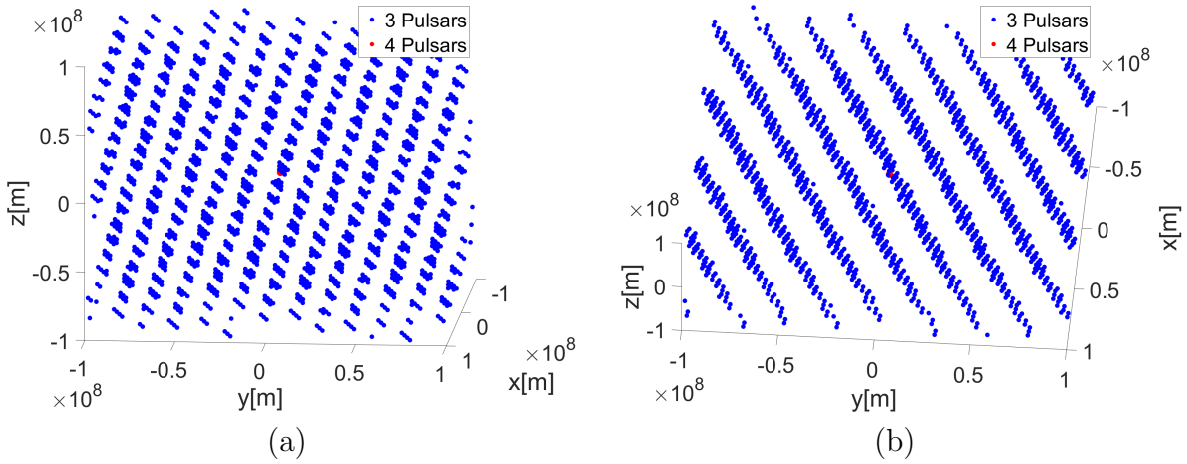

Figure 3.27: Candidate positions for 4 and 5 pulsars in 3D using different views.

Using this condition and the set of equations defined above the intersection for pulsars in 3D may be calculated, and are shown in Fig. 3.27. Here the phase tolerance used is 10^{-4}. Due to the increase in dimension the domain boundary was reduced to a cube with a side length of 2×10^8 m. Using 4 pulsars results in 361 candidate intersections, with a fifth pulsar measurement revealing the true solution at the origin. The 3D candidate positions behave similarly to the 2D candidates in that it follows a periodic structure; however, in the 3D case the solution is periodic in multiple directions.

3.4.2 Banded Error Model

The error ball method has a direct translation to 3D by changing the equation from a line to a plane and adding an additional measurement. In order to solve the banded error model in 3D additional steps are required. The problem begins by converting the base equations from those of lines to planes. Each plane is then offset in each direction by some tolerance ϵ which defines a banded region where feasible intersections may occur. Overlapping two banded region reduces the feasible region further and each additional measurement afterwards reduces it down even more. Figure 3.28 shows an example banded region for 3 pulsar measurements.

The polyhedron defining the feasible region for a solution to exist will be given by its vertices. In order to have a closed polyhedron three pulsar measurements are required. These vertices may be found by solving the following equation

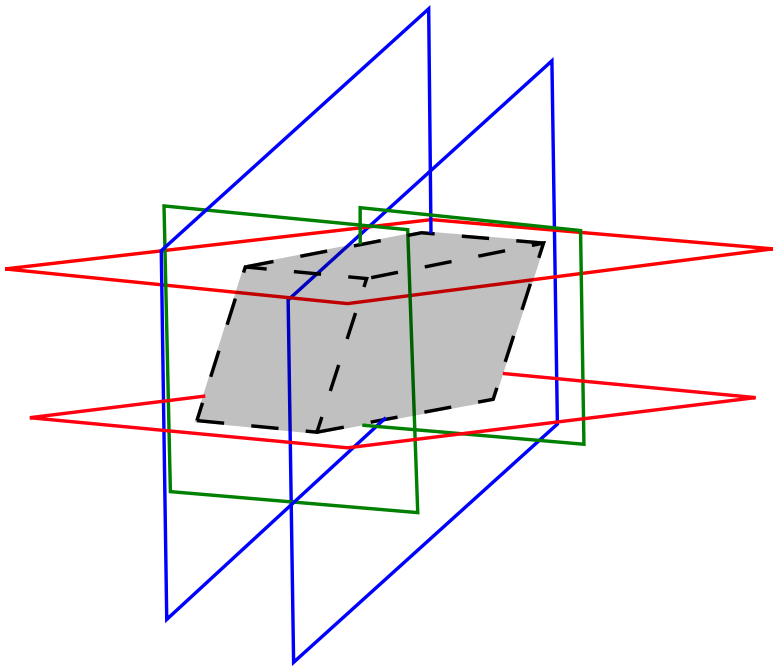

Figure 3.28: Intersection of banded regions in 3D.

$$\begin{bmatrix} a_1 & b_1 & c_1 \\ a_2 & b_2 & c_2 \\ a_3 & b_3 & c_3 \end{bmatrix} \begin{bmatrix} x \\ y \\ z \end{bmatrix} = \begin{bmatrix} d_1 \pm \lambda_1 \epsilon_1 \\ d_2 \pm \lambda_2 \epsilon_2 \\ d_3 \pm \lambda_3 \epsilon_3 \end{bmatrix} \tag{3.48}$$

The 8 combinations result in the 8 vertices of the parallelepiped defined by the intersection of the three banded regions. When considering additional measurements, the condition which determines if this vertex is within the new polyhedron or not is the same as it was in 2D, Eq. 3.37. If this condition is not satisfied, the vertex is removed. The removal of any of the vertices implies that the polyhedron has changed shape and additional vertices are created. These vertices are found by solving a 2D problem on the plane of the additional measurement, where the lines are computed by finding the intersection of each boundary plane.

The problem may be written in the same form as the 2D banded error model presented above by rotating the plane such that its normal vector points along the z-axis. This can be done by an axis-angle rotation, where the axis is defined by the cross product of the normal vector with the z-axis and the angle is the dot product of the normal vector and the z-axis. Upon completing this rotation all of the points would be have a non-zero z offset which can be removed to make the problem identical to the 2D version. Once the resulting polygon is found, the z offset must be added to each vertex then the resulting coordinates can be rotated back into the original frame. These vertices create one face of the polyhedron for the 3D problem. This procedure may then be repeated for any number of pulsar measurements.

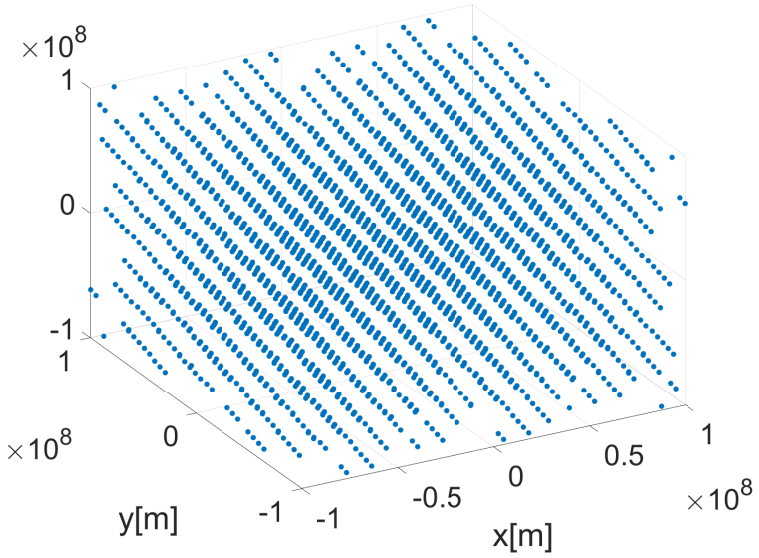

Figure 3.29: Candidate positions using a banded error model in 3D.

Using the above procedure the candidate solutions can be found, as seen in Fig. 3.29. The phase tolerance was set to be 10^{-4} with a cube domain with a side length of 2×10^8 m in order to match the parameters of the error ball case, as seen in Fig. 3.27. Here there are 2937 solutions as compared to the 361 solutions of the error ball case. Similar to the error ball case the solution has a banded structure in multiple directions.

3.5 Summary

In this chapter, methods for determining candidate spacecraft positions are presented for an XNAV system operating without prior information. Methods for finding candidate position in both 2D and 3D are presented which reduce to finding the intersection of infinite sets, in 2D between lines and in 3D between planes. An analytical method is presented which finds an expression for exact solutions which are parameterized by a non-unique vector of integers, $\mathbf{w}$. This method does not guarantee all solutions within a particular domain will be found, nor does it guarantee that solutions will be within a predetermined domain. The analytic model also does not account for measurement error. Two error models are considered, one where the error is modeled as a ball centered at the intersection of two pulsar wavefronts, and any subsequent wavefront must pass within this ball. The other models the error of each wavefront as a banded region and these banded regions must overlap for a solution to exist. Using the error ball model, a numeric scheme for quickly determining if the next wavefront is

within the feasible region is presented, which reduces the computational expense by a factor of N. The error band model is more computationally expensive, but more accurately models the error compared to the error ball. Using these methods the candidate intersections are found for three, four and, five pulsars with phase errors of 10^{-3}, 10^{-4} and 10^{-5}. As the error in the measurement is reduced by an order of magnitude the number of candidate solutions is also reduced by an order of magnitude. Increasing the number of observations by one pulsar reduces the number of solutions by two orders of magnitude. Since the error is proportional to $1/\sqrt{T_{obs}}$, adding additional pulsar measurements is more efficient in terms of total observation time than increasing the accuracy of each pulsar measurement.

CHAPTER 4

PULSAR MEASUREMENT AND SELECTION

In the previous chapter, methods were developed for efficiently finding pulsar wavefront intersections (and therefore candidate positions) using the pulsars selected for NASA's SEXTANT mission. However, the SEXTANT pulsars were selected to minimize the uncertainty of the measured spacecraft position in a relative position update navigation framework. If an XNAV system was operating with a prior position estimate this would be an effective pulsar selection strategy to continue operation with minimal errors. In the case without an initial position estimate this may result in additional candidate spacecraft positions within a given domain. A new method to select candidate pulsars must be developed to find pulsars which minimize the number of candidate solutions within a specified domain to reduce ambiguity in the spacecraft position.

This chapter explores pulsar selection criteria to determine how to best select pulsars to minimize the candidate spacing within a given domain. A set of guidelines are developed using three fictitious pulsars. The pulsar characteristics are varied to independently test the effect of their angular separation, period, and measurement uncertainty on the number of candidate positions within the domain. Using these fictitious pulsars, trends in the number of candidate positions may be found to create guidelines on how to select a set of real pulsars. Using pulsars from an XNAV feasibility study [30], combinations of 3, 4, 5 and 6 pulsars are found and evaluated to determine the size of the domain required to determine the spacing between candidate positions. The spacing between candidate positions determines the maximum domain size which results in a single solution, therefore removing the ambiguity in position.

4.1 Pulsar Selection Criteria

With each x-ray sky survey additional x-ray pulsars are discovered and the number of candidate pulsars increases. Rather than considering real pulsars, we consider hypothetical pulsars to determine trends in pulsar selection which minimize candidate solutions. Three hypothetical pulsars are generated with various directions, period, and phase accuracy to

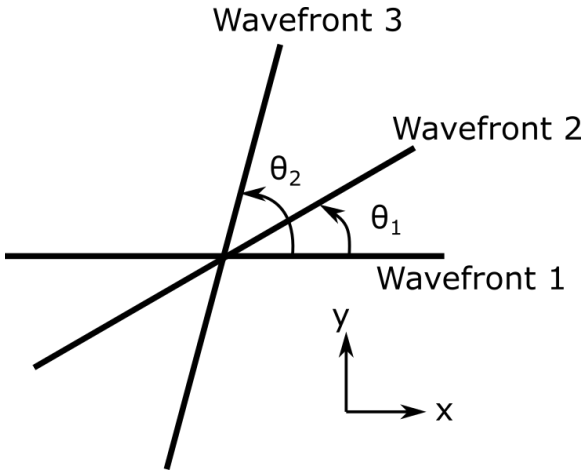

Figure 4.1: Orientation definition of hypothetical pulsars.

capture the range of candidate pulsars. By comparing hypothetical pulsars, guidelines may be determined for selecting real pulsars to minimize the number of candidate solutions. The domain is set to a 2×10^8 m square to reduce computation time and, unless otherwise stated, a phase tolerance of 10^{-3} is considered.

4.1.1 Effect of Pulsar Direction

The first pulsar characteristic considered is the relative direction of each pulsar and corresponding wavefront. Varying each direction results in a problem with 3 parameters; however, this may be reduced to a 2 parameter problem by instead selecting the angle between each direction, as shown in Fig. 4.1. Here θ_1 is the angle between the first and second pulsar and θ_2 is the angle between the first and third pulsar wavefronts. These angles are varied between 0 and π to account for all possible combinations without repetition. In this scenario the orientation of the first wavefront is free and forms the basis for the coordinate system.

Figure 4.2 shows contours of the number of intersections computed as a function of θ_1 and θ_2 when all three pulsars have a period of 0.002 s. The diagonal is not computed as having both pulsars along the same direction would result in no additional information gained. The contour is mirrored along the diagonal since both pulsar period and phase accuracies are identical. The red dots represent combinations which result in more than 1000 solutions, which would reduce the resolution for the remainder of the contours. There are additional outliers concentrated along two lines going from (π/2,0) to (π,π) and from (0,π/2) to (π,π). These lines represent cases where the second and third wavefronts are orthogonal and result in numeric instability. These outliers come as a result of the two pulsars having identical period and error characteristics. If the period of one wavefront is changed slightly from

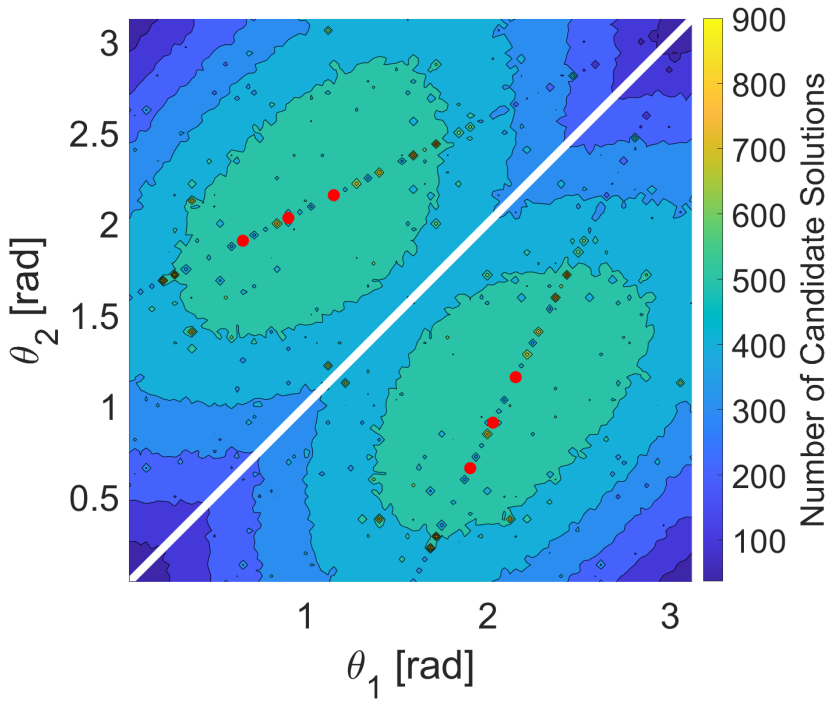

Figure 4.2: Number of solutions for various pulsar directions using a period of 0.002 s for each pulsar; red dots indicate orientations with more than 1000 candidate solutions.

0.002 s to 0.001999 s the linear structure of the outliers is removed; the resulting data are shown in Fig. 4.3. The general solution structure has relatively smooth contours where there are two peaks when the wavefronts are at an even spacing apart, $\theta_1 = \pi/3$ and $\theta_2 = 2\pi/3$ or vice versa. The corner cases where all three pulsars are most closely aligned performs the best in terms of limiting candidate solutions.

Having pulsar wavefronts nearly parallel gives the fewest candidate solutions regardless of the pulsar periods selected. Two additional cases are shown in Fig. 4.4. Figure 4.4(a) is the case where the period of the first pulsar is set to 0.0015 s and the other two remain at 0.002 s, and in Fig. 4.4(b) the first pulsar has a period of 0.001 s, the second has a period of 0.005 s and the third has a period of 0.01 s. For the case where the first pulsar's period is 0.0015 s there are more solutions in the domain than compared to any of the other cases, whereas the case where all three periods results in the fewest solutions in the domain. In both of these cases the corners again have the best performance in terms of the fewest candidate solutions. In the absence of other requirements, the number of candidate solutions within a domain for absolute position determination is minimized when the pulsars are selected such that they are nearly in the same direction.

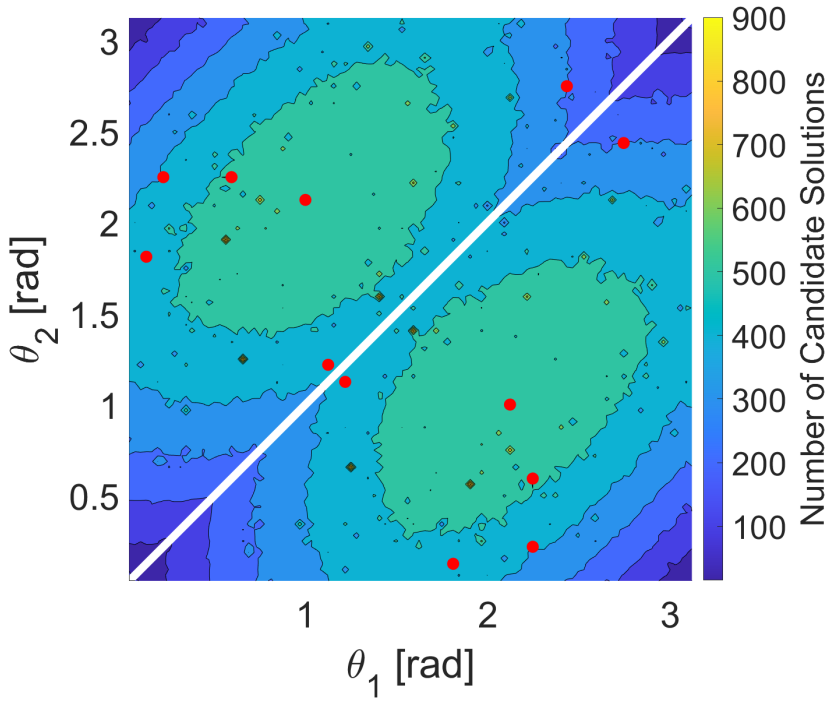

Figure 4.3: Number of solutions for various pulsar directions using a period of 0.001999 s for the first pulsar and 0.002 s for the other two pulsars; red dots indicate orientations with more than 1000 candidate solutions.

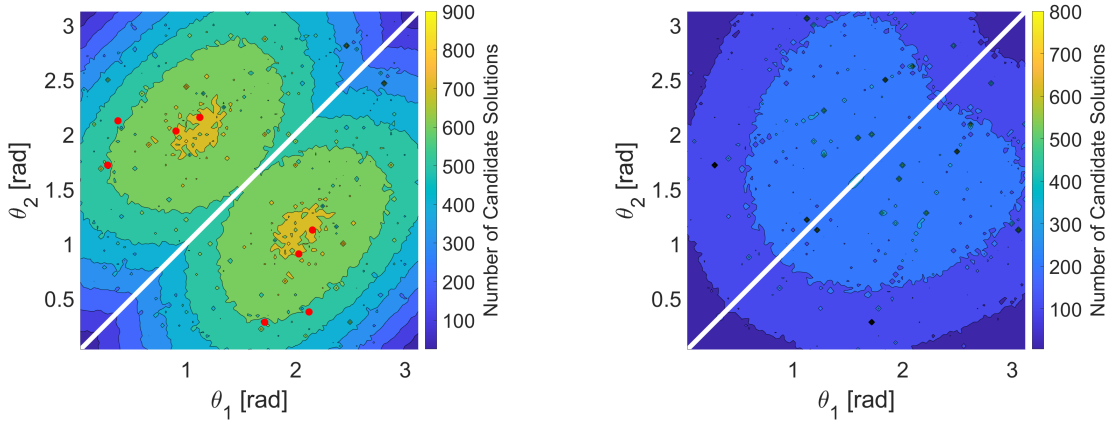

Figure 4.4: Number of solutions for various pulsar directions with a change in the period of (a) first pulsar to 0.0015 s or (b) first pulsar to 0.001 s, second pulsar to 0.005 s and third to 0.01 s; red dots indicate orientations with more than 1000 candidate solutions.

4.1.2 Effect of Period

As seen above, the period of the selected pulsars may have a significant effect on the number of candidate solutions. There is no defined upper or lower bound for the pulsar period; however, when considering all known millisecond pulsars, majority are within a range of 0.02 s to 0.001 s [75], including those used for this analysis. The pulsar directions are set to 60° apart to show the maximum number of solutions for the given periods. In order to better visualize the results, the period of the third pulsar is fixed to some value within these bounds.

The boundary cases are considered where the third pulsar has a period of 0.001 s and 0.02 s and the results are shown in Fig. 4.5. Here the contours are presented on a log scale plot with the data truncated at 500 candidate solutions for the case where the period of the third pulsar is set to 0.001 s and to 100 solutions for the case where the period is 0.02 s. The truncation is necessary to provide contrast since the peak number of solutions is far greater than the remainder of the domain. For the case where the fixed period is 0.001 s the peak number of solutions is 3561 and for the 0.02 s case it is 1267. Both of these peaks occur in the lower left corner of the figure where the periods of the two varying pulsars are at their minimum. Both of these cases suggest that, to minimize the number of candidate solutions, pulsars with as large of a period as possible should be selected. As the periods of the pulsars are increased the number of wavefronts within the domain decreases resulting in fewer candidate points which must be evaluated for additional intersections. In the case where the period is 0.001 s there are 456 wavefronts within the domain; when the period is increased to 0.02 s the number of wavefronts is decreased to 23. Selecting three pulsars with period of 0.02 s

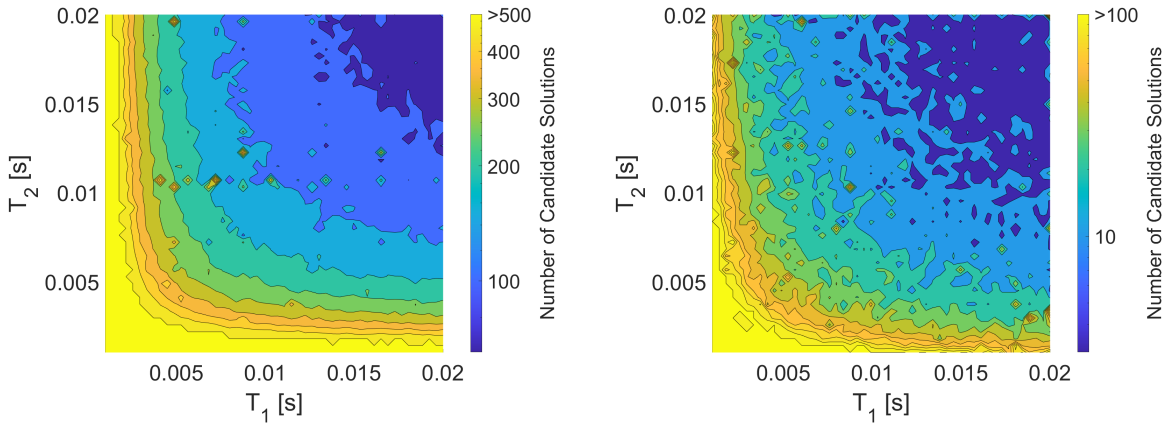

Figure 4.5: Number of candidate solutions for various pulsar periods with the third pulsar's period fixed to (a) 0.001 s and (b) 0.02 s.

results in less than 10 solutions compared to the 3561 candidate solutions in the case where all three have a period of 0.001 s. In the absence of other measurement criteria, pulsars with large periods are better candidates for minimizing the number of solutions within a given domain.

4.1.3 Effect of Measurement Error

In all prior analysis the pulsar phase accuracy was set to be the same for all pulsars, however this does not need to be the case. The phase accuracy of the pulsars will be varied between 10^{-3} and 10^{-5} independently to keep the bounds consistent with the prior analysis. The pulsar periods are set to 0.002 s and the directions are set 60° apart. The third pulsar's phase error bound will be fixed to either 10^{-3} or 10^{-5} to determine the boundary cases, and the resulting number of candidate intersections can be seen in Fig. 4.6, note that both axis are on a log scale. In both cases, as the error in the pulsar measurements is reduced, the number of candidate solutions decreases. The upper right corner of Fig. 4.6(a) represents the case where all three pulsars have an error tolerance of 10^{-3} and the lower left corner of Fig. 4.6(b) is the case where all three have a phase tolerance of 10^{-5}. Fig. 4.6(a) shows that improving the accuracy of only one pulsar from 10^{-3} to 10^{-5} gives rapidly diminishing returns, whereas improving both pulsar accuracies simultaneously performs better.

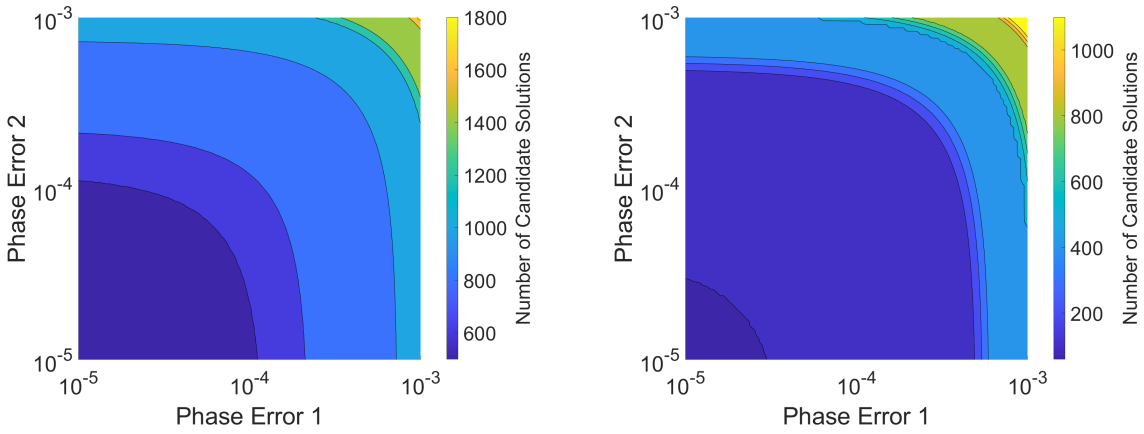

(a) (b)

Figure 4.6: Number of candidate solutions for various phase errors with the third pulsar having a phase error of (a) 10^{-3} and (b) 10^{-5}.

4.1.4 Effect of Phase Estimation Parameters

In reality all pulsars will have a different measurement uncertainty for a given observation time which can be approximated by Eq. 2.23. In Section 3.3, this equation was simplified since terms within the integral are constant and may be integrated for each pulsar, commonly refereed to as the integration parameter. The previous analysis only considered changing the measured phase accuracy without considering the observation time required to generate that measurement. The three pulsars will be assigned independent integration parameters of 5, 50, and 100 for pulsars 1, 2, and 3 respectively. Using this integration parameter and observation times between 1000 s and 10^7 s, the expected phase accuracy may be computed and the resulting number of intersections found. Figure 4.7(a) shows the case where the first pulsar observation has a measurement time of 1000 s, and in Fig. 4.7(b) the first pulsar has an observation time of 10^7 s. The red curves on these figures are lines of equal observation time on a log scale. On these figures there are two sets of x-axis and y-axis. The lower x-axis and left y-axis show the pulsar observation time, while the upper x-axis and right y-axis represent the phase accuracy of the corresponding observation time. Once again the figures show that in terms of phase accuracy it is best to improve the phase accuracy of both measurements simultaneously. When observation time is considered, the contours are shifted such that increasing the observation time of the second pulsar is more beneficial than increasing the observation time of the third measurement. However, increasing only one measurement is not as efficient as increasing both measurements. Looking at Fig. 4.7(a), if the second pulsar is observed for 10^7 s and the third pulsar is observed for 1000 s there

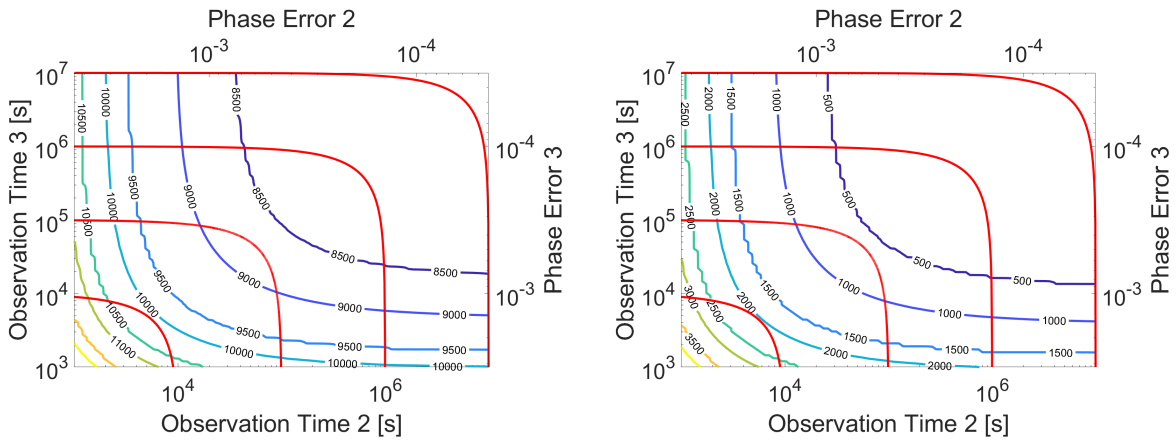

Figure 4.7: Contours of the number of candidate solutions for varying observation times, and the corresponding phase accuracy where the first pulsar has an observation time of (a) 1,000 s and (b) 10^7 s. In the red curves of equal observation time, on a log scale.

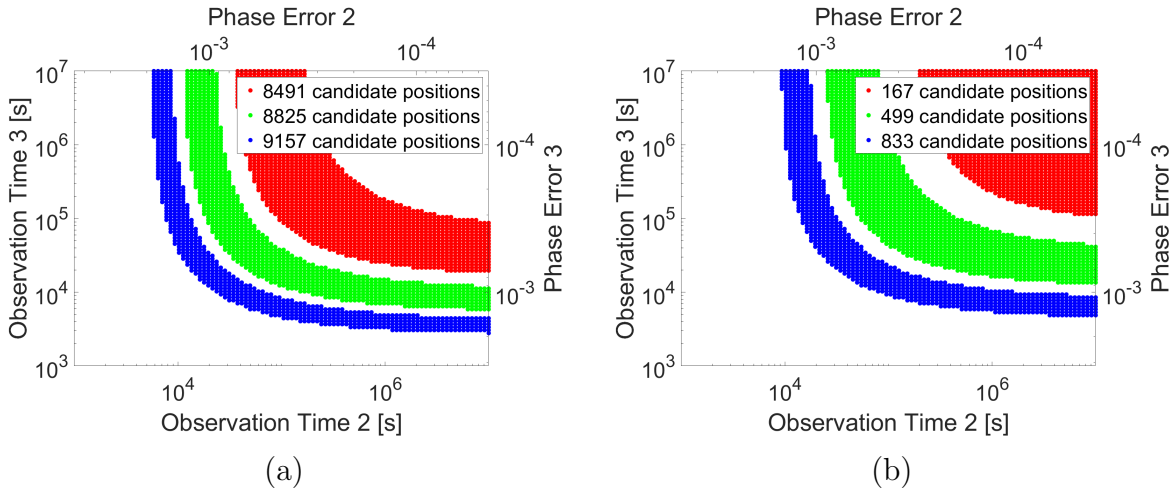

(a) (b)

Figure 4.8: The three most common results for the number of candidate solutions with varying observation time where the first pulsar is observed for (a) 1,000 s and (b) 10^7 s. The red dots show observation times which result in the most commonly found number of candidate solutions, the green dots show the second most common, and blue dots the third most common.

would be approximately 10,000 candidate positions. A similar result could be obtained by measuring each pulsar for 5,000 s.

Increasing the observation time for each measurement by a small amount is not guaranteed to reduce the number of solutions. When considering the case where the first pulsar is observed for 1000 s, there are 1798 combinations of observation times for pulsars two and three which result in 8491 candidate positions. In Fig. 4.8(a), these are represented as the red dots and are the most commonly found number of candidate solutions. The green dots show the second most commonly found number of candidate solutions, 8825, which is found for 1129 observation time combinations. The third most commonly found number of candidate solutions is 9157 which was found 838 times and are shown in the green dots. Of the 10,000 combinations of observation time evaluated, 3765 combinations resulted in one of the three most common number of candidate solutions. Figure 4.8(b) shows the three most commonly found number of candidate solutions for the case where the first pulsar is observed for 10^7 s. Here the most common number of candidate positions is 167 which is shown in 1694 red dots, the green dots show 1560 combinations with 499 candidate solutions, and the blue dots are 1039 combinations with 833 candidate positions. In this case, 4293 of 10,000 combinations result in one of the three most common number of candidate solutions. For both cases, the combinations of observations times which results in equivalent number of candidate solutions are in banded regions and combinations of observation times between these bands are more transient. As the phase error is reduced, the bands of equivalent

number of candidate solutions become thicker requiring more and more observation time in order to reduce the number of candidate solutions. If the observation time of one of the pulsar measurements is increased by too small an amount, it may not reduce the number of candidate solutions within the domain.

4.2 Pulsar Selection From Real Pulsars

In a real scenario, selecting a set of pulsars to observe requires a trade off between the pulsar period and relative directions. To determine how to best select form a real group of pulsars, this study will consider the set of pulsars used by Shemar et. al. in their feasibility study of XNAV [30]. Pulsar B0628-28 is removed for this study since it represents an outlier in terms of period, with a period is 1.244 s while the next largest period is 0.408 s. The remaining 34 pulsars are considered and combinations of 3, 4, and 5 pulsar observations are evaluated to determine the number of candidate solutions in a given domain. For each combination the average period is found and the average angular separation is computed by a dot product and bounded to be between $[0,\ \pi/2]$. Note that this is the average angular separation of wavefronts, not of the pulsars' directions. When computing candidate intersections using these sets of pulsars a phase accuracy of 10^{-3} is assumed.

Directly testing all combinations is computationally expensive as some pulsar combinations may result in several million candidate intersections on a large domain. Instead, a simple algorithm may be used to significantly reduce the computational expense, Algorithm 4. The algorithm works by starting with a small domain, for this case the domain is set to a 2×10^6 m square, and each pulsar combination is checked one at a time. Steps 4-7 initialize the current pulsar combinations by loading in the pulsar parameters of the set, finding the bounds on the number of wavefronts in the domain, and sorting the pulsars based on the maximum number of wavefronts. Step 9 calculates the intersection of the banded region of the first two pulsars. If the intersection is within a previously evaluated region, step 12 skips the wavefront combination and proceeds to the next one. Step 18 does the same for the case where the candidate is outside of the feasible region. If the current wavefront combination is outside of the domain, steps 14-16 are a check statement to see if any additional intersections will be found if the second wavefront is incremented to the next value. If the candidate is determined to be within the new feasible regions, additional pulsar measurements are evaluated based on the banded error model as described in Section 3.3.3. The wavefront indices i_1, i_2 are then incremented based on Algorithm 4 until all candidate intersections within the domain are found. Only combinations which have a single solution are passed retained, step 26, since

Algorithm 4 Rapidly search through candidate sets of pulsars

```
Set N_p = the number of pulsar combinations to evaluate, l = domain size, l_old = 0 (last domain size)
while N_p > 0 do
    for j=1:N_p do
        Load pulsar combination parameters
        Compute index upper and lower bounds for all pulsars in set j (LB_1, UB_1, ...)
        Sort pulsars based on wavefront bounds
        Initialize Check variable to 0 (Determine when to break loop)
        Set i_1 = 0, i_2 = 0
        while i_2 ≤ UB_2 do
            Compute candidate vertices
            if Vertices < l_old then
                Continue to next i_2
            if Vertices > l then
                if Check==1 then
                    Define upper bound of i_2, i_U
                    Break loop
                else
                    Continue to next i_2
            else
                Evaluate Pulsar(s) 3, 4, ...
                Check = 1;
            i_2 = i_2 + 1
            if More than one candidate position exists then
                Break to evaluate the next combination of pulsars
        Preform similar computations for remainder of Algorithm 3
                (Evaluate down/left/right)
                        ⋮
        Save candidate positions
    N_p = number of set in j which had only 1 candidate position
    l_old = l, increase l
```

the spacing between candidate solutions for these pulsars has not yet been determined. The current domain size is saved in step 27 and the domain size to evaluate is increased. If more than one candidate position is found, step 24 immediately exits the loop and returns to step 3 to evaluate the next pulsar combination. This algorithm is searching to find what domain size is required to find multiple solutions for a set of pulsars, evaluating the full domain for each set, after an additional candidate position is found, may be computationally expensive when a large number of pulsar combinations are considered. This algorithm results in a computation time which is proportional to $N_p(l^2 - l_{old}^2)$, where N_p is the number of pulsar combinations considered, l is the current domain size, and l_old is the previous domain size. By starting with a small domain, combinations which result in many solutions are removed early which improves performance as the domain grows. Once no combinations remain in the set, the combinations which required the largest domain size to find additional solutions may then be fully evaluated on a largest domain to determine the number of solutions. The combination which results in the fewest candidate positions is then considered the best combination of pulsars to use. For all following cases a phase accuracy of 10^{-3} will be used for each pulsar observation.

4.2.1 3 Pulsar Observations

Using the 34 candidate pulsars, each possible combination of 3 pulsars is found resulting in 5984 sets of pulsars. The resulting distribution of candidate pulsars can be seen as black dots in Fig. 4.9(a), for which the required domain side length to find multiple solutions for all sets of pulsars is 2×10^{10} m. The 50 combinations which results in the fewest solution are highlighted in Fig. 4.9(a) as red dots and also presented in Fig. 4.9(b) in terms of the resulting number of candidate solutions. The smallest number of candidate solutions with a domain size of 2×10^{10} is 9, which is significantly reduced from the 2,016,493 candidate solutions using the initial set from Table 3.1. Although the best solutions (ones that present the fewest number of candidate positions) are concentrated in the region with low average angular separation and large average period, not every combination in this area performs similar to the "best" combinations.

This procedure may be repeated with constraints on the angular separation between the pulsars to be larger than 1 degree, resulting in 5578 candidate combinations, or larger than 10 degrees resulting in 3027 combinations. Figure 4.10 shows the distribution for the 1 degree separation case along with the 50 combinations which most reduce the number of candidate intersections, and Fig. 4.11 shows the 10 degree separation case. For the 1 degree case, the smallest number of candidate solutions in a 2×10^{10} m domain is 9. Again, it appears

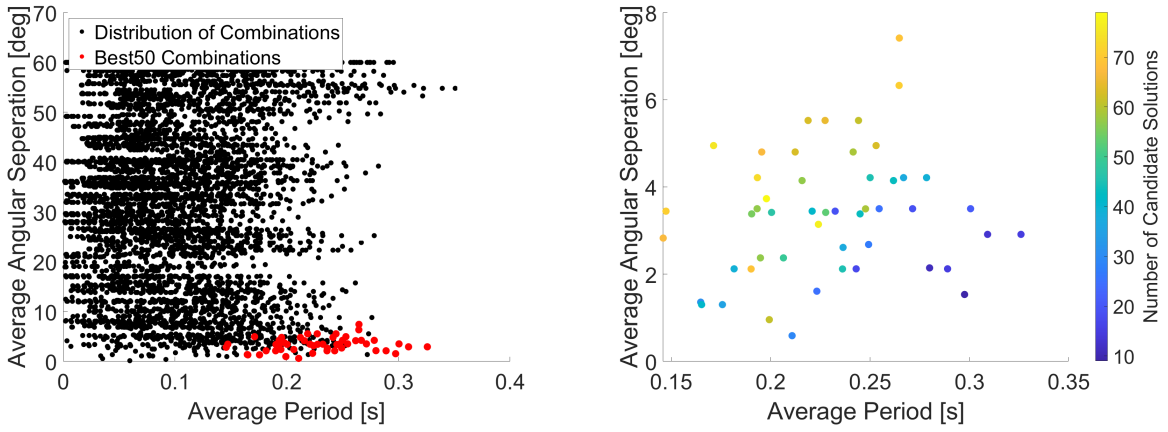

(a) (b)

Figure 4.9: Distribution of average period vs average angular separation for (a) all pulsar combinations with the best 50 highlighted in red (b) the best 50 combinations with the number of candidate solutions shown.

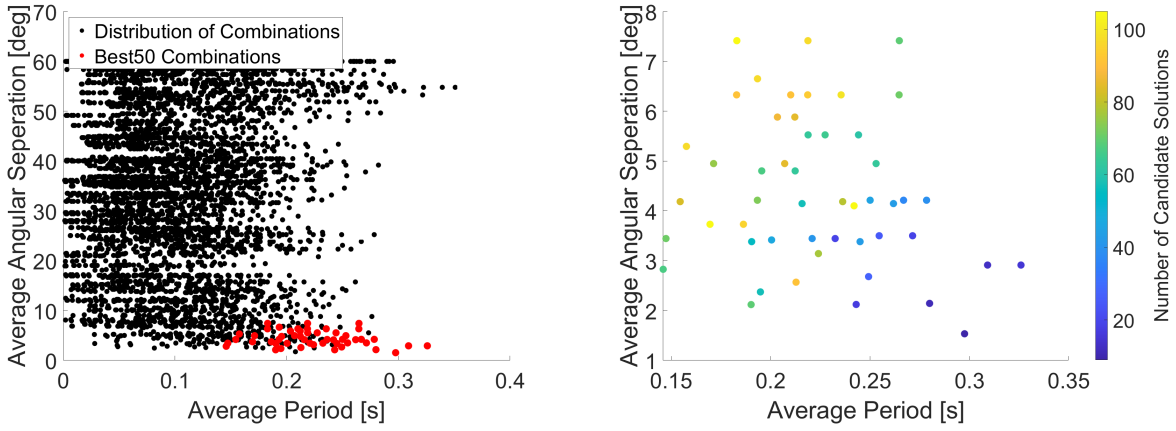

(a) (b)

Figure 4.10: Distribution of average period vs average angular separation with a minimum of 1 degree of angular separation constraint for (a) all pulsar combinations with the best 50 highlighted in red (b) the best 50 combinations with the number of candidate solutions shown.

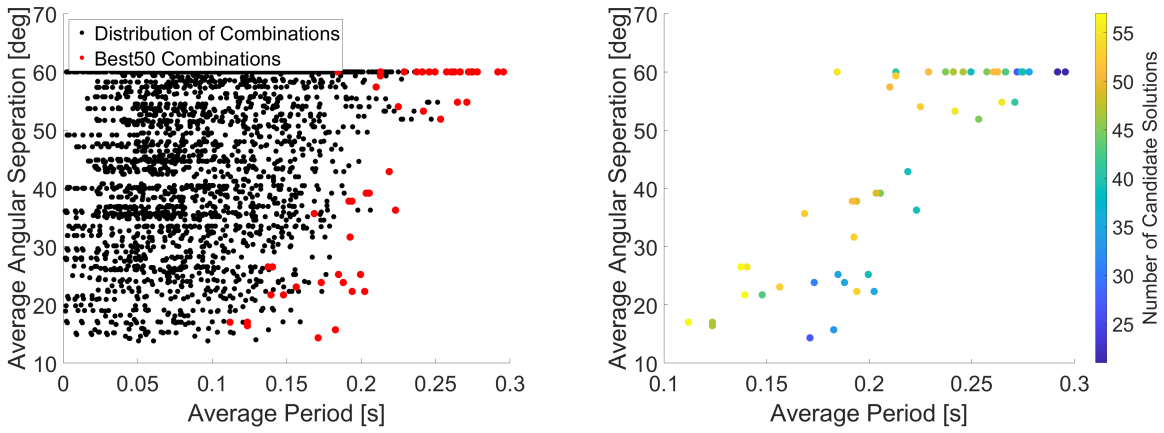

(a) (b)

Figure 4.11: Distribution of average period vs average angular separation with a minimum of 10 degree of angular separation constraint for (a) all pulsar combinations with the best 50 highlighted in red (b) the best 50 combinations with the number of candidate solutions shown.

that having a smaller angular separation is more significant than having a smaller period as solutions are concentrated on the lower boundary of Fig. 4.10 and not along the right boundary. The 10 degree separation constraint removed approximately half of the pulsar combinations, including the best 50 combinations for both the unconstrained case and the 1 degree separation case. With this constraint the best 50 solutions are now concentrated closer to the boundary of larger average period rather than smaller angular separation, with the best solution near the maximum angular separation boundary. Due to the constraints on the problem the required domain size to resolve all combinations was reduced to a square domain with a side length of 6.32×10^{9} m and in this domain the set with the fewest possible candidate positions had 21 candidates.

4.3 4 Pulsar Observations

The above process may be repeated with a fourth pulsar measurement, without a constraint on the angular separation, and the 46,376 combinations are searched through to find the best combination of four pulsars, Fig. 4.12. As the number of pulsar measurements increases the domain size required in order to determine the candidate spacing is also increased. The required side length for the domain is 4.48×10^{11} m and in this domain the minimum number of candidate solutions is 5. Comparing this case to the prior case with 3 pulsars, the location of the best 50 solutions is similar in that majority of them occur with larger average period

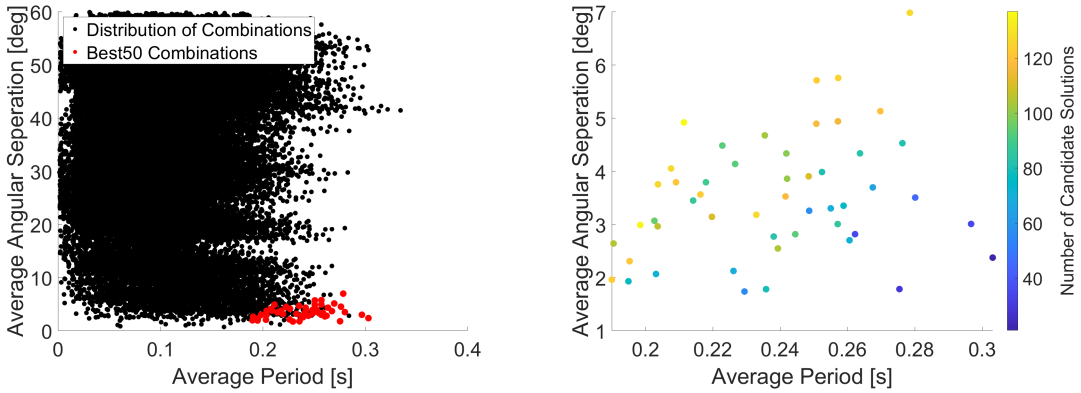

(a) (b)

Figure 4.12: Distribution of average period vs average angular separation for 4 pulsar combinations (a) all pulsar combinations with the best 50 highlighted in red (b) the best 50 combinations with the number of candidate solutions shown.

and smaller average angular separation. However, for the best 50 combinations of four pulsars, the smallest average period is larger than it was for the three pulsar case.

4.4 5 Pulsar Observations

A combinations of 5 pulsars may be considered, however now there are 278,256 potential combinations to consider. For each increase in puslar observations the domain size required to resolve all combinations would increase. This combined with the increase in the number of combinations may make this problem too computationally expensive to solve in a reasonable amount of time. Therefore an objective function is defined as

$$J = \mu \left(\frac{P - P_{max}}{P_{max}} \right)^2 + (1 - \mu)\theta^2; \tag{4.1}$$

where P is the average pulsar period, P_{max} is the maximum average pulsar period, θ is the average angular separation, and μ is a weighting factor. By adjusting the value of μ the objective function will weight the average period and angular separation differently. To capture the trends from the 3 and 4 pulsar cases with no angular separation constraint the weight will be set to 0.99, and the 100 lowest objective functions are selected, combinations may be seen in Fig. 4.13(a). Using these 100 combinations the domain size required to resolve the domain size required for position ambiguity may be done, and the best 15 solutions are shown alongside the 100 selected combinations, Fig 4.13(b). In order to determine a high-performing set of 5 pulsars, a square domain with a side length of 3.46×10^{12} m was used,

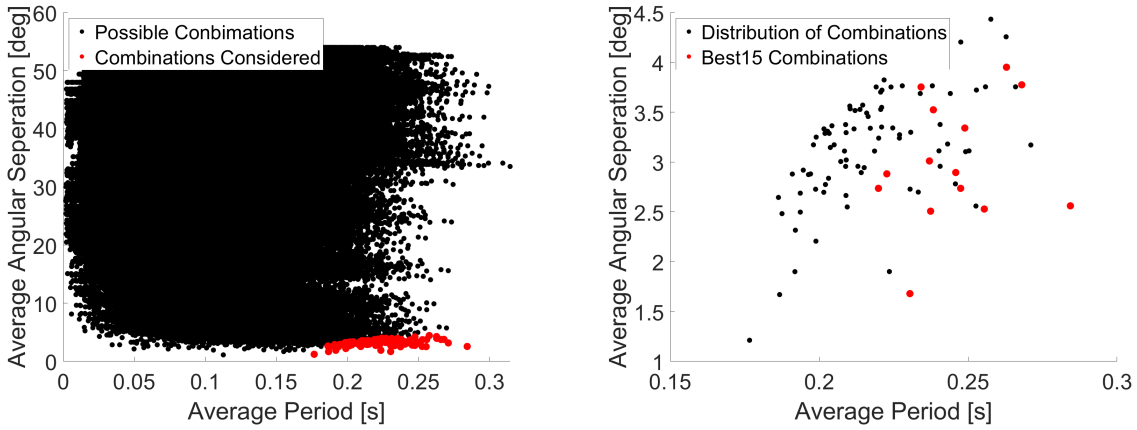

(a) (b)

Figure 4.13: Average period and angular separation for 5 pulsars (a) the 100 selected pulsar combinations in red and all combinations in black (b) the 100 combinations in black and the best 15 in red.

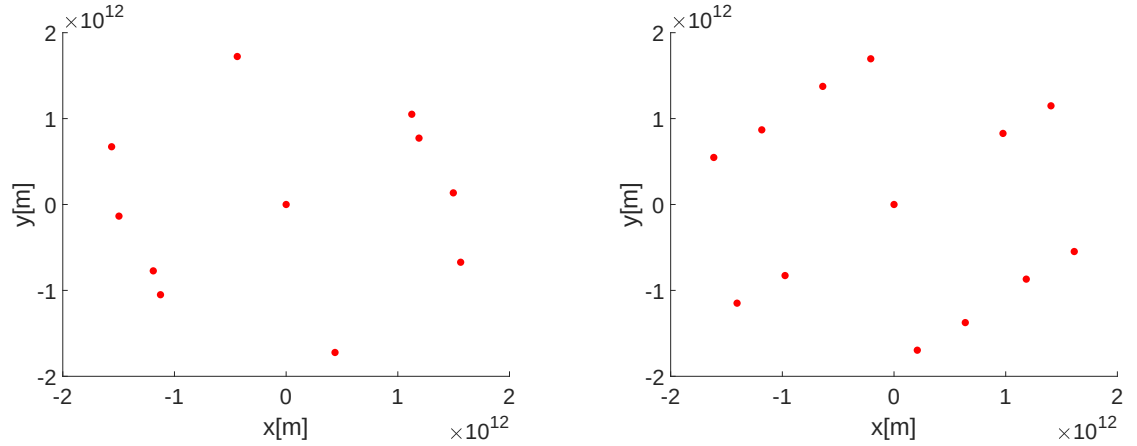

(a) (b)

Figure 4.14: Distribution of the candidate positions for (a) the 11 solution case (b) the 13 solution case.

and the best two combinations resulted in 11 and 13 candidate positions. Figure 4.14 shows distributions of candidate solutions for the two best solutions. Both cases have significant spacing between the candidate positions, however this spacing is not uniform in either case. The main similarity between the cases are the large distance between the exact solution at the origin and all other solutions. This gap is so large that the entire orbit of Mars fits within this area.

4.5 Trends in the Required Domain Size to Fully Resolve Position

Comparing the results of the 3, 4, and 5 pulsar cases, as the number of pulsars considered increased by one, the domain size required to resolve the combinations increased by an order of magnitude. The square domain for the 3 pulsar case had a side length of 2×10^{10}, for the 4 pulsar case 4.48×10^{11} m and the five pulsar case had a side length of 3.46×10^{12} m. If this trend continues observing a sixth pulsar may require a domain size on the order of 10^{13} m to resolve, which would capture the orbit of Pluto. As previously mentioned, the pulsar combinations with the largest average period and smallest average angular separation tend to perform the best.

Looking at Fig. 4.9(a), 4.10(a) and 4.12(a) it can be seen that there are some gaps between the best 50 combinations. The domain at which candidate pulsar combinations are removed can be explored and for the case of 3 pulsars are shown in Fig. 4.15. As the domain size is increased, candidate are removed with a wide range of angular separation and average period characteristics. On the final domain, 2×10^{10} m, there still were candidates with an average angular separation of over 40° with average periods less than 0.1 s, while in the first domain, 2×10^{7} m, there were candidates with smaller average angular separation and larger average periods that were removed. It may not be possible to directly determine which combination is best by looking at their average characteristics, rather these characteristics are couple with the independent periods and pulsar normal vectors. If given an average period and angular separation there is no way to know what domain size would be required to resolve the system without performing the computation. However, it is justified to say that the set which will minimize candidate spacing the most will have a larger average period and smaller average angular spacing, however there is no way to determine which specific combination that it will be.

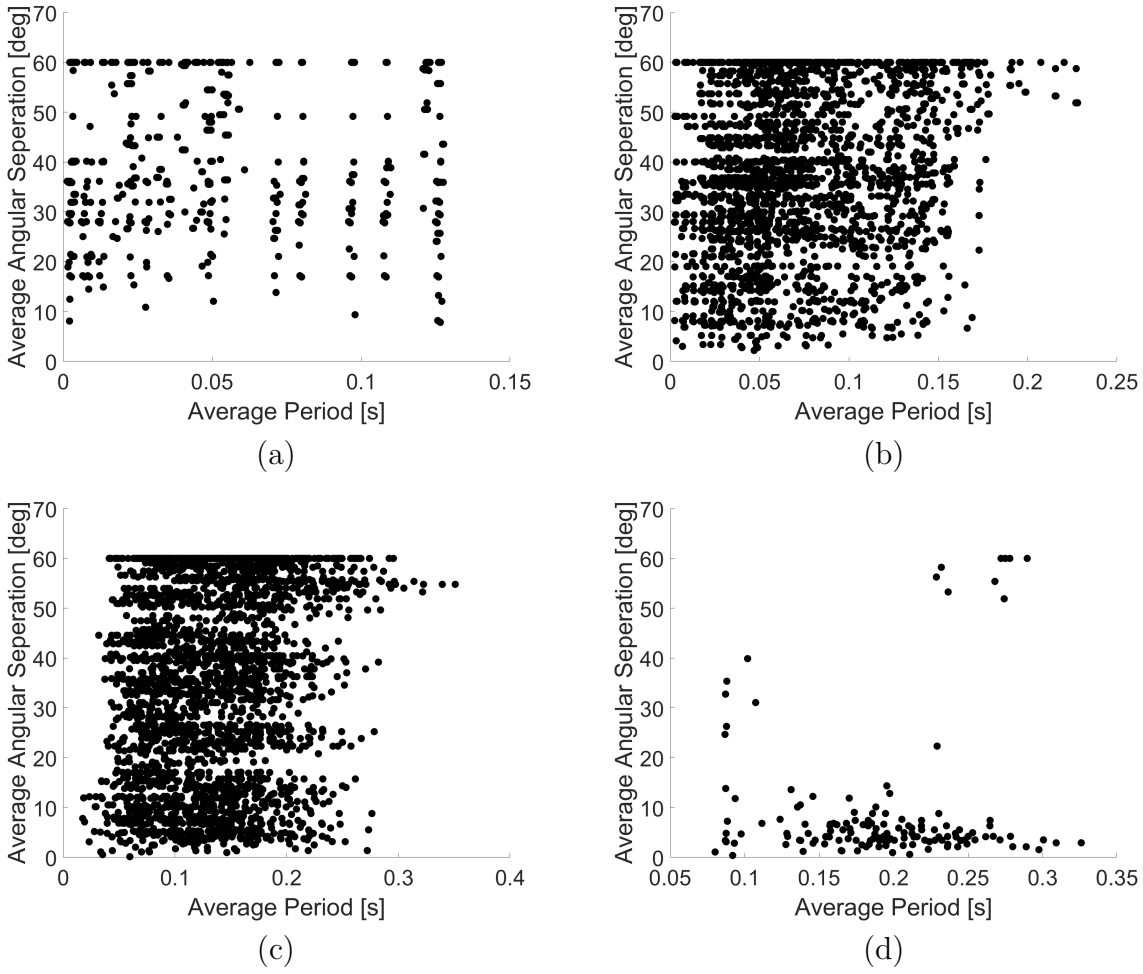

Figure 4.15: Distribution of the pulsar combinations which yielded multiple solutions in a square domain with side length (a) 2×10^7 m (b) 2×10^8 m (c) 2×10^9 m (d) 2×10^{10} m.

4.6 Summary

Criteria on the relative angular separation of the pulsars selected, their period, and measurement uncertainties were determined to minimize solution density over a given domain. Results indicate the number of candidate solutions is minimized for pulsars whose angular separation is as small as practical with as large of a period as possible. Further, it is more beneficial to improve the measured phase accuracy of all pulsars simultaneously rather than focusing on one pulsar. A set of 34 pulsars was selected and the average period and angular separation for all combinations was found. The resulting number of candidate solutions were found for each combination and those with both a small angular separation and large period performed the best with respect to minimizing the number of candidate solutions in a given domain.

CHAPTER 5

XNAV STATE DETERMINATION WITHOUT PRIOR INFORMATION

In the previous chapter, results indicated that a set of 5 pulsars requires a square domain side length on the order of 10^{12} m to find additional candidate positions; solving the absolute position determination problem with a properly selected set of pulsars would result in a sufficiently large candidate spacing to remove position ambiguity entirely over this domain size. A few assumptions must be made in order for position determination to be performed without prior state information. It is assumed that the spacecraft has an accurate onboard clock; for this analysis, it is assumed to be a perfect clock. The spacecraft is assumed to have an accurate x-ray detector such that the phase of the pulsar waveform may be estimated with an uncertainty 10^{-3}, as well as an attitude determination and control system to keep the detector pointed to the pulsar for the duration of the observation; current state-of-the-art star trackers and reaction wheels can provide the required pointing capability. A catalog of pulsar waveforms must be stored onboard along with the timing models at the Solar System barycenter. The spacecraft must also have sufficient onboard computational resources to carry out the evaluation of all possible candidate positions. If these conditions are met, the spacecraft may determine its position within the Solar System without ambiguity.

The position determination process is preformed by evaluating all possible candidate positions using the methods described in this dissertation, and increasing the number of pulsar observations until a unique solution is found. The process begins by recording all photon time of arrivals from the desired pulsar. In the absence of an initial position estimate the photon time of arrivals cannot be shifted back to the Solar System barycenter, or other reference location; however, a phase and frequency measurement of the pulsar signal may still be estimated without shifting the time of arrivals. A phase difference may still be computed with respect to the reference signal, which places the vehicle at the Solar System barycenter. Using these phase values sets of lines may be constructed from the Solar System barycenter outwards for each pulsar observation. Once three sets of lines may be computed, the algorithms previously described may be used to start computing the feasible intersections of wavefronts from the three pulsar observations for a given domain size. If a fourth pulsar is observed, only candidate positions which were feasible for the first three pulsar observations

need to be evaluated for intersection of wavefronts from the fourth pulsar observation. The process repeats for any additional pulsar observations. If position ambiguity is found, additional pulsar observations are required. This process can be demonstrated using various combinations of pulsars and is applied to NASA Insight's trajectory, Juno trajectory and New Horizon's trajectory to illustrate the efficacy of the proposed method.

5.1 Earth-Mars Transfer Trajectory

A set of pulsars can be selected such that the candidate spacing is sufficiently large to cover the orbit of Mars, and resolve missions to the inner Solar System. The Earth-Mars trajectory of NASA's Insight lander is considered and is shown in Fig 5.1 [145, 146]. Here the spacecraft position is set to the first trajectory correction maneuver (TCM), which is shortly after the spacecraft has been launched. The domain side length was set to 6×10^{11} m to cover the entire Mars orbit, and the observation phase accuracy is set to 10^{-3}, consistent with individual pulsar observation times of approximately one day.

5.1.1 5 Pulsar Observations - No Measurement Error

Using the 5 pulsar set which resulted in the fewest candidate positions from Chapter 4, a single XNAV solution is found which coincides with the true spacecraft location. The selected pulsars have very small angular separation with normal vectors which are all nearly along the y-direction, which means that their wavefronts are nearly parallel to the x-direction. This results in an uncertainty region which is skewed to be much longer in the x-direction, approximately 300 km, compared to the y-direction, approximately 7 km, which results in an area of 8.7921×10^4 km^2 for the feasible region, Fig. 5.1(b). The main goal of this analysis is to demonstrate the lack of position ambiguity, not to reduce the position uncertainty. In this example no measurement error is imposed on the measurement, only measurement uncertainty. The spacecraft is measuring the true phase which implies that one wavefront from each pulsar coincides with the true position and the uncertainty region is then centered about this true location. For clarity in Fig. 5.1(b), and all figures showing the feasible region, the values are shifted such that the true position is set to 0 in order to make the uncertainty bounds more clear.

The above procedure may be repeated for other locations in the orbit, and again there is only one resulting candidate solution. Figure 5.2 shows the candidate solutions and feasible spacecraft position at TCM 2, which is in the cruise stage of the transfer, and Fig. 5.3 shows

the results for TCM 6 which is just before atmospheric entry at Mars. For both cases there is only a single solution which occurs at the true solution. The feasible intersection region at all 3 TCM locations is the same with the true solution at its center, which is due to the lack of measurement error. As a result the wavefronts of each measurement coincide with the true position and the center of the feasible region is then centered on the true position.

5.1.2 5 Pulsar Observations - Random Measurement Error

To better capture a realistic scenario, a uniform random phase was added to each pulsar measurement. The magnitude of the measured phase was constrained to be less that 10^{-3}, and the spacecraft's position was set to TCM 1. Four sets of random uniformly distributed phase offsets were tested and two resulted in only one candidate position at TCM 1, while the other two resulted in two solutions. Figure 5.4 shows what the feasible intersection region looks like for the two cases which resulted in a single solution, and Fig. 5.5 shows the one additional solution found for the two seeds which resulted in additional solutions. By applying measurement error, the location of the vertices may change, however the area of the feasible region may only stay the same or decrease. The uncertainty region for each measurement is centered about the wavefront measurement and for the case with no measurement error all wavefronts are intersecting at the true solution. When measurement error is applied these wavefronts are not all coinciding at the same point which may cause some wavefronts to overlap less of the feasible region than in the case with no measurement error.

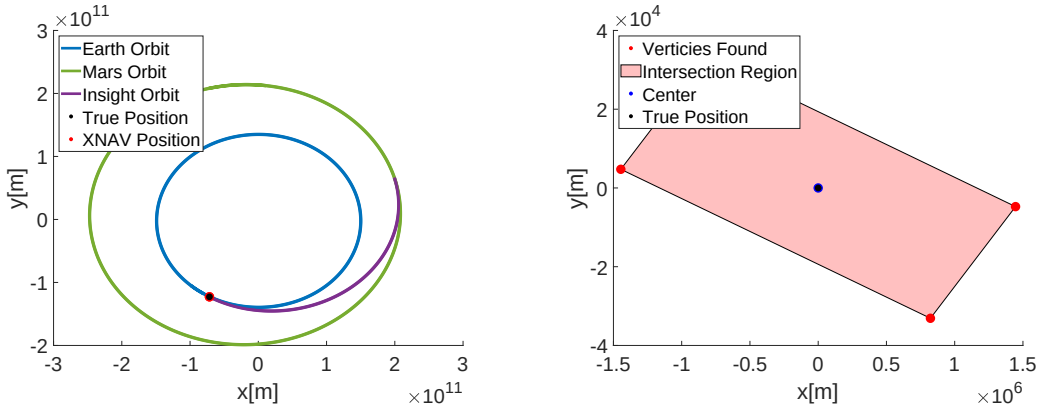

Figure 5.1: At TCM 1 (a)XNAV solutions in a domain covering the orbit of Mars along with relevant trajectories (b) The feasible region of the XNAV solution centered at the true spacecraft location.

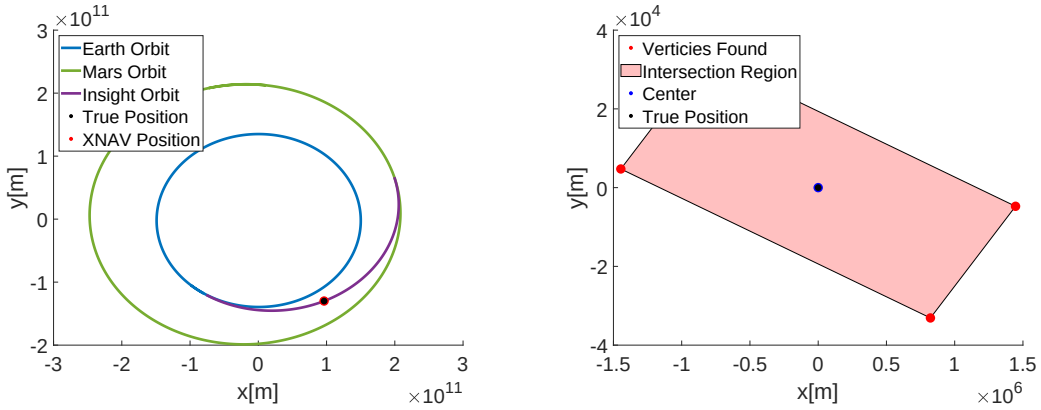

(a) (b)

Figure 5.2: At TCM 2 (a)XNAV solutions in a domain covering the orbit of Mars along with relevant trajectories (b) TThe feasible region of the XNAV solution centered at the true spacecraft location

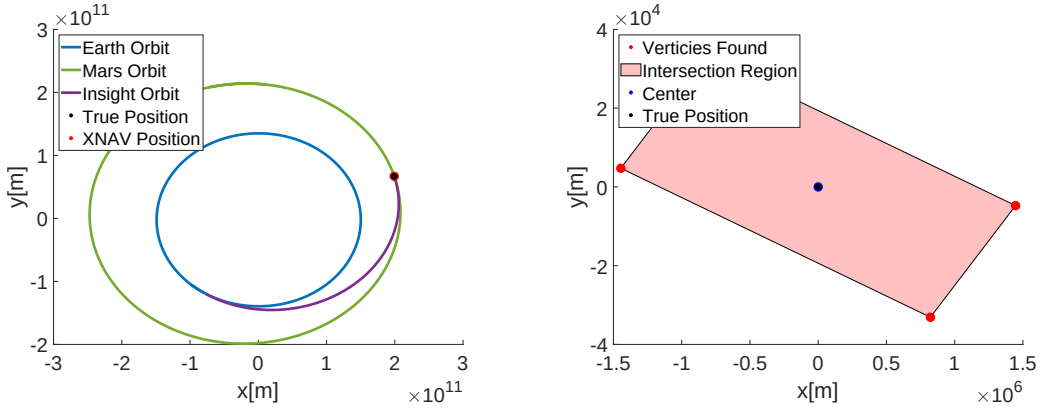

(a) (b)

Figure 5.3: At TCM 6 (a)XNAV solutions in a domain covering the orbit of Mars along with relevant trajectories (b) The feasible region of the XNAV solution centered at the true spacecraft location

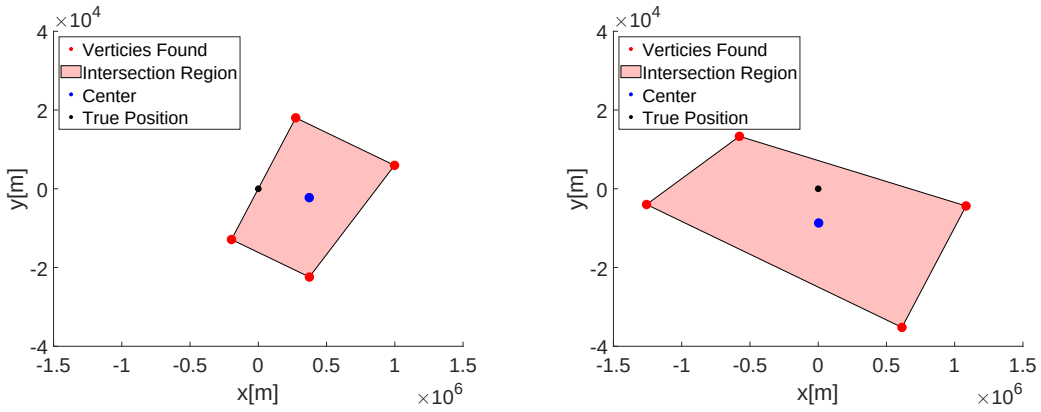

Figure 5.4: The feasible intersection region at TCM 1 with random measurement error for two different random number generator seeds.

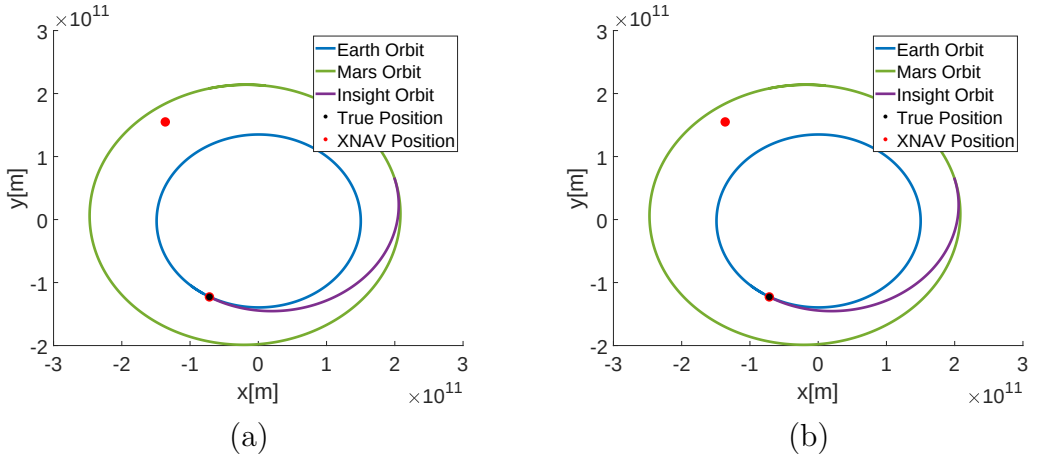

Figure 5.5: The candidate positions at TCM 1 with random measurement error for two different random number generator seeds which caused position ambiguity.

5.1.3 7 Pulsar Observations

Since the case of 5 pulsar measurements cannot reliably yield a single solution for the applied random error, additional pulsars must be observed. One option would be to add a sixth pulsar measurement, however, due to the size of the feasible region, a case could be made to incorporate pulsars which reduce the size of the feasible region. Shemar et al. presents a best set of 3 pulsars to measure to reduce position uncertainty [30], these can be incorporated into the measurement. However if these 3 measurements are used (which are selected to reduce position uncertainty, as opposed to position ambiguity, as discussed in Ch. 4), 7 observations are required as 6 would result in 3 solutions within the domain. These additional solutions come as a result of the structure of the uncertainty region. Looking back to Fig. 5.1(b) the uncertainty region is approximately 300 km long in the x-direction, but the pulsars selected to reduce the size of the uncertainty region have wavelengths on the order of smaller than that. In some cases, a single uncertainty region may actually be split into two smaller uncertainty regions making one candidate position become two. This requires additional measurements to overcome, which is why 7 pulsar measurements are used. The best combination of 4 pulsars has been selected along with 3 pulsars which minimize the XNAV uncertainty in a conventional XNAV operation [30], for a total of 7 pulsar observations. At TCM 1 the resulting position and uncertainty region for the case with no error is presented in Fig. 5.6, and the resulting uncertainty regions for the same four measurement errors as in the previous section are shown in Fig. 5.7. All cases find a single solution at the true solution, with various uncertainty regions. The uncertainty region in the case with no measurement error is now bounded within 14 km in the x-direction and 1.5 km in the y-direction, with an area of 7.37 km^2. The area of the feasible region has been reduced by four orders of magnitude

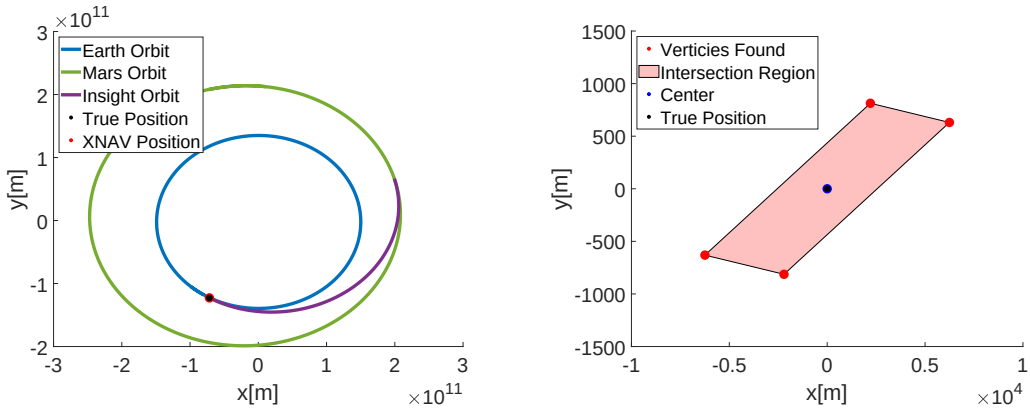

(a) (b)

Figure 5.6: Using 7 pulsars at TCM 1 (a)XNAV solutions in a domain covering the orbit of Mars along with relevant trajectories (b) The feasible region about the XNAV solution.

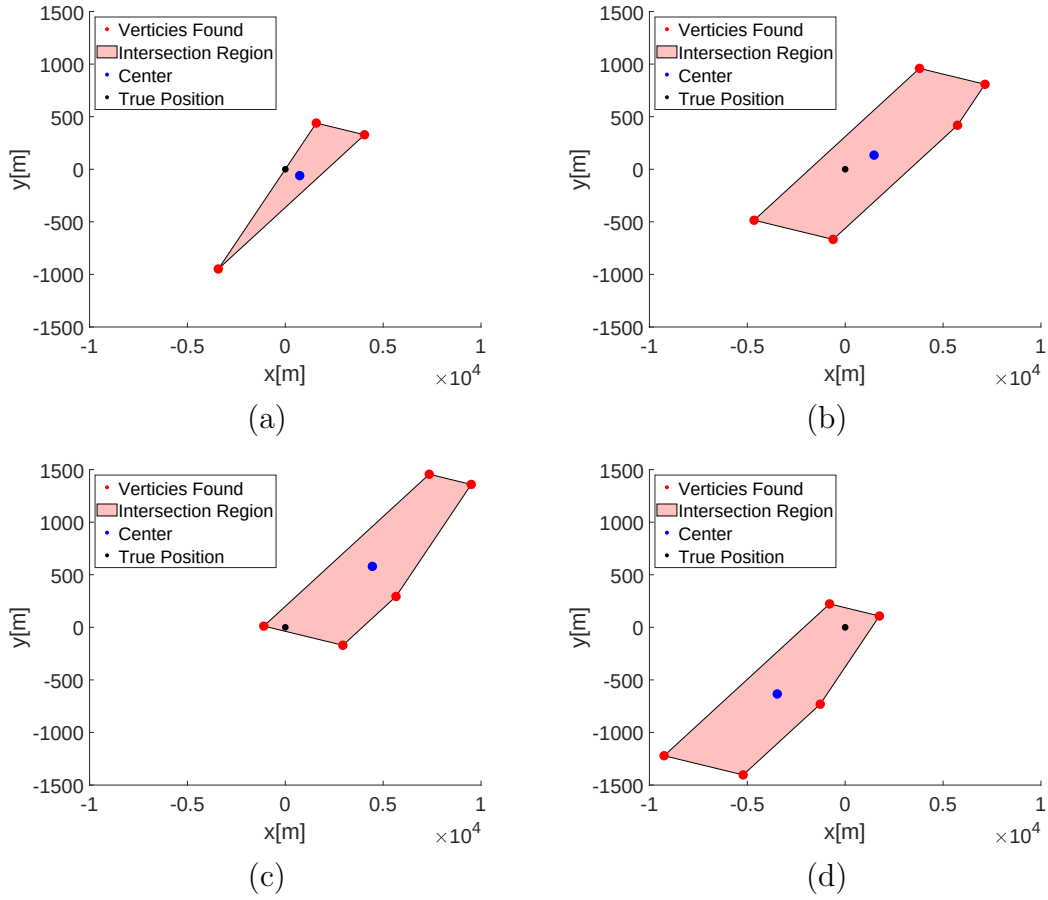

Figure 5.7: The feasible intersection region at TCM 1 for 7 pulsar measurements with random measurement error for four different random number generator seeds.

compared to the 5 pulsar case. In the 7 pulsar case also shows some cases where the number of vertices of the feasible region may increase or decrease.

5.2 Missions within Jupiter's Orbit

The same set of 7 pulsars may be used to determine a spacecraft's position for spacecraft operating within Jupiter's orbit. For the following example, NASA's Juno spacecraft trajectory is considered [145, 146], and the true position is the start of Juno's orbit insertion maneuver at Jupiter. Figure 5.8(a) shows the orbits of Earth and Jupiter, the trajectory of Juno, and the true and XNAV estimated positions, while Fig. 5.8(b) shows the feasible intersection region for the 7 pulsars, centered at the true position. For these 7 pulsars, there is a single solution at the true solution when no measurement error is applied, and since the pulsars selected are the same as the Mars case the area of the feasible region is 7.37 km^2.

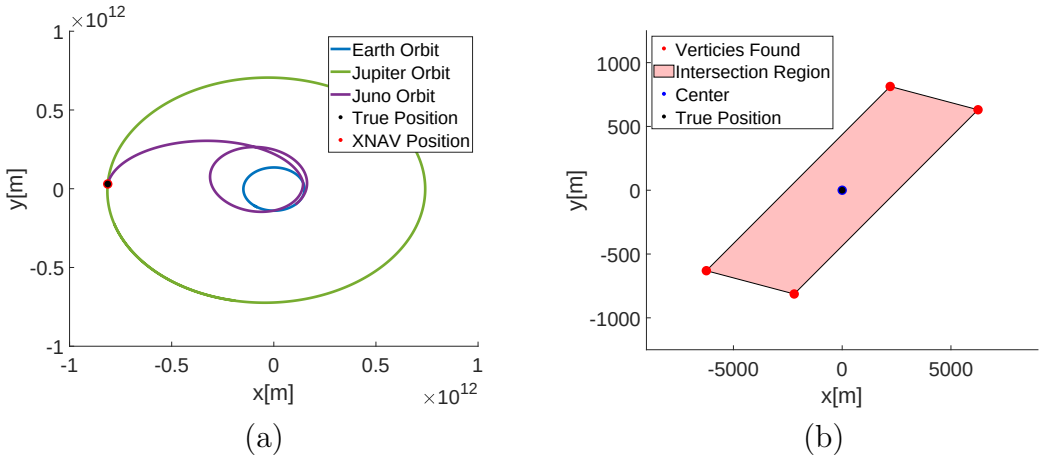

(a) (b)

Figure 5.8: Using 7 pulsars at orbit insertion for JUNO (a)XNAV solutions in a domain covering the orbit of Jupiter along with relevant trajectories (b) The feasible region about the XNAV solution.

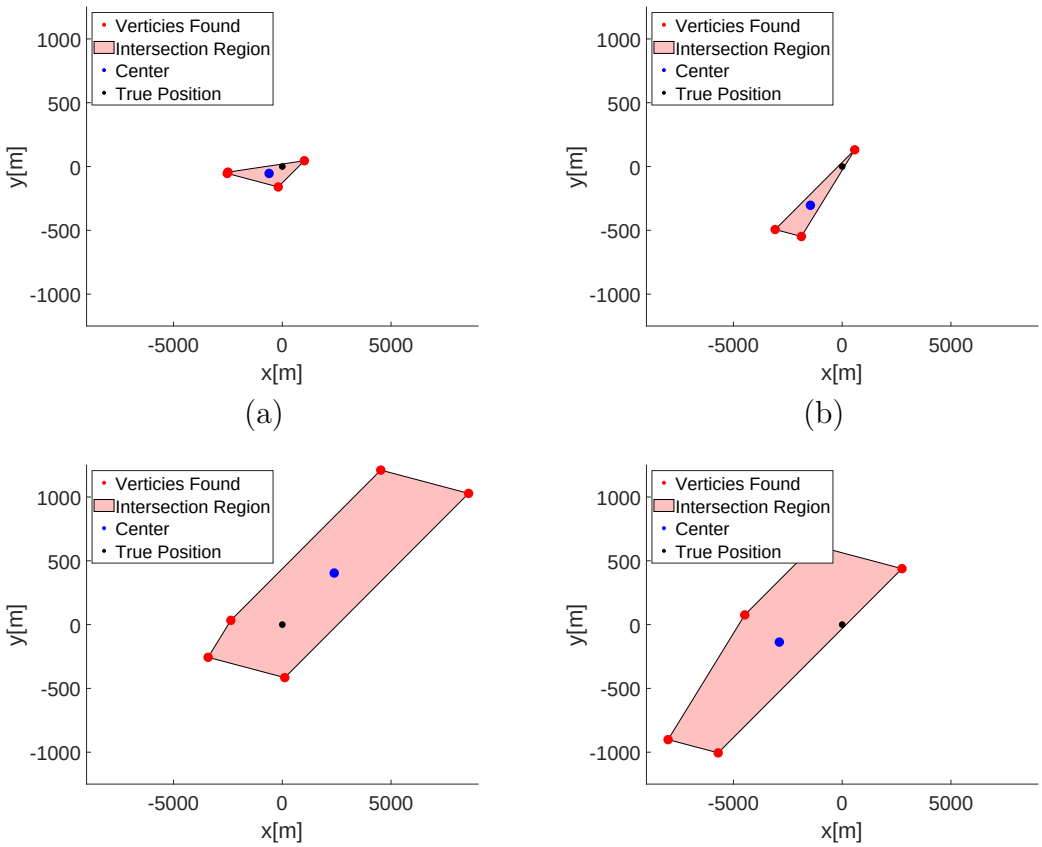

(a) (b) (c) (d)

Figure 5.9: The feasible intersection region at orbit insertion for 7 pulsar measurements with random measurement error for four different random number generator seeds.

The same random measurement error is applied as above and the resulting feasible regions is shown in Fig. 5.9. Once again the shape and area of the feasible region may change between all cases, but the true position is still contained within the feasible region. In all cases considered, a single candidate position was found within the orbit of Jupiter using only XNAV measurements.

5.3 Missions within Pluto's Orbit

An additional case may be considered for missions to the outer Solar System. The reference trajectory for this case will be NASA's New Horizons mission, and the domain size will be set to contain Pluto's orbit. For this case 8 pulsars are needed to be used to find a single solution, the combination of 5 pulsars which resulted in largest candidate spacing and the 3 which minimize the uncertainty in position. If 7 pulsars are used as in the Jupiter or Mars cases there are 2 or more solutions in a domain bounded by the orbit of Pluto. For an 8-pulsar-observation test case, the spacecraft is located at Pluto approach for New Horizons. Figure 5.10(a) shows Pluto's orbit, New Horizon's trajectory, the spacecraft's position and the XNAV estimated position while Fig. 5.10(b) shows the feasible intersection region for this case. Once again, a single solution for the spacecraft position is found for the case of no error, Fig. 5.10 or with random error, Fig. 5.11. The case with no measurement error bound the area of the feasible region to be less than 7.37 km^2, the addition of measurement error may reduce this area.

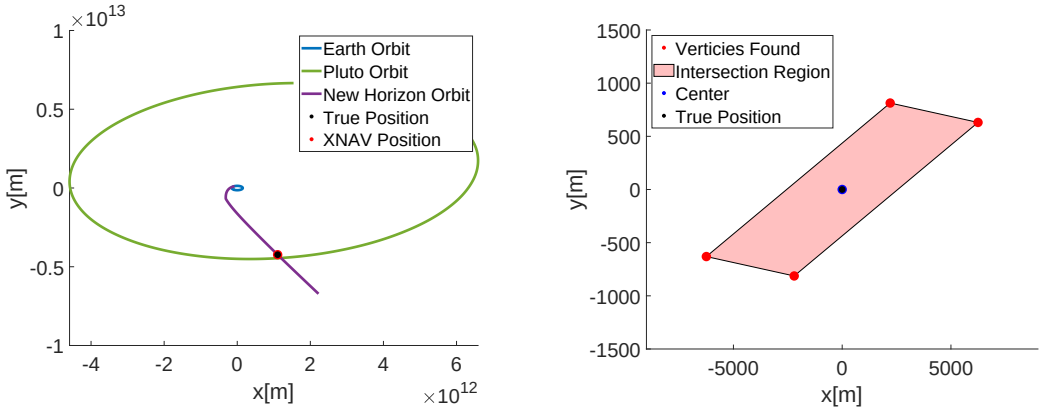

(a) (b)

Figure 5.10: Using 7 pulsars at Pluto approach for New Horizons (a) XNAV solutions in a domain covering the orbit of Pluto along with relevant trajectories (b) The feasible region about the XNAV solution.

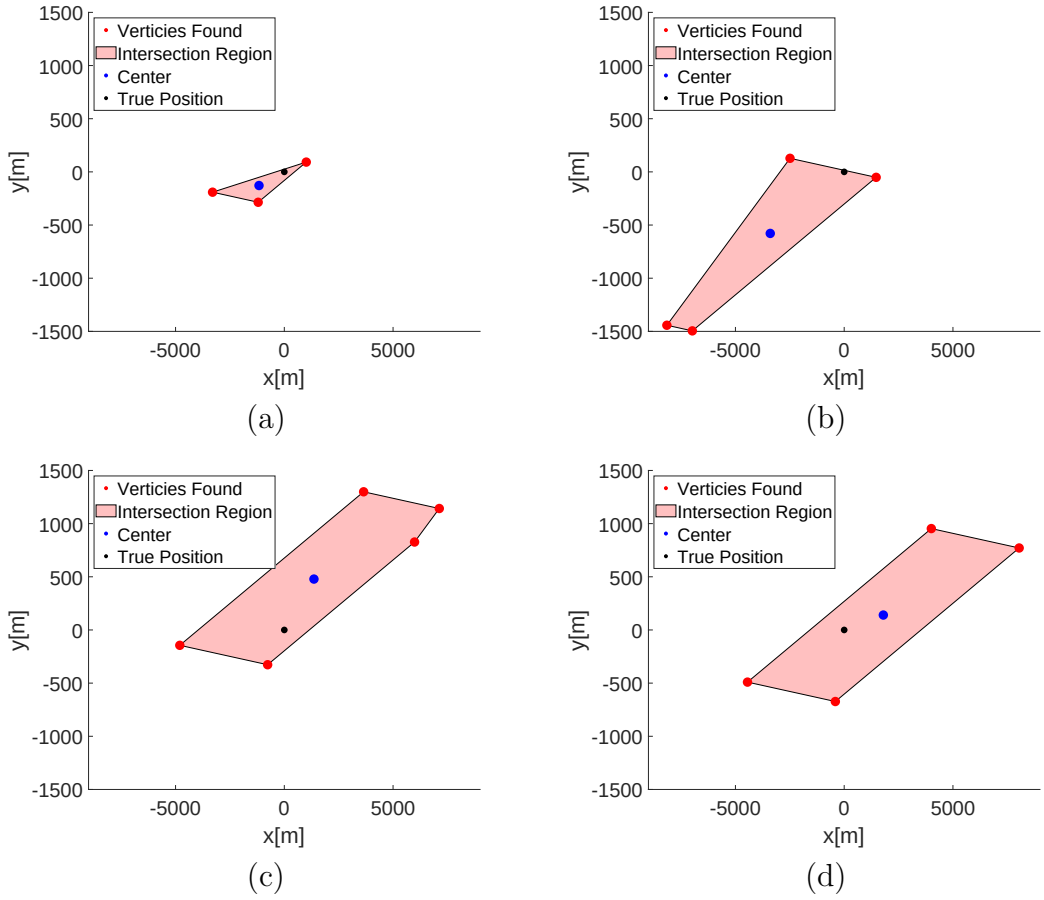

Figure 5.11: The feasible intersection region at orbit insertion for 7 pulsar measurements with random measurement error for four different random number generator seeds.

5.4 Summary

By selecting an appropriate set of pulsars, XNAV measurements may be used to unambiguously resolve spacecraft position within a bounded domain. Five pulsars must be observed to fully resolve position within the orbit of Mars, however this case is susceptible to measurement error and results in a large intersection region in which the position may not be further resolved without additional measurements. Six pulsars can be used to find a single solution, or the combinations of pulsars can be switched to select 4 which minimize the spacing between candidates and 3 to minimize the area of the feasible region. This 7-pulsar set results in a single solution with an area of 7.37 km^2 compared to an area of 8.7921×10^4 km^2 for the 5 pulsar case. Missions to Jupiter and Pluto are also considered and a single solution was found for both cases. For the Jupiter case, the same 7 pulsars were used and the area of the feasible region was once again bounded by 7.37 km^2. For the Pluto case, 8 pulsar observations are required to find a single spacecraft position. In terms of determining the spacecraft's position, all three cases have a similar performance, they all find a single solution whose feasible region is bounded by the same maximum area.

The difference between these cases is the required computation time to evaluate all possible candidate positions. Table 5.1 shows the computational resources and wall time required for evaluate all candidate positions. In these cases majority of the computation time is spent in evaluating the combination of the first three pulsar measurements, since only feasible candidate positions need to be evaluated for subsequent measurements. Increasing from 7 to 8 pulsar measurements will not significantly impact performance, but increasing the domain size by an order of magnitude will. Between the Insight and Juno cases, the number of pulsar observations was unchanged, and the area of the domain increased by a factor of 10.6, however the computation time increased by a factor of 16. In both of these cases, the total computation time is not significant compared to the time for a single pulsar observation, approximately one day. In the New Horizons case, the computation time increased by a factor of 16.36 compared to the Juno case even with the addition of 36 more computer cores. If the computation is run on a single computer core, the calculations would take approximately 160 hours, or 6.6 days. In this case it is important to begin the calculations

Table 5.1: Comparison of Case Studies

Case	Domain Size	Number of Observations	Computer Cores Used	Compute Time
Insight	5×10^{11} m	7 (or 5)	4	$\sim$ 55 s
Juno	6.3×10^{12} m	7	4	$\sim$ 880 s
New Horizons	3.3×10^{13} m	8	40	$\sim$ 14,400 s

as soon as the second pulsar observation is finished so that 6 days worth of computation may be preformed while the spacecraft is observing the 6 remaining pulsars, and less than one day of computation would remain at the end once all pulsar observations have been completed.

CHAPTER 6

CONCLUSIONS AND FUTURE WORK

6.1 Research Contributions

This dissertation presents a solution for determining candidate positions using XNAV measurements without prior state information. The contributions of this work are a comprehensive survey of XNAV technology, development of an efficient method for determining candidate states in a bounded domain, the development and assessment of measurement strategies for XNAV systems, and a method for state determination in a cold-start scenario using XNAV.

A comprehensive survey on XNAV technology was conducted which incorporates new advances in XNAV research from around the world. This work builds upon a more limited article published in 2005 by Sheikh et al. [38], which covered much of the early work in XNAV which was dominated by researchers in the United States of America. Since that time, research in XNAV has progressed and many more countries have contributed to the field. Advances in pulsar modeling, timing models, algorithms to estimate the pulsar phase, navigation filters, and hardware have made XNAV a more and more promising candidate for spacecraft navigation. Prior research has not addressed solving for a spacecraft's position in a cold-start scenario.

As a first step in solving the cold-start problem, a model for efficiently determining candidate states in a bounded domain using XNAV measurements is developed. An algorithm to determine which pulsar wavefronts to evaluate is presented to avoid iterating through all possible wavefronts combinations. Two error models are presented to determine if pulsar wavefronts intersect in two and three dimensions. One model defines the error as a ball about the intersection of two wavefronts, the other models the error as a banded region about each wavefront independently. For both models it is more efficient, in terms of observation time, to observe additional pulsars rather than improve the pulsar observation accuracy.

Using the banded error model, pulsar parameters were varied to determine which pulsars to measure in order to minimize the number of candidate solutions in a given domain. First, fictitious pulsars are considered to find guidelines for pulsar selection in an ideal scenario. It

was found that minimizing the angular separation between pulsar and increasing the period of the pulsars minimized the number of candidate solutions. In terms of accuracy, it is best to improve the accuracy of each measurement simultaneously rather than focusing on a single measurement. A set of real pulsars are then considered and combinations of 3, 4 and 5 pulsars are considered. The sets which minimize the number of candidates within the domain follow the same trends as with the fictitious pulsars.

Using proper pulsar selection, state determination using XNAV without any prior information is possible. Combinations of pulsars with sufficiently large candidate spacing may result in a single candidate position within the desired domain. The trajectories of NASA's Insight lander is considered for a Mars class mission, Juno for a Jupiter mission, and New Horizons for an outer Solar System mission. Using proper pulsar selection a single solution is found for all three cases for various measurement errors.

6.2 Future Work

The results presented in this dissertation have several areas which may be improved. The main areas identified are as follows:

6.2.1 Evaluation of combinations of 5 or more pulsars

Within this dissertation all combinations of 3 and 4 pulsars were evaluated in two dimensions to find which combinations produced the fewest solutions in a given domain. Results indicated that the combination which preformed best was one with small average angular separation and large average period, however there is no way to pick this combination out based purely on the average characteristics. One hundred combinations of pulsars were considered and evaluated in attempt to capture the solution which may perform best, but there is no guarantee that this happened. An full evaluation of combinations of 5 pulsars should be preformed to determine which combination performs best. The same procedure may be repeated for all combinations of 6 pulsars as well. These analyses are very computationally expensive; however, the computation does not need to be performed on the spacecraft, rather they may be performed prior to launch.

6.2.2 Evaluation of pulsar combination sensitivity to error

The analysis to determine which pulsar combination resulted in the fewest number of candidate solutions within a domain was done by by evaluating all combinations on a small domain, removing combinations which resulted in more than one candidate position, then increasing the domain and repeating the process. This method removes combinations when a single additional candidate solutions is found, it does not consider that some combinations of pulsars may result in clusters of candidate solutions near one another. Combinations like these may result in position ambiguity when error is introduced into the measurement. Pulsar combinations should then be evaluated to determine their sensitivity to error to more accurately determine the maximum domain size which can be used to position determination.

6.2.3 Evaluation of pulsar combinations in three dimensions

A majority of the results in this dissertation were presented in two dimensions for simplicity. Examples were given in three dimensions to show feasibility, but a full study was not conducted. The domain should be expanded to three dimensions to more accurately capture a realistic scenario. When expanding to three dimensions, the domain does not need to be a cube as bodies within the Solar System do not have a large inclination. However with the expansion to three dimensions, sets of pulsars to consider may change and analysis must be preformed again to determine which set to consider. Furthermore the number of pulsars required to determine position without any ambiguity will increase compared to two dimensions.

6.2.4 Improvements in the efficiency of candidate position determination algorithms

In order to determine a spacecraft's candidate position, a spacecraft would need to calculate all intersections for all pulsar measurements onboard. This may result in millions of candidates being checked since the computation time is proportional to the area of the domain. For deep space applications, where XNAV becomes a more attractive method of navigation, this becomes an increasingly important issue. When the problem is extended to three dimensions this computation time will only increase. Some time may be saved since the computations may begin once two measurements are completed for a 2D case, or three in a 3D case; however, depending on the computational resources it may require days in order to evaluate all potential positions.

REFERENCES

[1] S. I. Sheikh, D. J. Pines, P. S. Ray, K. S. Wood, M. N. Lovellette, and M. T. Wolff, "Spacecraft Navigation Using X-Ray Pulsars," *Journal of Guidance, Control, and Dynamics*, vol. 29, no. 1, pp. 49–63, 2006. [Online]. Available: http://arc.aiaa.org/doi/10.2514/1.13331

[2] K. S. Wood and P. S. Ray, "The NRL progam in X-ray navigation," in *593. WE-Heraeus Seminar on Autonomous Spacecraft Navigation*, 2015.

[3] J. H. Taylor, R. N. Manchester, and A. G. Lyne, "Catalog of 558 Pulsars," *The Astrophysical Journal Suplement Series*, vol. 88, pp. 529–568, 1993. [Online]. Available: http://adsabs.harvard.edu/doi/10.1086/191832

[4] L. A. Rawley, J. H. Taylor, M. M. Davis, and D. W. Allan, "Millisecond Pulsar PSR 1937+21: A Highly Stable Clock," *Science*, vol. 238, no. 4828, pp. 761–766, 1987.

[5] D. C. Backer and R. W. Hellings, "Pulsar Timing and General Relativity," *Annual Review of Astronomy and Astrophysics*, vol. 24, no. 1, pp. 537–575, 1986. [Online]. Available: http://www.annualreviews.org/doi/10.1146/annurev.aa.24.090186.002541

[6] G. S. Downs, "JPL Pulsar Timing Observations. I. The Vela Pulsar," *The Astrophysical Journal*, vol. 249, pp. 687–697, 1981.

[7] A. Lyne, G. Hobbs, M. Kramer, I. Stairs, and B. Stappers, "Switched Magnetospheric Regulation of Pulsar Spin-Down," *Science*, vol. 329, no. 5990, pp. 408–413, 2010.

[8] W. Becker, *Neutron Stars and Pulsars*. Springer, 2009. [Online]. Available: http://imagine.gsfc.nasa.gov/docs/science/know_l1/pulsars.html

[9] P. S. Ray, K. S. Wood, and M. T. Wolff, "Characterization of Pulsar Sources for X-ray Navigation," in *Proceedings ofthe 593. WE-Heraeus Seminar on Autonomous Spacecraft Navigation*, 2018. [Online]. Available: http://arxiv.org/abs/1711.08507

[10] A. A. Emadzadeh and J. L. Speyer, *Navigation in space by X-ray pulsars*, 2011.

[11] A. R. Golshan and S. I. Sheikh, "On pulse phase estimation and tracking of variable celestial X-ray sources," in *Institute of Navigation 63rd Annual Meeting*, 2007, pp. 413–422.

[12] J. Liu, J. Ma, and J. Tian, "Pulsar/CNS integrated navigation based on federated UKF," *Journal of Systems Engineering and Electronics*, vol. 21, no. 4, pp. 675–681, 2010.

[13] John Eric Hanson, "Principles of X-ray Navigation," Ph.D. dissertation, Stanford University, 1996.

[14] X. Zhang, P. Shuai, L. Huang, S. Chen, and L. Xu, "Mission Overview and Initial Observation Results of the X-Ray Pulsar Navigation-I Satellite," *International Journal of Aerospace Engineering*, vol. 2017, 2017.

[15] Z. Arzoumanian, K. C. Gendreau, C. L. Baker, T. Cazeau, P. Hestnes, J. W. Kellogg, S. J. Kenyon, R. P. Kozon, K.-C. Liu, S. S. Manthripragada, C. B. Markwardt, A. L. Mitchell, J. W. Mitchell, C. A. Monroe, T. Okajima, S. E. Pollard, D. F. Powers, B. J. Savadkin, L. B. Winternitz, P. T. Chen, M. R. Wright, R. Foster, G. Prigozhin, R. Remillard, and J. Doty, "The neutron star interior composition explorer (NICER): mission definition," in *Astronomical Telescopes and Instrumentation*, vol. 9144, 2014. [Online]. Available: http://proceedings.spiedigitallibrary.org/proceeding.aspx?doi=10.1117/12.2056811

[16] W. Baade and F. Zwicky, "On Super-Novae," *Proceedings of the National Academy of Sciences*, vol. 20, no. 5, pp. 254–259, 1934. [Online]. Available: http://www.pnas.org/lookup/doi/10.1073/pnas.20.5.254

[17] W. Baade and F. Zwicky, "Cosmic Rays From Super-Novae," *Handbuch d. Astrophysik*, vol. 20, no. 5, pp. 259–263, 1934.

[18] J. R. Oppenheimer and G. M. Volkoff, "On massive neutron cores," *Physical Review*, vol. 55, no. 4, pp. 374–381, 1939.

[19] T. J.-L. Courvosier, *High Energy Astrophysics*. Springer, 2009.

[20] L. L. Smarr and R. Blandford, "The Binary Pulsar: Physical Processes and Possible Companions, and Evolutionary Histories," *The Astrophusical Journal*, vol. 207, pp. 574–588, 1976.

[21] K. S. Wood, J. R. Determan, P. S. Ray, M. T. Wolff, S. A. Budzien, M. N. Lovellette, and L. Titarchuk, "Using the Unconventional Stellar Aspect (USA) experiment on ARGOS to determine atmospheric parameters by X-ray occultation," in *Optical Spectroscopic Techniques, Remote Sensing, and Instrumentation for Atmospheric and Space Research IV*, vol. 4485, 2002, pp. 258–265.

[22] D. J. Champion, G. B. Hobbs, R. N. Manchester, R. T. Edwards, D. C. Backer, M. Bailes, W. Coles, P. B. Demorest, R. D. Ferdman, W. M. Folkner, A. W. Hotan, A. N. Lommen, D. J. Nice, M. B. Purver, J. M. Sarkissian, I. H. Stairs, W. V. Straten, W. Verbiest, and D. R. B. Yardley, "Measuring the mass of solar system planets using pulsar timing," *The Astrophysical Journal Letters*, vol. 720, p. L201, 2010.

[23] W. Becker, M. Kramer, and A. Sesana, "Pulsar Timing and Its Application for Navigation and Gravitational Wave Detection," *Space Science Reviews*, 2018. [Online]. Available: http://dx.doi.org/10.1007/s11214-017-0459-0

[24] P. Reichley, G. Downs, and G. Morris, "Use of Pulsar Signals As Clocks," Tech. Rep. 2, 1971.

[25] G. S. Downs, "Interrplanetary Naviqation Using Pulsating Radio Sources," Tech. Rep., 1974.

[26] K. Wallace, "Radio Stars , What They are and The Prospects for their Use in Navigational Systems," *Journal of Navigation*, vol. 41, pp. 358–371, 1988.

[27] T. J. Chester and S. A. Butman, "Navigation Using X-ray Pulsars," 1981.

[28] J. W. Mitchell, L. B. Winternitz, M. A. Hassouneh, S. R. Price, S. R. Semper, W. H. Yu, P. S. Ray, M. T. Wolff, M. Kerr, K. S. Wood, Z. Arzoumanian, K. C. Gendreau, and P. Demorest, "Sextant X-Ray Pulsar Navigation Demonstration: Initial On-Orbit Results," in *AIAA Guidance and Contorl Conference*, Breckenridge, Colorado, 2018.

[29] L. M. B. Winternitz, J. W. Mitchell, M. A. Hassouneh, S. R. Price, S. R. Semper, W. H. Yu, P. S. Ray, M. T. Wolff, M. Kerr, K. S. Wood, Z. Arzoumanian, K. C. Gendreau, L. Guillemot, P. Demorest, B. Stappers, and A. Lyne, "SEXTANT X-ray Pulsar Navigation Demonstration: Additional On-Orbit Results," in *15th International Conference on Space Operations*, 2018.

[30] S. Shemar, G. Fraser, L. Heil, D. Hindley, A. Martindale, P. Molyneux, J. Pye, R. Warwick, and A. Lamb, "Towards practical autonomous deep-space navigation using X-Ray pulsar timing," *Experimental Astronomy*, vol. 42, no. 2, pp. 101–138, 2016.

[31] K. D. Anderson, D. J. Pines, and S. I. Sheikh, "Validation of Pulsar Phase Tracking for Spacecraft Navigation," *Journal of Guidance, Control, and Dynamics*, vol. 38, no. 10, pp. 1885–1897, 2015. [Online]. Available: http://arc.aiaa.org/doi/10.2514/1.G000789

[32] D. W. Woodfork, "The Use of X-Ray Pulsar for Aiding GPS Satellite Orbit Determination," Ph.D. dissertation, Air Force Institute of Technology, 2005.

[33] X. Kai, W. Chunling, and L. Liangdong, "The use of X-ray pulsars for aiding navigation of satellites in constellations," *Acta Astronautica*, vol. 64, no. 4, pp. 427–436, 2009.

[34] N. James, R. Abello, M. Lanucara, M. Mercolino, and R. Maddè, "Implementation of an ESA delta-DOR capability," *Acta Astronautica*, vol. 64, no. 11-12, pp. 1041–1049, 2009.

[35] P. Graven, J. Collins, S. Sheikh, J. Hanson, P. Ray, and K. Wood, "Xnav for Deep Space Navigation," in *31st Annual Guidance and Control Conference*, 2008, pp. 349–364.

[36] S. R. Steffes, G. H. Barton, S. A. Bhatt, M. P. Fritz, E. T. King, and D. C. Woffinden, "Deep Space Autonomous Navigation Options for Future NASA Crewed Missions," 2018, pp. 505–523.

[37] P. S. Ray, K. S. Wood, and B. F. Phlips, "Spacecraft Navigation Using X-Ray Pulsars," Tech. Rep., 2006. [Online]. Available: http://arc.aiaa.org/doi/10.2514/1.13331

[38] S. I. Sheikh, J. E. Hanson, P. H. Graven, and D. J. Pines, "Spacecraft Navigation and Timing Using X-ray Pulsars," *Navigation: Journal of the Institute ofNavigation*, vol. 58, no. 2, pp. 165–186, 2011.

[39] J. Sala, A. Urruela, X. Villares, R. Estalella, and J. M. Paredes, "Feasibility study for a spacecraft navigation system relying on pulsar timing information," European Space Agency, Tech. Rep., 2004.

[40] S. I. Sheikh, "The use of Variable Celestial X-Ray Sources for Spacecraft Navigation," Ph.D. dissertation, 2005. [Online]. Available: http://drum.lib.umd.edu/handle/1903/9139

[41] S. I. Sheikh and D. J. Pines, "Recursive estimation of spacecraft position and velocity using X-ray pulsar time of arrival measurements," *Navigation, Journal of the Institute of Navigation*, vol. 53, no. 3, pp. 149–166, 2006.

[42] S. I. Sheikh, A. R. Golshan, and D. J. Pines, "Absolute and relative position determination using variable celestial X-ray sources," in *30th Annual AAS Guidance and Control Conference*, 2007, pp. 855–874.

[43] K. D. Anderson and D. Pines, "Experimental Validation of Pulse Phase Tracking for X-ray Pulsar Based Spacecraft Navigation," *AIAA Guidance, Navigation, and Control (GNC) Conference*, 2013. [Online]. Available: http://arc.aiaa.org/doi/10.2514/6.2013-5202

[44] A. Hewish, S. J. Bell, J. D. H. Pilkington, P. F. Scott, and R. A. Collins, "Observation of a Rapidly Pulsating Radio Source," *Nature*, vol. 217, pp. 709–713, 1968.

[45] C. Thompson and R. C. Duncan, "The Soft Gamma Repeaters as Very Strongly Magnetized Neutron Stars. II. Quiescent Neutrino, X-Ray and Alfven Emission," *The Astrophysical Journal*, vol. 473, no. 1, pp. 322–342, 1996.

[46] E. P. J. van den Hueval and S. A. Rappaport, *X-Ray Binaries and Recycled Pulsars*. Springer, 1992.

[47] A. Papitto, C. Ferrigno, E. Bozzo, N. Rea, L. Pavan, L. Burderi, M. Burgay, S. Campana, T. Di Salvo, M. Falanga, M. D. Filipović, P. C. Freire, J. W. Hessels, A. Possenti, S. M. Ransom, A. Riggio, P. Romano, J. M. Sarkissian, I. H. Stairs, L. Stella, D. F. Torres, M. H. Wieringa, and G. F. Wong, "Swings between rotation and accretion power in a binary millisecond pulsar," *Nature*, vol. 501, no. 7468, pp. 517–520, 2013.

[48] D. C. Backer, S. R. Kulkarni, C. Heiles, M. M. Davis, and W. M. Goss, "A Millisecond Pulsar," *Letters to Nature*, vol. 300, pp. 615–618, 1982.

[49] L. R. Cominsky and K. S. Wood, "Discovery of a 7.1 Hour Period and Eclipses from MXB 1959-29," *The Astrophysical Journal*, vol. 283, pp. 765–773, 1984.

[50] L. R. Cominsky and K. S. Wood, "Further Observations of the Eclipsing X-Ray Burst Source MXB 1969-29," *The Astrophysical Journal*, vol. 337, pp. 485–493, 1989.

[51] W. Becker and J. Trümper, "Detection of pulsed X-rays from the binary millisecond pulsar J0437 - 4715," *Nature*, vol. 365, no. 6446, pp. 528–530, 1993.

[52] H. Inoue, "The X-Ray Astronomy SAtellite "ASCA"," *Experimental Astronomy*, vol. 4, no. 1, pp. 1–10, 1993.

[53] Y. Tsusaka, H. Suzuki, K. Yamashita, H. Kunieda, Y. Tawara, Y. Ogasaka, Y. Uchibori, H. Honda, M. Itoh, H. Awaki, H. Tsunemi, K. Hayashida, S. Nomoto, M. Wada, E. Miyata, P. J. Serlemitsos, L. Jalota, and Y. Soong, "Characterization of the Advanced Satellite for Cosmology and Astrophysics x-ray telescope: preflight calibration and ray tracing." *Applied optics*, vol. 34, no. 22, pp. 4848–4856, 1995. [Online]. Available: http://www.ncbi.nlm.nih.gov/pubmed/21052325

[54] K. Jahoda, J. H. Swank, A. B. Giles, M. J. Stark, T. Strohmayer, W. W. Zhang, and E. H. Morgan, "In-orbit performance and calibration of the Rossi X-ray Timing Explorer (RXTE) Proportional Counter Array (PCA)," in *International Symposium on Optical Science*, 1996. [Online]. Available: http://proceedings.spiedigitallibrary.org/proceeding.aspx?articleid=1021016 pp. 59–70.

[55] W. Becker and J. Trumper, "The X-ray luminosity of rotation-powered neutron stars," *Astronomy and Astrophysics*, vol. 326, 1997.

[56] R. Wijnands and M. Van Der Klis, "A millisecond pulsar in an X-ray binary system," *Nature*, vol. 394, pp. 344–346, 1998.

[57] W. Becker and J. Trümper, "The X-ray emission properties of millisecond pulsars," *Astronomy and Astrophysics*, vol. 341, pp. 803–817, 1999. [Online]. Available: http://arxiv.org/abs/astro-ph/9806381

[58] W. Voges, B. Aschenbach, T. Boller, H. Braeuninger, U. Briel, W. Burkert, K. Dennerl, J. Englhauser, R. Gruber, F. Haberl, G. Hartner, G. Hasinger, E. Pfeffermann, W. Pietsch, P. Predehl, C. Rosso, J. H. M. M. Schmitt, J. Truemper, and H.-U. Zimmermann, "The ROSAT All-Sky Survey Bright Source Catalogue," *Astronomy Letters*, vol. 349, 1999. [Online]. Available: http://arxiv.org/abs/astro-ph/9909315

[59] R. N. Manchester, A. G. Lyne, F. Camilo, J. F. Bell, V. M. Kaspi, N. D'Amico, N. P. McKay, F. Crawford, I. H. Stairs, A. Possenti, M. Kramer, and D. C. Sheppard, "The Parkes Multi-Beam Pulsar Survey: I. Observing and Data Analysis Systems, Discovery and Timing of 100 Pulsars," *Monthly Notices of the Royal Astronomical Society*, vol. 328, no. 1, pp. 17–35, 2001.

[60] D. K. Galloway, D. Chakrabarty, E. H. Morgan, and R. A. Remillard, "Discovery of a High-Latitude Accreting Millisecond Pulsar in an Ultracompact Binary," *The Astrophysical Journal*, vol. 576, pp. L137–L140, 2002. [Online]. Available: http://stacks.iop.org/1538-4357/576/i=2/a=L137

[61] A. Possenti, R. Cerutti, M. Colpi, and S. Merghetti, "Re-examining the X-ray versus spin-down luminosity correlation of rotation powered pulsars," *Astronomy and Astrophysics*, vol. 387, pp. 993–1002, 2002.

[62] C. B. Markwardt, J. H. Swank, T. E. Strohmayer, J. J. M. i. t. Zand, and F. E. Marshall, "Discovery of a Second Millisecond Accreting Pulsar: XTE J1751305," *The Astrophysical Journal*, vol. 575, pp. L21–L24, 2002. [Online]. Available: http://stacks.iop.org/1538-4357/575/i=1/a=L21

[63] L. Nicastro, G. Cusumano, O. Loehmer, M. Kramer, L. Kuiper, W. Hermsen, T. Mineo, and W. Becker, "BeppoSAX observation of PSR B1937+21," *Astronomy and Astrophysics*, vol. 413, 2004. [Online]. Available: http://arxiv.org/abs/astro-ph/0310299

[64] M. G. F. Kirsch, K. Mukerjee, M. G. Breitfellner, S. Djavidnia, M. J. Freyberg, E. Kendziorra, and M. J. S. Smith, "Studies of orbital parameters and pulse profile of the accreting millisecond pulsar XTE J1807–294," *Astronomy & Astrophysics*, vol. 423, pp. L9–L12, 2004. [Online]. Available: http://www.aanda.org/10.1051/0004-6361:200400022

[65] A. H. Rots, K. Jahoda, and A. G. Lyne, "ABSOLUTE TIMING OF THE CRAB PULSAR WITH THE ROSSI X-RAY TIMING EXPLORER Arnold H. Rots," *The astrophysical Journal*, vol. 605, pp. L129–L132, 2004.

[66] T. Boller, M. J. Freyberg, J. Truemper, F. Haberl, W. Voges, and K. Nandra, "Second ROSAT all-sky survey (2RXS) source catalogue," *Astronomy and Astrophysics*, vol. 103, 2016. [Online]. Available: http://arxiv.org/abs/1609.09244%0Ahttp://dx.doi.org/10.1051/0004-6361/201525648

[67] J. Yang, S. G. T. Laycock, D. M. Christodoulou, S. Fingerman, M. J. Coe, and J. J. Drake, "A Comprehensive Library of X-ray Pulsars in the Small Magellanic Cloud: Time Evolution of their Luminosities and Spin Periods," *The Astrophysical Journal*, vol. 839, no. 2, p. 119, 2017. [Online]. Available: http://arxiv.org/abs/1703.05196

[68] G. Fritz, R. C. Henry, J. F. Meekins, T. A. Chubb, and H. Friedman, "X-ray pulsar in the Crab Nebula," *Science*, vol. 164, no. 3880, pp. 709–712, 1969.

[69] D. Chakrabarty and E. H. Morgan, "The two-hour orbit of a binary millisecond X-ray pulsar," *Nature*, vol. 394, pp. 346–348, 1998. [Online]. Available: http://adsabs.harvard.edu/abs/1998Natur.394..346C

[70] M. C. Weisskopf, H. D. Tanabaum, L. P. V. Speybroeck, and S. L. Dell, "Chandra X-Ray Obsevatory (CXO): Overview," in *Proceedings of SPIE*, 2000.

[71] M. Kowalski, D. Wood, G. Fritz, G. Fewtrell, M. Lovellette, D. Yentis, K. Wood, M. Wolff, P. Ray, and R. Bandyopadhyay, "The unconventional stellar aspect (USA) experiment on ARGOS," in *AIAA Space 2001 Conference and Exposition*, 2001. [Online]. Available: http://arc.aiaa.org/doi/10.2514/6.2001-4664

[72] K. S. Wood, G. Fritz, P. Hertz, W. N. Johnson, M. N. Lovelette, M. T. Wolff, E. Bloom, G. Godfrey, J. Hanson, P. Michelson, R. Taylor, and H. Wen, "The USA experiment on the Argos Satellite: A low cost instrument for timing x-ray binaries," *AIP Conference Proceedings*, vol. 308, no. 561, 1994. [Online]. Available: http://aip.scitation.org/doi/abs/10.1063/1.45941

[73] K. S. Wood, "Navigation Studies Utilizing the NRL-801 Experiment and the ARGOS Satellite," in *Society of Photo-Optical Instrumentation Engineers Proceedings*, 1993. [Online]. Available: http://proceedings.spiedigitallibrary.org/proceeding.aspx?articleid=1011383 pp. 105–116.

[74] P. S. Ray, K. S. Wood, G. Fritz, P. Hertz, M. Kowalski, W. N. Johnson, M. N. Lovellette, M. T. Wolff, D. Yentis, R. M. Bandyopadhyay, E. D. Bloom, B. Giebels, G. Godfrey, K. Reilly, P. S. Parkinson, G. Shabad, P. Michelson, M. Roberts, D. A. Leahy, L. Cominsky, J. Scargle, J. Beall, D. Chakrabarty, and Y. Kim, "The USA X-ray Timing Experiment," in *X-Ray Astronomy*, 1999. [Online]. Available: http://arxiv.org/abs/astro-ph/9911236

[75] R. N. Manchester, G. B. Hobbs, A. Teoh, and M. Hobbs, "The ATNF Pulsar Catalogue," *The Astronomical Journal*, vol. 129, pp. 1993–2006, 2005. [Online]. Available: http://arxiv.org/abs/astro-ph/0412641%0Ahttp://dx.doi.org/10.1086/428488

[76] M. Feroci, L. Stella, M. van der Klis, T. J. L. Courvoisier, M. Hernanz, R. Hudec, A. Santangelo, D. Walton, A. Zdziarski, D. Barret, T. Belloni, J. Braga, S. Brandt, C. Budtz-Jørgensen, S. Campana, J. W. den Herder, J. Huovelin, G. L. Israel, M. Pohl, P. Ray, A. Vacchi, S. Zane, A. Argan, P. Attinà, G. Bertuccio, E. Bozzo, R. Campana, D. Chakrabarty, E. Costa, A. De Rosa, E. Del Monte, S. Di Cosimo, I. Donnarumma, Y. Evangelista, D. Haas, P. Jonker, S. Korpela, C. Labanti, P. Malcovati, R. Mignani, F. Muleri, M. Rapisarda, A. Rashevsky, N. Rea, A. Rubini, C. Tenzer, C. Wilson-Hodge, B. Winter, K. Wood, G. Zampa, N. Zampa, M. A. Abramowicz, M. A. Alpar, D. Altamirano, J. M. Alvarez, L. Amati, C. Amoros, L. A. Antonelli, R. Artigue, P. Azzarello, M. Bachetti, G. Baldazzi, M. Barbera, C. Barbieri, S. Basa, A. Baykal, R. Belmont, L. Boirin, V. Bonvicini, L. Burderi, M. Bursa, C. Cabanac, E. Cackett, G. A. Caliandro, P. Casella, S. Chaty, J. Chenevez, M. J. Coe, A. Collura, A. Corongiu, S. Covino, G. Cusumano, F. D'Amico, S. Dall'Osso, D. De Martino, G. De Paris, G. Di Persio, T. Di Salvo, C. Done, M. Dovčiak, A. Drago, U. Ertan, S. Fabiani, M. Falanga, R. Fender, P. Ferrando, D. Della Monica Ferreira, G. Fraser, F. Frontera, F. Fuschino, J. L. Galvez, P. Gandhi, P. Giommi, O. Godet, E. Göğüş, A. Goldwurm, D. Götz, M. Grassi, P. Guttridge, P. Hakala, G. Henri, W. Hermsen, J. Horak, A. Hornstrup, J. J. M. in't Zand, J. Isern, E. Kalemci, G. Kanbach, V. Karas, D. Kataria, T. Kennedy, D. Klochkov, W. Kluźniak, K. Kokkotas, I. Kreykenbohm, J. Krolik, L. Kuiper, I. Kuvvetli, N. Kylafis, J. M. Lattimer, F. Lazzarotto, D. Leahy, F. Lebrun, D. Lin, N. Lund, T. Maccarone, J. Malzac, M. Marisaldi, A. Martindale, M. Mastropietro, J. McClintock, I. McHardy, M. Mendez, S. Mereghetti, M. C. Miller, T. Mineo, E. Morelli, S. Morsink, C. Motch, S. Motta, T. Muñoz-Darias, G. Naletto, V. Neustroev, J. Nevalainen, J. F. Olive, M. Orio, M. Orlandini, P. Orleanski, F. Ozel, L. Pacciani, S. Paltani, I. Papadakis, A. Papitto, A. Patruno, A. Pellizzoni, V. Petráček, J. Petri, P. O. Petrucci, B. Phlips, L. Picolli, A. Possenti, D. Psaltis, D. Rambaud, P. Reig, R. Remillard, J. Rodriguez, P. Romano, M. Romanova, T. Schanz, C. Schmid, A. Segreto, A. Shearer, A. Smith, P. J. Smith, P. Soffitta, N. Stergioulas, M. Stolarski, Z. Stuchlik, A. Tiengo, D. Torres, G. Török, R. Turolla, P. Uttley, S. Vaughan, S. Vercellone, R. Waters, A. Watts, R. Wawrzaszek, N. Webb, J. Wilms, L. Zampieri, A. Zezas, and J. Ziolkowski, "The Large Observatory for X-ray Timing (LOFT)," *Experimental Astronomy*, vol. 34, no. 2, pp. 415–444, 2012. [Online]. Available: http://link.springer.com/10.1007/s10686-011-9237-2

[77] S. Zane, D. Walton, T. Kennedy, M. Feroci, J.-W. Den Herder, M. Ahangarianabhari, A. Argan, P. Azzarello, G. Baldazzi, M. Barbera, D. Barret, G. Bertuccio, P. Bodin, E. Bozzo, L. Bradley, F. Cadoux, P. Cais, R. Campana, J. Coker, A. Cros, E. Del Monte, A. De Rosa, S. Di Cosimo, I. Donnarumma, Y. Evangelista, Y. Favre, C. Feldman, G. Fraser, F. Fuschino, M. Grassi, M. R. Hailey, R. Hudec, C. Labanti, P. Malcovati, D. Macera, M. Marisaldi, A. Martindale, T. Mineo, F. Muleri, M. Nowak, M. Orlandini, L. Pacciani, E. Perinati, V. Petracek, M. Pohl, A. Rachevski, P. Smith, A. Santangelo, J.-Y. Seyler, C. Schmid, P. Soffitta, S. Suchy, C. Tenzer, P. Uttley, A. Vacchi, G. Zampa, N. Zampa, J. Wilms, and B. Winter, "The large area detector of LOFT: the Large Observatory for X-ray Timing," in *Proc. SPIE 9144, Space Telescopes and Instrumentation 2014: Ultraviolet to Gamma Ray*, 2014. [Online]. Available: http://proceedings.spiedigitallibrary.org/proceeding.aspx?doi=10.1117/12.2054654

[78] V. M. Kaspi, J. H. Taylor, and M. F. Ryba, "High-Precision Timing of Millisecond Pulsars. III. Long-Term Monitoring of PSRs B1885+09 and B1937+21," *The Astrophysical Journal*, vol. 428, pp. 713–728, 1994.

[79] G. Desvignes, R. N. Caballero, L. Lentati, J. P. Verbiest, D. J. Champion, B. W. Stappers, G. H. Janssen, P. Lazarus, S. Osłowski, S. Babak, C. G. Bassa, P. Brem, M. Burgay, I. Cognard, J. R. Gair, E. Graikou, L. Guillemot, J. W. Hessels, A. Jessner, C. Jordan, R. Karuppusamy, M. Kramer, A. Lassus, K. Lazaridis, K. J. Lee, K. Liu, A. G. Lyne, J. McKee, C. M. Mingarelli, D. Perrodin, A. Petiteau, A. Possenti, M. B. Purver, P. A. Rosado, S. Sanidas, A. Sesana, G. Shaifullah, R. Smits, S. R. Taylor, G. Theureau, C. Tiburzi, R. Van Haasteren, and A. Vecchio, "High-precision timing of 42 millisecond pulsars with the European Pulsar Timing Array," *Monthly Notices of the Royal Astronomical Society*, vol. 458, pp. 3341–3380, 2016.

[80] I. Congrad and D. C. Backer, "A MICROGLITCH IN THE MILLISECOND PULSAR PSR B1821-24 IN M28," *The Astrophysical Jounral*, vol. 612, no. 2, pp. L125–L127, 2004.

[81] C. M. Espinoza, A. G. Lyne, B. W. Stappers, and M. Kramer, "A study of 315 glitches in the rotation of 102 pulsars," *Monthly Notices of the Royal Astronomical Society*, vol. 414, no. 2, pp. 1679–1704, 2011.

[82] G. Hobbs, A. G. Lyne, and M. Kramer, "An analysis of the timing irregularities for 366 pulsars," *Monthly Notices of the Royal Astronomical Society*, vol. 369, pp. 655–672, 2018.

[83] D. R. Stinebring, M. F. Ryba, J. H. Taylor, and R. W. Romani, "Cosmic Gravitational-Wave background: Limits from Millisecond Pulsar Timing," *Physical Review Letters*, vol. 65, no. 3, pp. 285–288, 1990.

[84] R. M. Shannon and J. M. Cordes, "Assessing the role of spin noise in the precision timing of millisecond pulsars," *The Astrophysical Journal*, vol. 725, pp. 1607–1619, 2010.

[85] Q. Gravity, "Pulsar timing and relativistic gravity," *Philosophical Transactions of the Royal Society of London. Series A: Physical and Engineering Sciences*, vol. 341, pp. 117–134, 1993.

[86] R. T. Edwards, G. B. Hobbs, and R. N. Manchester, "TEMPO2, a new pulsar timing package - II. The timing model and precision estimates," Tech. Rep. 4, 2006.

[87] G. B. Hobbs, R. T. Edwards, and R. N. Manchester, "TEMPO2, a new pulsar-timing package - I. An overview," *Monthly Notices of the Royal Astronomical Society*, vol. 369, pp. 655–672, 2006.

[88] A. G. Lyne, P. R. S, and F. Grahm Smith, "23 Years of Crab Pulsar Rotational History," *monthly Notices of the Royal Astronomical Society*, vol. 265, no. 4, pp. 1003–1012, 1993.

[89] X. P. Deng, W. Coles, G. Hobbs, M. J. Keith, R. N. Manchester, M. Shannon, and J. H. Zheng, "Optimal Interpolation and Prediction in Pulsar Timing," *Monthly Notices of the Royal Astronomical Society*, 2012.

[90] J. B. Thonas, "Reformulation of the relativistic conversion between coordinate time and atomic time," *The astronomical Journal*, vol. 80, no. 5, pp. 405–411, 1975.

[91] R. Blandford and S. A. Teukolskyi, "Arrival-Time Analysis for a Pulsar in a Binary System," *The Astrophysical Journal*, vol. 205, pp. 580–591, 1976.

[92] T. D. Moyer, "Transformation from Proper Time on Earth to Coordinate Time in Solar System Barycentric Space-Time Frame of Reference, Part 1," *Celestial Mechanics*, vol. 23, pp. 33–56, 1981.

[93] T. D. Moyer, "Transformation from Proper Time on Earth to Coordinate Time in Solar System Barycentric Space-Time Frame of Reference, Part 2," *Celestial Mechanics*, vol. 23, pp. 57–68, 1981.

[94] C. F. Martin, M. H. Torrence, and C. W. Misner, "Relativistic Effects on an Earth-Orbiting Satellite in the Barycenter Coordinate System," *Journal of Geophysical Research*, vol. 90, no. B11, pp. 9403–9410, 1985.

[95] R. W. Hellings, "Relativistic Effects in Astronomical Timing Measurements," *The Astronomical Journal*, vol. 91, no. 3, pp. 650–659, 1986.

[96] L. Fairhead and B. P., "An Analytical Formula for the Time transformation TB-TT," *Astronomy and Astrophysics*, vol. 229, pp. 240–247, 1990.

[97] T. Fukushima, "Time Ehpemeris," *Astronomy and Astrophysics*, vol. 294, pp. 895–906, 1995.

[98] D. R. Lorimer, "Binary and Millisecond Pulsars at the New Millennium An Introduction to Pulsar Astronomy," 2001.

[99] S. I. Sheikh, R. W. Hellings, and R. A. Matzner, "High-Order Pulsar Timing For Navigation," in *Institute of Navigation 63rd Annual Meeting*, 2007, pp. 432–443.

[100] Z. Huang, M. Li, and P. Shuai, "On time transfer in X-ray pulsar navigation," in *Science in China, Series E: Technological Sciences*, vol. 52, no. 5, 2009, pp. 1413–1419.

[101] G. W. Richter and R. A. Matzner, "Second-order contributions to relativistic time delay in the parametrized post-Newtonian formalism," *Physical Review D*, vol. 28, no. 12, pp. 3007–3012, 1983.

[102] I. Bar-David, "Communication under the Poisson Regime," *IEEE Transactions of Information Theory*, vol. 15, no. 1, 1969.

[103] G. Space, "Station Explorer for X-ray Timing and Navigation Technology (SEXTANT) Algorithm Description Document (ADD)," Tech. Rep., 2016.

[104] R. Pasupathy, "Generating Nonhomogeneous Poisson Processes," 2011. [Online]. Available: http://doi.wiley.com/10.1002/9780470400531.eorms0356

[105] P. Bratley, B. L. Fox, and L. E. Schrage, *A Guide to Simulation*. Springer, 1987.

[106] Y. Chen, "Thinning Algorithms for Simulating Point Processes," 2016. [Online]. Available: http://www.math.fsu.edu/ ychen/research/Thinning algorithm.pdf

[107] L. M. Winternitz, M. A. Hassouneh, J. W. Mitchell, J. E. Valdez, S. R. Price, S. R. Semper, W. H. Yu, P. S. Ray, K. S. Wood, Z. Arzoumanian, and K. C. Gendreau, "X-ray pulsar navigation algorithms and testbed for SEXTANT," in *IEEE Aerospace Conference Proceedings*, 2015.

[108] A. A. Emadzadeh, J. L. Speyer, and A. R. Golshan, "Asymptotically Efficient Estimation of Pulse Time Delay For X-ray Pulsar Based Relative Navigation," in *AIAA Guidance, Navigation, and Control Conference*. Chicago, Illinois: American Institute of Aeronautics and Astronautics, 2009.

[109] A. A. Emadzadeh, A. R. Golshan, and J. L. Speyer, "Consistent estimation of pulse delay for x-ray pulsar based relative navigation," in *Proceedings of the IEEE Conference on Decision and Control*. IEEE, 2009, pp. 1488–1493.

[110] O. C. De Jager, J. W. H. Swanepoel, and B. C. Raubenheimer, "A Powerful Test for Weak Periodic Signals with Unknown Light Curve Shape in Sparse Data," *Astronomy and Astrophysics*, p. 302, 1989.

[111] M. G. Bernhardt, T. Prinz, W. Becker, and U. Walter, "Timing X-ray Pulsars with Application to Spacecraft Navigation," in *High Time Resolution Astrophysics IV*, vol. 108, 2010.

[112] A. A. Emadzadeh and J. L. Speyer, "X-ray pulsar-based relative navigation using epoch folding," *IEEE Transactions on Aerospace and Electronic Systems*, vol. 47, no. 4, pp. 2317–2328, 2011.

[113] Y. Wang and W. Zhang, "Pulsar phase and doppler frequency estimation for XNAV using on-orbit epoch folding," *IEEE Transactions on Aerospace and Electronic Systems*, vol. 52, no. 5, pp. 2210–2219, 2016.

[114] S. L. Li, K. Liu, and L. L. Xiao, "Fleet algorithm for X-ray pulsar profile construction and TOA solution based on compressed sensing," *Optik*, vol. 125, no. 7, pp. 1875–1879, 2014. [Online]. Available: http://dx.doi.org/10.1016/j.ijleo.2013.10.032

[115] L. M. Winternitz, J. W. Mitchell, M. A. Hassouneh, J. E. Valdez, S. R. Price, S. R. Semper, W. H. Yu, P. S. Ray, K. S. Wood, Z. Arzoumanian, and K. C. Gendreau, "SEXTANT X-ray Pulsar Navigation demonstration: Flight system and test results," in *IEEE Aerospace Conference Proceedings*, 2016.

[116] L. W. Huang, B. Liang, and T. Zhang, "Pulse phase and doppler frequency estimation of X-ray pulsars under conditions of spacecraft and binary motion and its application in navigation," *Science China: Physics, Mechanics and Astronomy*, vol. 56, no. 4, pp. 848–858, 2013.

[117] W. C. Lindsey and C. M. Chie, "Survey of Digital Phase-Locked Loops," in *Proceedings of the IEEE Conference*, vol. 69, no. 4, 1981, pp. 410–431.

[118] S. A. Stephens and J. B. Thomas, "Controlled-Root Formulation for Digital Phase-Locked Loops," *IEEE Transactions on Aerospace and Electronic Systems*, vol. 31, no. 1, pp. 78–95, 1995.

[119] J. B. Thomas, "An Analysis of Digital phase-Locked Loops," *Response*, no. February, 1989.

[120] K. D. Anderson and D. Pines, "Methods of Pulse Phase Tracking for X-ray Pulsar Based Spacecraft Navigation using Low Flux Pulsars," in *SpaceOps Conference*, no. May, 2014. [Online]. Available: http://arc.aiaa.org/doi/abs/10.2514/6.2013-5202

[121] I. Sheikh, Suneel, P. S. Ray, K. Weiner, T. Wolff, Michael, and K. S. Wood, "Relative Navigation of Spacecraft Utilizing Bright , Aperiodic Celestial Sources," in *Institute of Navigation 63rd Annual Meeting*, 2007.

[122] S. I. Sheikh, D. J. Pines, P. S. Ray, K. S. Wood, M. N. Lovellette, and M. T. Wolff, "The Use of X-Ray Pulsars for Spacecraft Navigation," in *14th AAS/AIAA Space Flight Mechanics Conference*, 2004.

[123] P. H. Graven, J. T. Collins, S. I. Sheikh, and J. E. Hanson, "Spacecraft Navigation Usign X-Ray Pulsrs," in *7th International ESA Conference on Guidance, Navigation, & Control Systems*, 2008.

[124] X. P. Deng, G. Hobbs, X. P. You, M. T. Li, M. J. Keith, R. M. Shannon, W. Coles, R. N. Manchester, J. H. Zheng, X. Z. Yu, D. Gao, X. Wu, and D. Chen, "Interplanetary spacecraft navigation using pulsars," in *Advances in Space Research*, vol. 52, no. 9, 2013, pp. 1602–1621.

[125] L. Huang, P. SHUAI, B. LIANG, T. ZHANG, and C. ZHANG, "Synchronizing of Multiple Time-of-Arrivals for Pulsar-Based Navigation," *Transactions of the Japan Society for Aeronautical and Space Sciences*, vol. 57, no. 1, pp. 31–39, 2013.

[126] S. I. Sheikh, J. E. Hanson, J. Collins, and P. H. Graven, "Deep Space Navigation Augmentation Using Variable Celestial X-Ray Sources," in *Proceedings of the 2009 International Technical Meeting of The Institute of Navigation*, 2009, pp. 34 – 48.

[127] C. L. Thornton and J. S. Border, *Radiometric Tracking Techniques for Deep - Space Navigation*, 2000.

[128] Y. Wang, W. Zheng, X. An, S. Sun, and L. Li, "XNAV/CNS integrated navigation based on improved kinematic and static filter," *Journal of Navigation*, vol. 66, no. 6, pp. 899–918, 2013.

[129] X. Ning, M. Gui, J. Zhang, J. Fang, and G. Liu, "Impact of the Pulsar's Direction on CNS / XNAV Integrated Navigation," *IEEE Transactions on Aerospace and Electronic Systems*, vol. 53, no. 6, 2017.

[130] S. Sheikh and D. Pines, "Recursive Estimation of Spacecraft Position Using X-ray Pulsar Time of Arrival Measurements," in *ION 61st Annual Meeting*, 2005. [Online]. Available: http://www.asterlabs.com/publications/2005/Sheikh_et_al,_ION_61_AM_June_2005.pdf pp. 464–475.

[131] X. Ju, S. Jian, L. Hengnian, C. Lu, and L. Zhe, "Application of Multi-rate Sensor Data Fusion in the X-ray Pulsar Navigation," in *20th International Conference on Information Fusion*, 2017, pp. 1–6.

[132] P.-T. Chen, J. L. Speyer, D. S. Bayard, and W. A. Majid, "Autonomous Navigation Using X-Ray Pulsars and Multirate Processing," *Journal of Guidance, Control, and Dynamics*, vol. 40, no. 9, pp. 2237–2249, 2017. [Online]. Available: https://arc.aiaa.org/doi/10.2514/1.G002705

[133] J. Liu, J. Ma, J. Tian, Z. Kang, and P. White, "Pulsar navigation for interplanetary missions using CV model and ASUKF," *Aerospace Science and Technology*, vol. 22, no. 1, pp. 19–23, 2012. [Online]. Available: http://dx.doi.org/10.1016/j.ast.2011.04.010

[134] J. T. Runnels and D. Gebre-egziabher, "Six Degree of Freedom Navigation Using Astrophysical Signals of Oportunity," in *42nd AAS Guidance and Control Conference*, no. 73, 2019.

[135] N. Ashby and D. A. Howe, "Relativity and timing in X-ray pulsar navigation," in *Proceedings of the IEEE International Frequency Control Symposium and Exposition*, 2007, pp. 767–770.

[136] J. Hanson, S. Sheikh, P. Graven, and J. Collins, "Noise Analysis for X-ray Navigation Systems," in *IEE/ION Position, Location and Navigation Symposium*, 2008, pp. 704–713.

[137] J. W. Mitchell, M. Hassouneh, L. Winternitz, J. Valdez, S. Price, S. R. Semper, W. H. Yu, Z. Arzoumanian, P. Ray, K. S. Wood, R. J. Litchford, and K. C. Gendreau, "SEXTANT - Station Explorer for X-ray Timing and Navigation Technology," in *AIAA Guidance, Navigation, and Control Conference*, 2015. [Online]. Available: http://arc.aiaa.org/doi/10.2514/6.2015-0865

[138] H.-X. Wang and X.-J. Wu, "An Analysis of Average Pulsar Profiles and A Study of the rho-P relation of Pulsars," *Chinese Journal of Astronony and Astrophysics*, vol. 3, pp. 469–477, 2003. [Online]. Available: http://adsabs.harvard.edu/cgi-bin/nph-bib_query?bibcode=2003ChJAA...3..469W&db_key=AST&high=436c7b4a7a01561

[139] K. C. Gendreau, Z. Arzoumanian, P. W. Adkins, C. L. Albert, J. F. Anders, A. T. Aylward, C. L. Baker, E. R. Balsamo, W. A. Bamford, S. S. Benegalrao, D. L. Berry, S. Bhalwani, J. K. Black, C. Blaurock, G. M. Bronke, G. L. Brown, J. G. Budinoff, J. D. Cantwell, T. Cazeau, P. T. Chen, T. G. Clement, A. T. Colangelo, J. S. Coleman, J. D. Coopersmith, W. E. Dehaven, J. P. Doty, M. D. Egan, T. Enoto, T. W. Fan, D. M. Ferro, R. Foster, N. M. Galassi, L. D. Gallo, C. M. Green, D. Grosh, K. Q. Ha, M. A. Hasouneh, K. B. Heefner, P. Hestnes, L. J. Hoge, T. M. Jacobs, J. L. Jørgensen, M. A. Kaiser, J. W. Kellogg, S. J. Kenyon, R. G. Koenecke, R. P. Kozon, B. LaMarr, M. D. Lambertson, A. M. Larson, S. Lentine, J. H. Lewis, M. G. Lilly, K. A. Liu, A. Malonis, S. S. Manthripragada, C. B. Markwardt, B. D. Matonak, I. E. Mcginnis, R. L. Miller, A. L. Mitchell, J. W. Mitchell, J. S. Mohammed, C. A. Monroe, K. M. Montt de Garcia, P. D. Mulé, L. T. Nagao, S. N. Ngo, E. D. Norris, D. A. Norwood, J. Novotka, T. Okajima, L. G. Olsen, C. O. Onyeachu, H. Y. Orosco, J. R. Peterson, K. N. Pevear, K. K. Pham, S. E. Pollard, J. S. Pope, D. F. Powers, C. E. Powers, S. R. Price, G. Y. Prigozhin, J. B. Ramirez, W. J. Reid, R. A. Remillard, E. M. Rogstad, G. P. Rosecrans, J. N. Rowe, J. A. Sager, C. A. Sanders, B. Savadkin, M. R. Saylor, A. F. Schaeffer, N. S. Schweiss, S. R. Semper, P. J. Serlemitsos, L. V. Shackelford, Y. Soong, J. Struebel, M. L. Vezie, J. S. Villasenor, L. B. Winternitz, G. I. Wofford, M. R. Wright, M. Y. Yang, and W. H. Yu, "The Neutron star Interior Composition Explorer (NICER): design and development," in *Astronomical Telescopes and Instrumentation*, vol. 9905, 2016. [Online]. Available: http://proceedings.spiedigitallibrary.org/proceeding.aspx?doi=10.1117/12.2231304

[140] M. G. Revnivtsev, O. E. Gadzhily, A. A. Lutovinov, S. V. Molkov, V. A. Arefiev, M. N. Pavlinsky, and A. G. Tuchin, "On the possibility of improving the orbits of satellites based on observations of isolated X-ray pulsars," *Astronomy Letters*, vol. 41, no. 8, pp. 450–455, 2015. [Online]. Available: http://link.springer.com/10.1134/S106377371508006X

[141] M. G. Bernhardt, W. Becker, T. Prinz, F. M. Breithuth, and U. Walter, "Autonomous spacecraft navigation based on pulsar timing information," in *2nd International Conference on Space Technology, ICST 2011*, 2011, pp. 15–17.

[142] C. L. Hollenberg and J. A. Christian, "Initial Orbit Determination with Velocity Vectors and Angles," in *AAS/AIAA Astrodynamics Specialist Conference*, no. 18-410, 2018, pp. 1–8.

[143] V. Bowman and C.-A. Burdet, "On the General Solution to Systems of Mixed-Integer Linear Equations," *SIAM Journal on Applied Mathematics*, vol. 26, no. 1, pp. 120–125, 1974.

[144] M. F. Hurt and C. Waid, "A Generalized Inverse Which Gives all the Integral Solutions to a System of Linear Equations," *SIAM Journal on Applied Mathematics*, vol. 19, no. 3, pp. 547–550, 1970. [Online]. Available: http://epubs.siam.org/doi/abs/10.1137/0119053

[145] C. H. Acton, "Ancillary data services of NASA's navigation and Ancillary Information Facility," *Planetary and Space Science*, vol. 44, no. 1, pp. 65–70, 1996.

[146] C. Acton, N. Bachman, B. Semenov, and E. Wright, "A look towards the future in the handling of space science mission geometry," *Planetary and Space Science*, vol. 150, pp. 9–12, 2018. [Online]. Available: https://doi.org/10.1016/j.pss.2017.02.013